Equatorially trapped Rossby waves in the presence of meridionally sheared baroclinic flow in the Pacific Ocean

D.B. Chelton [a,*], M.G. Schlax [a], J.M. Lyman [a,1], G.C. Johnson [b]

[a] *College of Oceanic and Atmospheric Sciences, Oregon State University, 104 Oceanography Administration Building, Corvallis, OR 97331-5503, USA*
[b] *NOAA/Pacific Marine Environmental Laboratory, 7600 Sand Point Way N.E., Bldg. 3, Seattle, WA 98115-0070, USA*

Abstract

TOPEX/POSEIDON altimeter data are analyzed for the 8.5-year period November 1992 to May 2001 to investigate the sea surface height (SSH) and geostrophic velocity signatures of quasi-annual equatorially trapped Rossby waves in the Pacific. The latitudinal structures of SSH and both components of geostrophic velocity are found to be asymmetric about the equator across the entire Pacific with larger amplitude north of the equator. The westward phase speeds are estimated by several different methods to be in the range 0.5–0.6 m s^{-1}. These observed characteristics are inconsistent with the classical theory for first vertical, first meridional mode equatorially trapped Rossby waves, which predicts a phase speed of about 0.9 m s^{-1} with latitudinally symmetric structures of SSH and zonal velocity and antisymmetric structure of meridional velocity. The observations are even less consistent with the latitudinal structures of SSH and geostrophic velocity components for other modes of the classical theory.

The latitudinal asymmetries deduced here have also been consistently observed in past analyses of subsurface thermal data and altimeter data and have been variously attributed to sampling errors in the observational data, a superposition of multiple meridional Rossby wave modes, asymmetric forcing by the wind, and forcing by cross-equatorial southerly winds in the eastern Pacific. We propose a different mechanism to account for the observed asymmetric latitudinal structure of low-frequency equatorial Rossby waves. From the free-wave solutions of a simple 1.5-layer model, it is shown that meridional shears in the mean equatorial current system significantly alter the potential vorticity gradient in the central and eastern tropical Pacific. The observed asymmetric structures of sea surface height and geostrophic velocity components are found to be a natural consequence of the shear modification of the potential vorticity gradient. The mean currents also reduce the predicted westward phase speed of first meridional mode Rossby waves, improving consistency with the observations.
© 2003 Elsevier Science Ltd. All rights reserved.

Contents

---

* Corresponding author. Tel.: +1-541-737-4017; fax: +1-541-737-2064.
   E-mail address: chelton@coas.oregonstate.edu (D.B. Chelton).
  [1] Current affiliation: NOAA/Pacific Marine Environmental Laboratory, 7600 Sand Point Way N.E., Bldg. 3, Seattle, WA 98115-0070, USA

1. Introduction

It is well known that the latitudinal variation of the Coriolis parameter and its change in sign at the equator create a waveguide in the equatorial band between about 8° S and 8° N (Matsuno, 1966; Moore, 1968; Moore & Philander, 1977). The vertical modes of dynamical variability are determined from the stratification of the water column. The classical theory, in which the equations of motion for a given vertical mode are linearized about a state of rest on an equatorial β plane, yields an orthogonal basis set of free-wave eigensolutions. For each of these meridional modes, the latitudinal structures of the pressure and the two components of velocity can be expressed in terms of linear combinations of Hermite functions (Fig. 1). At low frequencies, the first vertical mode, first meridional mode that is often presumed to account for most of the variability propagates westward with a phase speed of ~0.9 m s^{-1}. The pressure perturbations associated with this mode are symmetric about the equator (solid line in the top panel of Fig. 1). In this study, the latitudinal structure and phase speed of quasi-annual westward propagating sea surface height (SSH) variability (which can be equated to the wave-induced pressure perturbations) and geostrophic velocity variability are determined from an analysis of TOPEX/POSEIDON altimeter data over the 8.5-year period November 1992 to May 2001. The observed characteristics are found to be inconsistent with the classical theory.

The discrepancies between the classical theory and the observed characteristics identified here from TOPEX/POSEIDON data have been reported previously from historical observations of subsurface thermal structure and altimeter data. Indeed, the latitudinal structures in Fig. 1 have never been observed in the ocean. As summarized in detail in Section 2, past studies have consistently found that the signatures of westward propagating thermocline variability (which can also be equated to the wave-induced pressure perturbations) and SSH variability are asymmetric with larger amplitudes on the north side of the equator. This observed asymmetry cannot be accounted for by any of the individual modes of the classical theory,

Meridional Modes 1 and 2
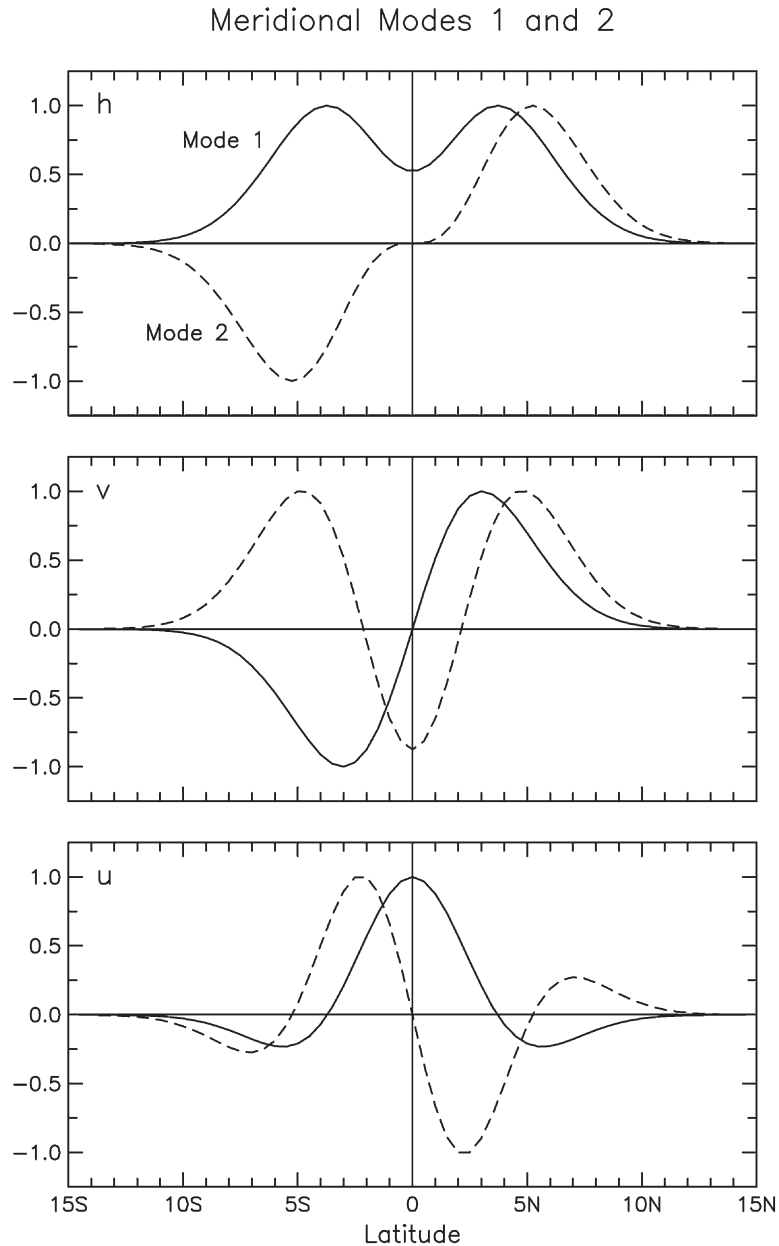
Fig. 1.   The latitudinal structures of sea surface height *h* (which can be equated with pressure), meridional velocity *v*, and zonal velocity *u* for the first (solid lines) and second (dashed lines) meridional modes of the classical theory that neglects the effects of background mean currents.

which are either symmetric (the odd modes) or antisymmetric (the even modes) in these variables. Most studies have also observed phase speeds that are 30–50% slower than predicted by the classical theory. It is widely presumed that the latitudinal asymmetry is attributable either to a superposition of multiple meridional modes or to the asymmetry of the wind forcing, which is much stronger north of the equator.

Based on a simple model, we propose that the latitudinal asymmetry and slow phase speeds of observed equatorially trapped Rossby waves can be mostly attributed to the effects of meridional shears in the background mean currents that are neglected in the classical theory.

The paper is organized as follows. A review of past observational studies of equatorially trapped waves is given in Section 2. The processing applied to the TOPEX/POSEIDON data in order to isolate the SSH signatures of quasi-annual equatorially trapped Rossby waves is summarized in Section 3.1. The Acoustic Doppler Current Profiler measurements of upper-ocean velocity that later form the basis for a theoretical calculation of equatorially trapped Rossby wave eigenfunctions in the presence of meridionally sheared background currents are summarized in Section 3.2. Observational determination of the latitudinal structure of quasi-annual variability within the equatorial waveguide from TOPEX/POSEIDON data is presented in Section 4 and phase speed estimates are obtained in Section 5. Both the observed latitudinal asymmetry (larger north of the equator) and the slow observed westward phase speeds are inconsistent with the classical theory for equatorial Rossby waves.

While the effects of equatorial currents on the dispersion relations for equatorially trapped Rossby waves have previously been considered (Philander, 1979; Chang & Philander, 1989; Zheng, Yan, Ho & Tai, 1994), the effects of equatorially asymmetric currents on the latitudinal structures of the waves have not. In Section 6, we use the simple 1.5-layer model of the baroclinic structure of the equatorial Pacific previously considered in an idealized setting by Philander (1979) to determine the eigenfunctions of the β-plane equations linearized about observed meridional profiles of background mean zonal velocity in the upper ocean. It is shown that the strong meridional shears in the equatorial current system that are neglected in the classical theory produce latitudinally asymmetric equatorially trapped Rossby waves with reduced phase speeds.

2. Observational background

Unambiguous observational verification of the existence of equatorially trapped Rossby waves is difficult, because of stringent sampling requirements. Determination of the detailed meridional structure of the waves necessitates fine-scale sampling across the full latitudinal extent of the equatorial waveguide between about 8° N and 8° S. By the late 1970s, a sufficient database of mechanical bathythermograph (MBT) and expendable bathythermograph (XBT) data had accumulated to allow investigations across the northern half of the equatorial waveguide in the Pacific; subsurface thermal variability remains undersampled south of the equator even today. The data have nonetheless provided useful information about the cross-equatorial structure of equatorially trapped Rossby waves.

Equatorial asymmetry of the amplitude of annual variations of the thermocline depth was first documented by Meyers (1979). Thermocline variability was characterized by depth variations of the 14 °C isotherm estimated from historical MBT and XBT observations between 30° S and 30° N across the full width of the Pacific. Within a well-defined band of energetic variability centered near 6° N, the observed annual thermocline variations propagated westward with an estimated phase speed of 0.58 m s^{-1}. This phase speed is 35% slower than the approximate 0.9 m s^{-1} phase speed predicted by the classical theory for first vertical mode, first meridional mode annual Rossby waves. The MBT and XBT data were too sparse to detect westward propagation south of the equator. The data were, however, sufficient to show that thermocline variability was about a factor of two smaller in amplitude across the southern half of the equatorial waveguide, although Meyers (1979) expressed concern that the estimates of southern hemisphere variability may have been biased by sampling errors.

From historical ship-based observations of the wind stress compiled by Wyrtki and Meyers (1976), the possibility that the observed westward propagating signals might be generated by the wind stress curl was investigated by Meyers (1979). He noted that the energetic annual westward propagating thermocline depth

variability along 6° N was coincident with the band of maximum annual variability of the wind stress curl in association with seasonal meridional migrations of the Intertropical Convergence Zone (ITCZ). Except in the far western Pacific, there was remarkably little wind stress curl variability south of the equator within the tropical band. This strong equatorial asymmetry of the wind stress curl field has been confirmed by numerous subsequent studies based both on more complete observational datasets and on the analyzed wind fields from operational weather forecast models (e.g., McPhaden, Busalacchi & Picaut, 1988; Kessler, 1990; Kessler & McCreary, 1993; Rienecker, Atlas, Schubert & Willett, 1996; Wang, Wu & Lukas, 2000; see also Figs 6 and 7 below).

The band of westward propagating thermocline variations along 6° N is within the equatorial waveguide near the expected latitude of the maximum amplitude of first meridional mode equatorial Rossby waves (Fig. 1). Though the variability at this latitude should be governed by equatorial wave dynamics, Meyers (1979) investigated the linear, 1-dimensional forced wave equation from midlatitude Rossby wave theory and argued that the thermocline variability along 6° N could be interpreted as a forced wave response to the intense annual variation of the wind stress curl in the eastern tropical Pacific. Regardless of the quantitative applicability of this model at 6° N, Meyers (1979) found from consideration of only the local time-dependent response that the observed thermocline variability could not be explained as purely local Ekman pumping by the wind stress curl.

Lukas and Firing (1985) analyzed the densely sampled XBT dataset from the Hawaii-to-Tahiti Shuttle Experiment (Wyrtki et al., 1981) along 150° W, 153° W and 158° W. This appears to be the first study in which the annual variability within this latitude range was interpreted in the context of equatorial wave theory. Because of the restricted longitudinal span of the three XBT lines, it was not possible to estimate the phase speed of the observed thermocline variability. However, the data clearly showed that isotherm displacements within the thermocline were largest near 4° N, with at least a factor of two smaller variability south of the equator. They suggested that the asymmetry of the thermocline variations was to be expected in view of the strong asymmetry in the wind forcing noted earlier by Meyers (1979). They further speculated that the larger amplitude variability north of the equator was induced by cross-equatorial southerly winds in the eastern Pacific and the change of sign of the Coriolis parameter at the equator. The dynamics of this hypothesized wind generation are unclear.

The annual westward propagation identified by Meyers (1979) in subsurface thermal data was also detected by Mitchum and Lukas (1990) in sea level measurements at seven island tide gauges between 5 and 10° N across the western tropical Pacific. From the zonal phase variation of the annual harmonic, they estimated a westward phase speed of 0.50 ± 0.10 m s^{-1} with an amplitude of about 0.05 m. To investigate the generation mechanism for this observed sea level variability, they looked closely at 1 year of high-quality wind measurements extending from December 1979 to November 1980 during the First GARP (Global Atmospheric Research Program) Global Experiment. Noting the existence of annual westward propagating zonal wind stress variations along the equator with a phase speed about the same as that of the annual sea level and thermocline depth variations near the higher latitude of 7.5° N, they hypothesized that the westward propagating oceanic variability was resonantly forced by the wind. However, westward propagation was not readily apparent in the winds between 5 and 10° N (the latitude band of the observed westward propagating sea level variations); the phase of annual variations of the zonal wind stress in this latitude band was nearly uniform across most of the Pacific (see also Fig. 7 below).

In an effort to isolate a component of the annual zonal wind stress variability along 7.5° N that propagated westward at the observed 0.5 m s^{-1} phase speed of the sea level variations, Mitchum and Lukas (1990) band-pass filtered the annual zonal wind stress to extract the variability in the wavenumber band that corresponds to this phase speed. While the annual variability within this wavenumber band was found to be energetic across the Indian Ocean and in the far western Pacific, its amplitude across most of the Pacific was only a fraction of a meter per second (see Fig. 10 of Mitchum & Lukas, 1990). It thus seems highly unlikely that resonant forcing by the weak annual variability of westward propagating zonal winds in this

wavenumber band could account for the observed large-amplitude westward propagating sea level variations.

Annual variability of the thermocline across the full width of the tropical Pacific was re-examined by Kessler (1990) from a more comprehensive and quality-controlled MBT and XBT dataset than was available for the earlier study by Meyers (1979). Within the equatorial waveguide, the largest annual variations of the depth of the 20° C isotherm were in a zonal band near 5° N extending from 110–170° W. Thermocline variations along 6° N propagated westward with an estimated phase speed of 0.58 m s^{-1} identical to the estimate obtained by Meyers (1979). As in the earlier analysis, Kessler (1990) showed that the amplitudes of thermocline depth variations were much smaller in the southern half of the equatorial waveguide.

From an analysis of the Florida State University pseudo-stress wind fields, Kessler (1990) confirmed the remarkable covariability of the annual wind field along 5° N across the full width of the Pacific. Using the same linear, 1-dimensional forced wave equation from midlatitude Rossby wave theory that had previously been considered by Meyers (1979), Kessler (1990) concluded that the observed thermocline variability was comprised of westward propagating free waves generated by the wind stress curl in the eastern tropical Pacific. From consideration of only the local time-dependent response, Kessler (1990) confirmed that the local Ekman pumping response to wind stress curl forcing was negligible along this latitude.

The nature of deep isotherm displacements to depths of 3000 m was investigated by Kessler and McCreary (1993) from historical observations of deep hydrographic profiles between 10° S and 10° N across the full width of the Pacific. They attempted to rationalize the observed latitudinal structure in terms of equatorial wave theory. Consistent with the structure of pressure perturbations associated with first meridional mode equatorially trapped Rossby waves (solid line in the top panel of Fig. 1), there were well-defined maxima in the isotherm displacements near 5° N and 5° S with a local minimum at the equator. However, as in previous studies of isotherm depth variations in the upper 1000 m from MBTs and XBTs, they found larger annual variability of the isotherm displacements along 5° N than along 5° S. Although they expressed concern about the sparse sampling of hydrographic profiles in the central Pacific, Kessler and McCreary (1993) concluded that sampling errors were not likely to provide a complete explanation for the asymmetry of the observed isotherm displacements.

In search of a mechanism for the observed asymmetric structure, Kessler and McCreary (1993) analyzed the output of a linear, continuously stratified model forced by a realistic, equatorially asymmetric annual cycle of the wind stress field. The particular model that they considered requires separability of the vertical and horizontal mean structures, and is therefore restricted to zero background mean flow with a horizontally uniform background mean density field. The free meridional modes of this model are thus the Hermite solutions of the classical theory. Isotherm displacements in this wind-forced model exhibited the symmetric structure expected from the classical theory for first meridional mode Rossby waves. Forcing with a realistically asymmetric annual wind stress field generated symmetric equatorial Rossby waves. Likewise, neither the cross-equatorial southerly winds suggested by Lukas and Firing (1985), nor resonant forcing by the zonal wind stress suggested by Mitchum and Lukas (1990), were able to generate latitudinally asymmetric westward propagating thermocline variability.

A significant limitation of the linear model used in the Kessler and McCreary (1993) analysis is that it is not able to assess the importance of the asymmetric mean density and zonal current structures in the eastern tropical Pacific. The authors noted in particular the potential importance of the northern branch of the South Equatorial Current that extends a few degrees north of the equator. It will be shown in Section 6 that this feature of the background mean zonal velocity field indeed modifies the free modes of the system in such a manner that the first meridional mode equatorial Rossby waves have an asymmetric latitudinal structure very similar to the observations.

On the basis of the Kessler and McCreary (1993) modeling results, it appears that asymmetric wind forcing in the absence of an asymmetric background mean flow cannot generate asymmetric equatorial Rossby waves. Asymmetric Rossby waves are, however, generated in more sophisticated models that allow

realistic asymmetric background mean currents. For example, sea level variability within the equatorial waveguide in the linear, four-vertical mode shallow-water model considered by McPhaden et al. (1988) was about a factor of two larger north of the equator when the model was forced by winds derived from ship observations and cloud motion vectors. Likewise, westward propagation of thermocline variability centered near 5° N and 5° S with about a factor of two larger amplitude in the north is clearly evident in the National Centers for Environmental Prediction (NCEP) Ocean Data Assimilation model output analyzed by Wang et al. (2000). They suggested that the thermocline variations in the eastern Pacific are larger north of the equator because of local Ekman pumping by the equatorially asymmetric wind stress curl. It is noteworthy that the westward propagating thermocline variability in the NCEP model retained its asymmetric latitudinal structure across the central and western Pacific, where Wang et al. (2000) concluded that the prominent westward propagation consists of free equatorial Rossby waves forced remotely in the eastern Pacific. This suggests that the free modes of the system are equatorially asymmetric, in contradiction to the symmetric or antisymmetric structures expected from the classical theory. While equatorial Rossby waves are undoubtedly generated by the winds, we suggest in Section 7 that the asymmetry of the wind forcing plays only an indirect role in the generation of asymmetric equatorial Rossby waves through the establishment of a mean equatorial current system with asymmetric meridional shears that modify the latitudinal structure of the free waves.

The completion of the Tropical Atmosphere-Ocean (TAO) buoy array of thermistor chains (McPhaden et al., 1998) has eliminated temporal sampling errors in subsurface thermal data as a limitation in the investigation of the symmetry of long equatorially trapped Rossby waves. The coarse longitudinal spacing of about 15° between TAO moorings is not a major concern for the 10 000 km and longer wavelengths of quasi-annual Rossby waves. While the meridional structure of the waves cannot be resolved by the coarse latitude spacing of the moorings (which are located at the equator and at latitudes of 2, 5 and 8° in both hemispheres), the moorings along 5° N and 5° S are located near the latitudes of maximum thermocline variability associated with the first meridional mode equatorial Rossby wave. These waves should therefore be easily detectable in the TAO data.

Yu and McPhaden (1999) analyzed the data from all of the TAO moorings that were in operation for five or more years during the period 1988–1996. They found clear westward propagation of annual variations of the 20 °C isotherm depth and the surface dynamic height along both 5° N and 5° S across the entire Pacific with phase speeds consistent with the approximate 0.9 m s^{-1} phase speed of first vertical mode, first meridional mode equatorial Rossby waves in the classical theory. While the phase speeds estimated from the TAO data are faster than the 0.5–0.7 m s^{-1} phase speeds estimated as previously summarized from subsurface thermal data and tide gauge data, Yu and McPhaden (1999) report large uncertainties of 0.3–0.7 m s^{-1}. The TAO estimates may therefore be consistent with the slower phase speeds reported by other investigators, but the discrepancy merits further investigation that is beyond the scope of this study.

As in all previous analyses of subsurface thermal data from MBTs, XBTs and hydrographic profiles, Yu and McPhaden (1999) observed about a factor of two asymmetry in the amplitudes of the variations of both isotherm depth and dynamic height along 5°N and 5°S. Following the suggestions of previous investigators, they speculated that this asymmetric structure is attributable to stronger wind stress curl north of the equator (Meyers, 1979; Kessler, 1990), to forcing by cross-equatorial southerly winds in the eastern tropical Pacific (Lukas & Firing, 1985), or to resonant forcing by westward propagating annual variations of the zonal wind stress (Mitchum & Lukas, 1990). As discussed above, the model considered by Kessler and McCreary (1993), when forced by realistic winds, suggests that none of these features in the wind field can account for the observed asymmetry of equatorial trapped Rossby waves without the existence of an asymmetric background mean equatorial current system.

Beginning with Geosat in 1986, the advent of satellite altimetry (Fu & Cazenave, 2001) has provided an observational dataset in which sampling errors can be discounted as an explanation for the apparent latitudinal asymmetry of equatorially trapped Rossby waves. In the first analysis of altimeter data for this

purpose, Delcroix, Picaut and Eldin (1991) were able to identify clear westward propagation across the tropical Pacific from the first 13 months of Geosat altimeter data. The observed SSH variability consisted of maxima centered near 4° N and 4° S with a local minimum on the equator. For the short 6-month period April–October 1987, they estimated a westward phase speed of 1.0 ± 0.3 m s^{-1} between 125° W and 165° E, which is consistent with the classical theory. Because of the large uncertainty owing to the short 6-month data record, this phase speed estimate is also consistent with the slower 0.5–0.7 m s^{-1} reported by other investigators.

Delcroix et al. (1991) concluded that the observed SSH variability could be interpreted as the latitudinally symmetric first meridional mode of the classical theory. Careful scrutiny of their Fig. 9, however, reveals a distinct asymmetry with larger amplitude north of the equator along six of the nine longitudes that they considered between 110° W and 165° E. This asymmetry is also apparent across the eastern and central Pacific in the time-longitude plots of 17 months of Geosat SSH data along 4° N and 4° S in Fig. 2 of Fu, Vazquez and Perigaud (1991).

To investigate further the interpretation of the observed westward propagating signals in the Geosat data as equatorially trapped Rossby waves, Delcroix et al. (1991) computed zonal geostrophic velocity anomalies from the SSH fields. Although they concluded that the observed latitudinal structure of zonal geostrophic velocity was consistent with the equatorially symmetric structure in the classical theory (solid line in the bottom panel of Fig. 1), a distinct asymmetry with a central maximum at 2° N is evident in their Fig. 12. This off-equatorial maximum was flanked by secondary extrema with opposite signs. While this is qualitatively consistent with the classical theory, the negative extremum at 6° N was more than a factor of two larger in amplitude than the negative extremum at 7° S.

In a follow-up analysis of Geosat data for the extended 3-year time period from November 1986 to September 1989, Delcroix, Boulanger, Masia and Menkes (1994) investigated equatorial wave dynamics in the tropical Pacific during the 1986–1987 El Niño and the ensuing 1988–1989 La Niña. The latitudinal structure of equatorial waves was difficult to determine from SSH because of the dominance of the El Niño and La Niña signals. The structure was somewhat clearer in the zonal geostrophic current anomalies computed from the Geosat data. The maximum of the zonal velocity was centered 1–2° north of the equator across most of the Pacific.

The asymmetries observed by Delcroix et al. (1991, 1994) in both SSH and zonal velocity, and the northward displacement of the central maximum of the zonal velocity, are inconsistent with the classical theory for equatorially trapped Rossby waves. It is shown in Section 6 that these are the salient features of the eigenfunctions for equatorially trapped Rossby waves in the presence of the background mean equatorial currents in the Pacific.

The contributions of equatorial Kelvin and Rossby waves to the ocean adjustment from the 1986–1987 El Niño to the 1988–1989 La Niña were investigated by Delcroix et al. (1994) by projecting the Geosat estimates of zonal current anomalies onto the Kelvin wave mode and the first three meridional Rossby wave modes of the classical theory. About 70% of the variance was accounted for by just the Kelvin and first meridional mode Rossby wave. The projection method was extended to include additional higher-order Rossby wave modes and applied to the first 14 months of TOPEX/POSEIDON data by Boulanger and Menkes (1995) to investigate equatorial wave dynamics during the 1992–1993 El Niño. This approach has subsequently been applied to longer records of TOPEX/POSEIDON data by Boulanger and Fu (1996), Boulanger and Menkes (1999) and Delcroix, Dewitte, DuPenhoat, Masia and Picaut (2000). Use of the projection method side steps the issue of latitudinal asymmetries of the westward propagating signals by effectively assuming that any asymmetries are a result of a superposition of multiple meridional modes of equatorially trapped Rossby waves.

To date, the only attempt that we are aware of to determine explicitly the latitudinal structure of SSH variations within the equatorial band from TOPEX/POSEIDON data is the complex empirical orthogonal function analysis of the first 32 months of data presented by Susanto, Zheng and Yan (1998). It is difficult

to interpret their estimates of the meridional structure in the western half of the tropical Pacific in the context of equatorial wave dynamics, most likely because the equatorially trapped Rossby wave signals of interest are contaminated by other processes affecting SSH (see the discussion in Section 3.1 below). Across the eastern half of the tropical Pacific, however, westward propagating SSH variability was unambiguously asymmetric with larger amplitude north of the equator. Susanto et al. (1998) speculated that the observed asymmetric latitudinal structure might be a result of either asymmetric wind forcing or the effects of background mean currents, but they did not rigorously investigate either of these hypotheses. Rather, they interpreted the asymmetric structure as indicative of a superposition of multiple equatorially trapped Rossby wave modes. They estimated westward phase speeds of 0.6 m s^{-1} and 0.4 m s^{-1} along latitudes of 5° N and 7° S, respectively, consistent with the earlier estimates from subsurface thermal data and tide gauge data.

It is shown from the analysis of TOPEX/POSEIDON data in Section 4 that quasi-annual SSH variability retains a remarkably constant asymmetric latitudinal structure over a zonal distance of more than 8000 km. It seems unlikely that mode superposition can account for the observed asymmetry of equatorially trapped Rossby waves over this longitudinal range. The westward phase speed of the meridional mode m equatorially trapped Rossby wave in the classical theory is proportional to $(2m + 1)^{-1}$. Thus, for example, the phase speed of meridional mode 2 is 40% slower than the phase speed of meridional mode 1. While a local superposition of meridional modes 1 and 2 could conspire to produce the observed asymmetry at any particular longitude, this structure could not be maintained as the meridional modes 1 and 2 of the classical theory propagated 8000 km westward across the basin, because of the disparate phase speeds of the two modes.

The inadequacy of mode superposition as an explanation for the observed latitudinal asymmetry of westward propagating SSH and thermocline variability seems to be borne out in the results of the projection method presented by Boulanger and Menkes (1995), see their Table 1. They estimated the phase speeds of the equatorial Kelvin wave and the first three meridional Rossby wave modes obtained by projection of SSH onto the free modes of the classical theory. While the theoretical phase speed of meridional mode 2 is 40% slower than that of meridional mode 1, their estimated phase speed was actually 10% faster for meridional mode 2 (though with large uncertainty). The SSH signatures of meridional modes 1 and 2 in their analysis thus essentially propagated synchronously westward across the Pacific. This phase locking raises questions about whether the asymmetric latitudinal structure in SSH is really a superposition of two dynamical modes or is simply a mathematical artifact of local orthogonal decomposition of the latitudinal structure of SSH. We argue in Section 6 that the first meridional mode of an equatorial ocean with the observed meridionally sheared mean zonal currents is a more efficient and dynamically consistent description of the observed asymmetric latitudinal structure. This could explain the close match in phase speeds obtained by Boulanger and Menkes (1995) for their superposed Hermite solutions for meridional modes 1 and 2; the sum of these two orthogonal modes, with the same westward phase speed as determined empirically by Boulanger and Menkes (1995), can describe the single dynamical Rossby wave mode of the meridionally sheared equatorial current system.

In summary, every observational study that has critically examined the latitudinal structure of quasi-annual variability in the equatorial waveguide has found latitudinal asymmetry with larger amplitude north of the equator. This asymmetry has been attributed to a variety of different effects, including sampling errors in the data, a superposition of multiple meridional modes, equatorially asymmetric forcing by the wind stress curl, resonant forcing by the zonal wind stress, and forcing by cross-equatorial southerly winds in the eastern tropical Pacific. As summarized in this section, we believe that none of these mechanisms satisfactorily explains the latitudinal asymmetry that has consistently been observed in thermocline, SSH and zonal current variability. Furthermore, most of the observational studies have found westward phase speeds significantly slower than predicted by the classical theory. No explanation has been offered in these past observational studies for the mismatch between the observed and predicted phase speeds (see, however,

the review of theoretical studies of long Rossby waves in Section 6.1). The classical theory appears to be an incomplete description of equatorially trapped Rossby waves.

3. Data processing

3.1. Sea surface height

The first 8.5 years of TOPEX/POSEIDON altimeter observations of SSH (November 1992 to May 2001) are analysed in Sections 4 and 5 to determine the latitudinal structure and phase speed of westward propagating quasi-annual SSH variability. Standard corrections were applied to the raw altimeter data (Chelton, Ries, Haines & Fu, 2001). The 4-cm accuracy of individual SSH measurements can be improved to the sub-centimeter level by appropriate spatial and temporal smoothing of the data with concomitant loss of resolution (Greenslade, Chelton & Schlax, 1997; Chelton & Schlax, 2003). The details of the processing applied to the TOPEX/POSEIDON data to isolate the quasi-annual westward propagating SSH variability that is of interest in this study are summarized here.

The challenge is to isolate the signatures of quasi-annual equatorially trapped Rossby waves from other contributions to SSH variability. These other processes include the very energetic monthly variability associated with tropical instability waves (Chelton, Schlax, Lyman & Szoeke, 2003), equatorial Kelvin waves (see Section 2.3 of Picaut & Busalacchi, 2001), interannual variability associated with the major El Niño event that occurred in 1997–1998 (Delcroix et al., 2000) and steric effects, the most energetic of which are associated with the annual heating and cooling cycle (Stammer, 1997; Chambers, Tapley & Stewart, 1997). These unwanted contributions to SSH variability were attenuated through the following three-step filtering procedure.

The TOPEX/POSEIDON data were initially smoothed onto a 1° of longitude by 1° of latitude by 10-day grid by applying a three-dimensional quadratic loess smoother (Cleveland & Devlin, 1988; Schlax & Chelton, 1992; see also the appendix of Greenslade et al., 1997) with half spans of 15° in longitude, 2° in latitude and 150 days. The filter transfer function for the quadratic loess smoother has nominal half-power wavenumber and frequency filter cutoffs equal to the reciprocals of the half spans. The half spans chosen here thus correspond to filter cutoffs analogous to those of $7.5° \times 1° \times 75$-day block averages, though with smaller filter side lobes than in the filter transfer function for block averages. These particular spatial smoothing parameters that retain high meridional resolution at the expense of zonal resolution were chosen mindful of the dynamics of quasi-annual equatorial Rossby waves. The temporal filter cutoff of 150 days was chosen to eliminate the variability associated with tropical instability waves centered near 5° N in the eastern and central Pacific. Tropical instability waves consist primarily of monthly variability but the time scales extend to periodicities of about 100 days during some years (Chelton et al., 2003). The 150-day low-pass filtering also attenuates equatorial Kelvin waves, which are confined to within a few degrees of the equator and propagate eastward across the full width of the Pacific in less than 100 days.

The $15° \times 2° \times 150$-day filtered SSH variability is most energetic between 5° S and 5° N across the entire eastern half of the Pacific and at latitudes higher than 5° N in the far western tropical Pacific (top panel of Fig. 2). Much of this variability is associated with the 1997–1998 El Niño and some is likely associated with annual steric heating and cooling. There is also energetic variability along 10° N in the eastern Pacific. This is a region of strong annual forcing by the wind stress curl in association with the ITCZ and with the Papagayo wind jet that extends 1000 km or more to the west of the gap through the Central American mountains that is formed by the Nicaraguan Lake District (Chelton, Freilich & Esbensen, 2000).

The unwanted contributions to SSH variability from large-scale steric heating and cooling, the shorter-wavelength variability associated with the Papagayo wind jet and midlatitude Rossby waves outside of the
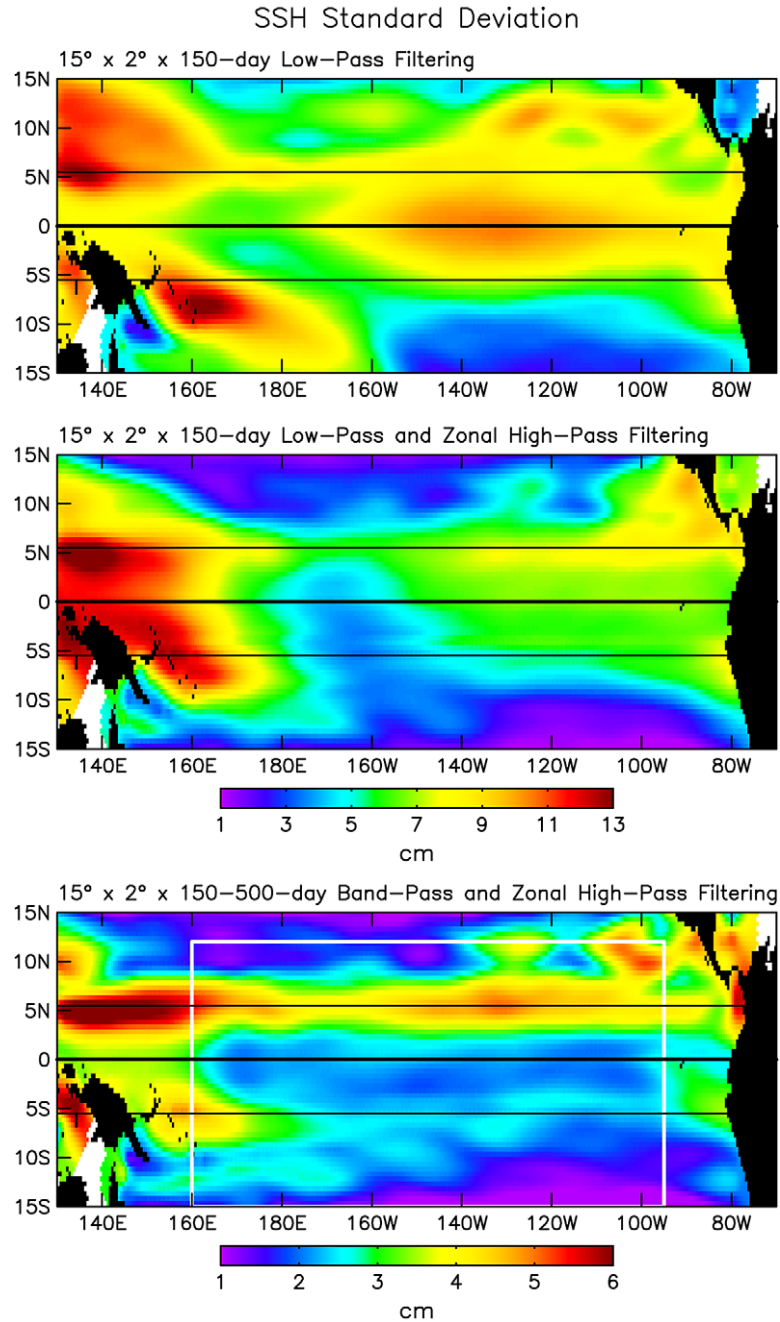
Fig. 2. Geographical variation of the standard deviation of SSH after each of the three levels of filtering indicated at the tops of the panels (see text for details). Note the different color scale for the bottom panel. The white box in the bottom panel delineates the region in which equatorially trapped Rossby waves are investigated in Sections 4 and 5.

equatorial waveguide, and residual equatorial Kelvin wave signals were attenuated by applying a one-dimensional loess smoother with a latitudinally varying zonal half span and subtracting the resulting spatially low-pass filtered SSH from the $15° \times 2° \times 150$-day filtered SSH. The half span was selected to achieve a zonal wavelength half-power filter cutoff λ_c that decreased cosinusoidally from 30 000 km at the equator to 6000 km at the maximum latitude of $15°$ considered in this study, i.e.,

$$\lambda_c(\text{km}) = 3 \times 10^4 \cos\left(\frac{2\pi\theta}{\theta_o}\right)$$

where θ is latitude and $\theta_0 = 30\pi/\cos^{-1}(0.2)$

The zonal high-pass filtering successfully attenuates the variability outside of the equatorial waveguide (middle panel of Fig. 2). Inside of the waveguide, the filtering reduces, but does not entirely eliminate the variability with large zonal scale associated with processes unrelated to the quasi-annual equatorially trapped Rossby waves of interest here. In particular, there is still large-amplitude variability in the western equatorial region and, to a somewhat lesser extent, in the eastern equatorial region. (The small increase in variability in the far western equatorial Pacific is an 'edge effect' that results from a combination of filter imperfection and the large-amplitude variability in the western equatorial Pacific.)

The nature of the zonally high-pass filtered SSH variability in the western and eastern tropical Pacific becomes apparent from the time-longitude plots of the filtered SSH along $5.5°$ N and $5.5°$ S shown in Fig. 3 (see the two thin horizontal lines in the standard deviation maps in Fig. 2). Comparing the $15° \times 2° \times 150$-day smoothed SSH from the first filtering step (left panels) with the results after applying the zonal high-pass filtering (middle panels) shows that the latter reduces the zonally coherent variability that is especially apparent during periods of positive SSH.

Westward propagation of SSH is most easily identified in the left and middle panels of Fig. 3 from the negative SSH features. This variability has larger amplitude and is better defined along $5.5°$ N than along $5.5°$ S. However, these westward propagating signals that are the focus of this study were somewhat obscured by the large-scale SSH variability that began with the onset of El Niño in mid-1997 and continued with the persistent La Niña conditions that developed after 1998.

While especially pronounced in the eastern and western regions, the effects of the El Niño-Southern Oscillation (ENSO) phenomenon are present throughout the tropical Pacific. The ENSO effects in the central tropical Pacific, for example, are evident in the time series of $15° \times 2° \times 150$-day smoothed and zonally high-pass filtered SSH variability at $5.5°$ N, $140°$ W and $5.5°$ S, $140°$ W (middle two panels of Fig. 4). There is a very well-defined seasonal cycle at both of these locations, although it does not consist of a simple annual harmonic. Relatively short-lived minima occur for about 3 months centered around April of each year and more persistent maxima occur for about 6 months from approximately July to January of each year. The seasonal cycle thus consists of a superposition of both annual and semiannual variability. This seasonal cycle is almost identical to that of temperature variations at a depth of 450 m deduced from XBT data near this longitude (Lukas et al., 1984).

The annual variability of SSH at $5.5°$ N, $140°$ W is related to the known seasonal variability of the equatorial current system (e.g., Reverdin, Frankignoul, Kestenare & McPhaden, 1994; Johnson, Sloyan & Kessler, 2002). The latitude of $5.5°$ N is near the ridge in dynamic height that separates the westward flow of the northern branch of the South Equatorial Current from the eastward flow of the North Equatorial Countercurrent. The April minimum of SSH along this ridge and the associated minimum meridional gradients of SSH on the flanks of the ridge thus coincide with the timing of the minimum transports of these opposing currents near $140°$ W.

The exceptionally strong 1997–1998 El Niño signal (top panel of Fig. 4) is associated with a dramatic alteration of the normal seasonal cycle, especially at $5.5°$ S. The 1997–1998 El Niño also disrupted the normal seasonal evolution of the wind stress curl field in this region (bottom panel of Fig. 4), clearly indicative of the coupled nature of atmospheric and oceanic conditions during this El Niño. After the
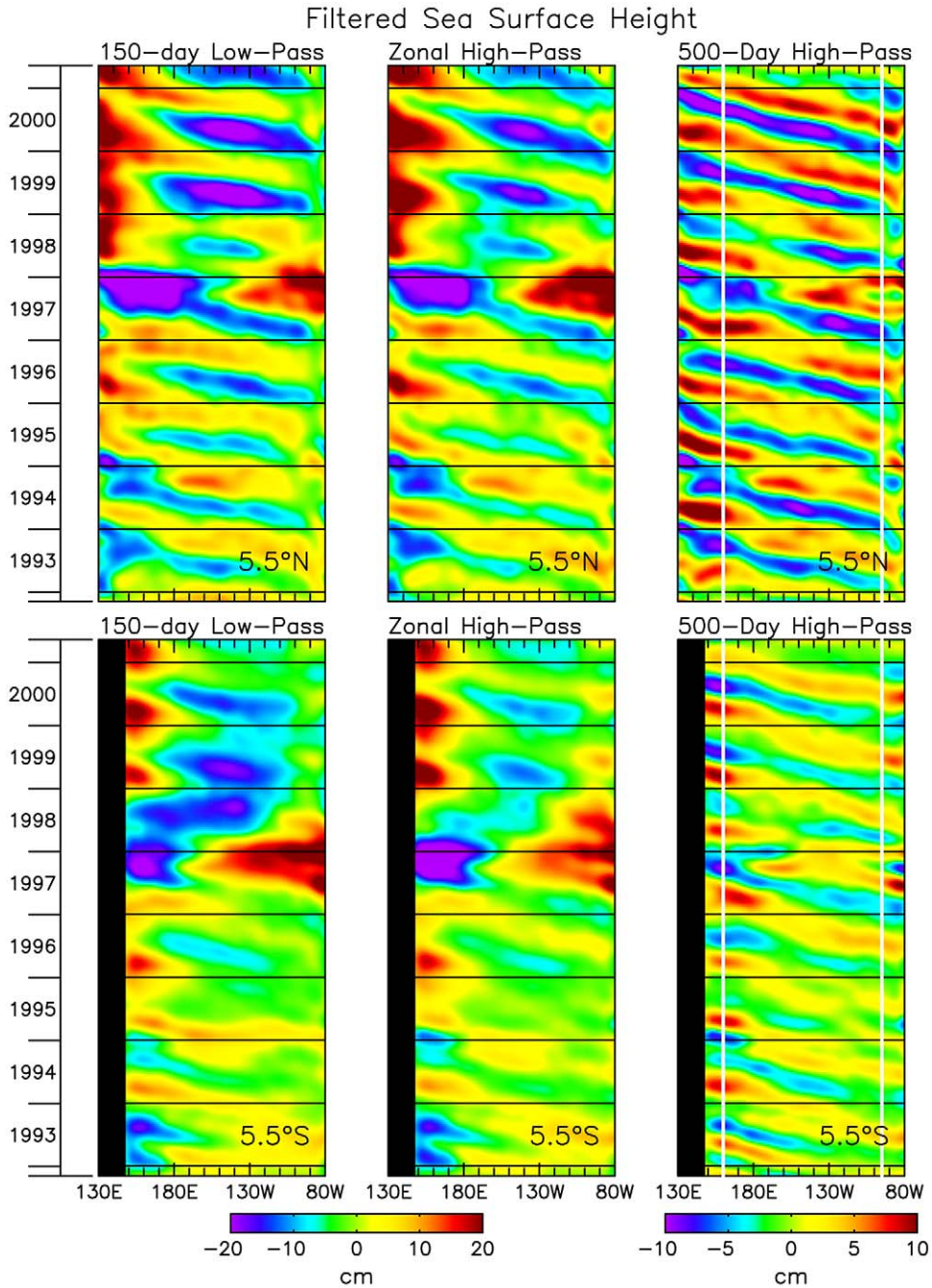
Fig. 3. Time-longitude plots of SSH along 5.5° N (upper panels) and 5.5° S (lower panels). The 15° × 2° × 150 - day smoothed SSH obtained after the first level of filtering is shown in the left panels. The results obtained after additionally applying the latitudinally varying zonal high-pass filter described in the text are shown in the middle panels. The final results after also high-pass filtering the time series at each location to attenuate signals with periods longer than 500 days are shown in the right panels (note the different color scale). The vertical white lines in the right panels delineate the longitudinal range over which equatorially trapped Rossby waves are investigated in Sections 4 and 5.
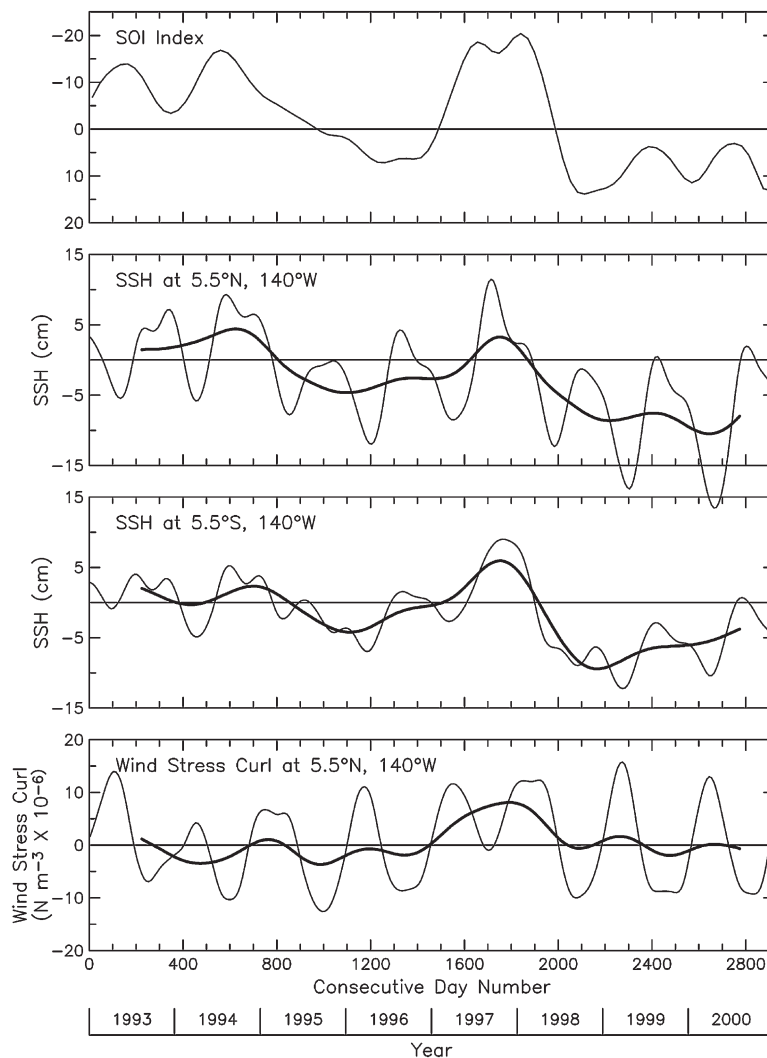
Fig. 4. Time series of the Southern Oscillation Index, low-pass filtered with a half-power cutoff of 300 days (top panel), SSH at 5.5° N, 140° W (second panel), SSH at 5.5° S, 140° W (third panel) and the wind stress curl at 5.5° N, 140° W computed from the analyzed surface wind fields from the European Centre for Medium-range Weather Forecasts numerical weather prediction model (bottom panel). The thin lines in the middle two panels are the $15° \times 2° \times 150$ - day smoothed and zonally high-pass filtered SSH and the thin line in the bottom panel is the $3° \times 2° \times 150$ - day smoothed wind stress curl. The heavy lines in all three bottom panels are the 500-day low-pass filtered variability of each time series. Note that the y axis is inverted in the top panel.

demise of the 1997–1998 El Niño and the transition to persistent La Niña conditions beginning in 1998, the mean SSH decreased by several centimeters compared with the mean SSH prior to 1997. This change of mean sea level occurred across most of the tropical Pacific (left and middle panels of Fig. 3); the negative westward propagating SSH signals after 1998 had much larger apparent amplitude than the positive SSH signals because of this negative shift of mean sea level.

Although interesting in its own right, an investigation of the post 1997–1998 El Niño drop in mean SSH is beyond the scope of this study. For present purposes, this interannual variability obscures the westward propagating SSH signals that are of interest here. We therefore temporally high-pass filtered the SSH at

each grid point to attenuate variability with periods longer than about 500 days by subtracting the low-frequency SSH obtained by applying a one-dimensional loess smoother with a half span of 500 days. The 500-day low-pass filtered SSH time series at 5.5° N, 140° W and 5.5° S, 140° W (heavy solid lines in the middle two panels of Fig. 4) reflect interannual variability likely associated with ENSO. The 500-day high-pass filtered time series obtained by subtracting these low-frequency SSH time series (heavy and thin solid lines in Fig. 5) exhibit a more regular seasonal cycle. The correlation between the 150–500-day band-pass filtered SSH at these two locations is 0.86. The amplitude of the variability at 5.5° N is about double that at 5.5° S (Fig. 5), a feature that is the focus of much of the analysis presented in Sections 4 and 6.

The three layers of filtering applied here to the TOPEX/POSEIDON data successfully isolate quasi-annual westward propagating SSH variability. Along both of the selected latitudes, westward propagation extends across the full width of the Pacific (right panels of Fig. 3). Although the character of the annual westward propagating SSH signals is noticeably altered during the 1997–1998 El Niño, quasi-annual Rossby waves are clearly present throughout the 8.5-year TOPEX/POSEIDON data record. Westward phase speeds along 5.5° N and 5.5° S vary somewhat longitudinally and from year to year.

As in the thermocline depth variability analyzed from XBT data by Meyers (1979) and Kessler (1990), the most energetic variability of fully filtered SSH is located in a zonal band that is centered at 5.5° N and extends across the full width of the Pacific (bottom panel of Fig. 2). Along this latitude, the variability is largest to the west of 170° E and smallest near 170° W with a broad zonal secondary maximum of SSH variability centered near 130° W. A weaker zonal band of locally high SSH variability also spans the Pacific south of the equator, centered near 5.5° S. This subtle southern hemisphere feature is not evident in the XBT data, most likely because of the sparse sampling of XBT data south of the equator. Except near 5.5° S in the far western Pacific, the standard deviation of the filtered SSH is much smaller everywhere south of the equator than north of the equator.

There is also energetic quasi-annual variability near 10° N in the far western Pacific and in several patches near 10° N in the eastern Pacific. The variability in these regions that are outside of the equatorial waveguide is apparently resonantly forced by the wind stress curl (Meyers, 1979; Kessler, 1990) and is thus unrelated to the equatorially trapped Rossby wave signals that are of interest here.

To investigate the sensitivity of results to the detailed specification of the filter parameters, we applied a variety of other filtering schemes to isolate the signals of interest here. Though clearest with the particular filtering summarized above, the energetic quasi-annual westward propagating SSH signals were readily apparent in all of these sensitivity studies. We feel confident that the conclusions of this study are not
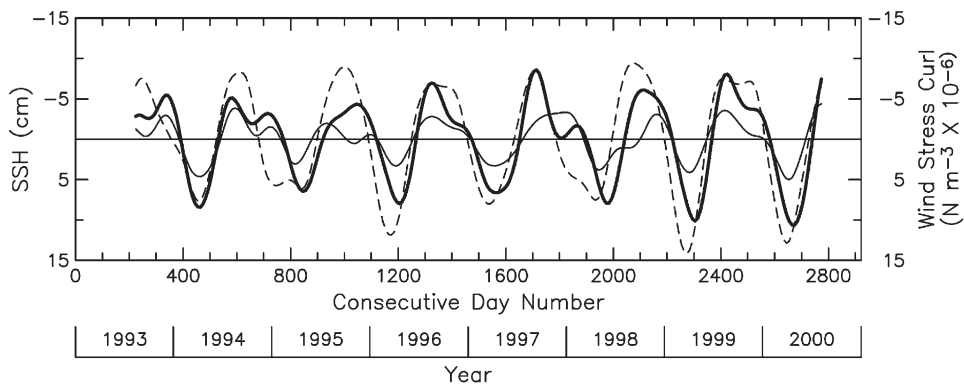

Fig. 5.   Time series of fully filtered SSH at 5.5° N, 140° W (heavy solid line) and 5.5° S, 140° W (thin solid line), and 3° × 2° smoothed and 150–500-day band-pass filtered ECMWF wind stress curl at 5.5° N, 140° W (dashed line). The wind stress curl is inverted (see the axis labels on the right side of the plot).

critically dependent on the precise details of the filtering. The fully filtered SSH obtained by the three-step filtering procedure described in detail above therefore forms the basis for the analysis of the latitudinal structure and westward phase speed of quasi-annual equatorially trapped Rossby waves presented in Sections 4 and 5.

3.2. Mean zonal velocity

The background mean zonal currents from which the effects of meridional shear on equatorially trapped Rossby waves are modeled in Section 6 were obtained from vertical sections of Acoustic Doppler Current Profiler (ADCP) measurements made between June 1985 and December 2000. A detailed discussion of the processing of these data to obtain estimates of the mean zonal velocity can be found in Johnson et al. (2002). A brief summary is given here.

Meridional sections of mean zonal velocity along the seven longitudes 110° W, 125° W, 140° W, 155° W, 170° W, 180° and 165° E are considered for the modeling studies in Section 6. Temporal sampling of these lines was irregular over the 16-year data record, with less frequent sampling between 5° S and 8° S, no measurements south of 8° S, and only infrequent sampling north of 8° N. At a depth of 150 m in the most frequently sampled latitude band between 5° S and 8° N, the typical number of ADCP measurements was about 15 along individual longitudes, with a maximum of 22 samples along 155° W and a minimum of 12 samples along 110° W. To improve the sampling at the expense of reduced zonal resolution, the ADCP data were smoothed longitudinally as described below.

Each ADCP section was objectively interpolated onto a regular grid in latitude and depth based on an assumed noise-to-signal variance ratio of 0.01 and a Gaussian autocovariance function with a latitudinal decorrelation scale of 1° and a vertical decorrelation scale of 25 m. The shallowest ADCP measurements were generally at a depth of 20 m. Velocities were extrapolated to the sea surface based on the shear in the upper water column. In combination with conductivity–temperature–depth (CTD) sections sampled simultaneously with the ADCP sections, the gridded zonal velocities were interpolated to a closely spaced latitudinal and isopycnal grid for statistical analysis. Isopycnal averaging is preferable to isobaric averaging because it preserves velocity extrema by reducing the 'smearing' effect that occurs in the statistics of variability computed at fixed isobaric surfaces in the presence of vertical motion of isopycnals.

Although there are 172 individual ADCP/CTD sections in the complete dataset, the number of measurements along each individual longitude (typically about 15, as noted above) is not adequate to average out the effects of unwanted signals such as aliasing of the unresolved and very energetic monthly variability associated with tropical instability waves and biased sampling of the interannual ENSO phenomenon. These sampling limitations were mitigated by smoothing the velocity measurements zonally by least-squares regression onto a quadratic function of longitude over a longitudinal span of 45° centered on the estimation longitude. For the nominal 15° longitudinal separation of the ADCP/CTD sections, the estimated zonal velocity thus incorporates measurements from the central longitude and the nearest neighboring longitudes to the east and to the west.

The above spatial regression was done concurrently with temporal regressions onto an annual cycle and a 5-month running average of the Southern Oscillation Index (SOI) of the ENSO phenomenon. The zonal velocity estimates were thus obtained from a 5-parameter multivariate regression of the velocity measurements at longitudes x, latitudes y, isopycnals ρ and times t onto a quadratic function of longitude, a harmonic with a period of $T = 1$ year, and the smoothed SOI index. The zonal velocity at a central longitude $x = 0$ was estimated by evaluating the resulting regression estimate

$$\hat{u}(x,y,\rho,t) = a_0 + a_1 x + a_2 x^2 + a_3 \sin(2\pi t/T) + a_4 \cos(2\pi t/T) + a_5 \text{SOI}$$

at the longitude $x = 0$. The regression coefficients a_i, $i = 0, \ldots, 5$ are all dependent on x, y and ρ. For the purposes of this study, only the mean zonal velocity is of interest. The mean zonal velocity as a function

of latitude and density is therefore estimated as $\hat{u}_0(y,\rho) = a_0$. By the explicit inclusion of their effects in the above formulation, annual variability and ENSO-related variability are effectively removed from these estimates of mean zonal velocity. For the applications in Section 6, the $\hat{u}_0(y,\rho)$ sections were interpolated onto a regular grid in depth z.

4. The observed latitudinal structures

Westward propagation is clearly evident along 5.5° N and 5.5° S across the full width of the Pacific in time-longitude plots of the fully filtered SSH (right panels of Fig. 3). Although disrupted during the 1997–1998 El Niño, negative SSH develops near the eastern boundary near the end of each year of the 8.5-year TOPEX/POSEIDON data record. These negative SSH signals propagate westward and arrive at the western boundary almost exactly a year later. The wavelengths of these westward propagating quasi-annual SSH signals are thus approximately equal to the width of the equatorial Pacific. As noted previously from Figs 4 and 5, this quasi-annual variability is not a simple harmonic; the durations of large negative SSH are only a few months whereas the durations of large positive SSH are about 6 months. The transition to positive SSH occurs in late spring or early summer at the eastern boundary.

For the purposes of this study, the most significant feature of the fully filtered SSH variability (right panels of Fig. 3) is the generally larger amplitude along 5.5° N than along 5.5° S. The difference is about a factor of two across most of the basin. The increase in amplitude west of the Dateline along 5.5° S is a notable exception. The equatorial asymmetry of SSH variability is quantified statistically in this section, which is organized as follows. The geographical structure and temporal evolution of the wind stress curl field is described in Section 4.1. The latitudinal structure of fully filtered SSH variability is determined in Section 4.2. The formalism for estimating the geostrophic velocity from SSH is summarized in Section 4.3 and the latitudinal structures of the zonal and meridional geostrophic velocity components are investigated in Sections 4.4 and 4.5. A theoretical explanation for the observed latitudinal asymmetries of all three of these variables across the eastern and central tropical Pacific, and the transition towards a more symmetric structure in the far western tropical Pacific, is later proposed in Section 6.

4.1. Wind stress curl

Geographical variations of the mean and standard deviation of the wind stress curl calculated over the 8-year period 1993–2000 from 150–500-day band-pass filtered 6-hourly surface wind analyses of the European Centre for Medium-range Weather Forecasts (ECMWF) are shown in Fig. 6. The strongest mean wind stress curl occurs within a band that is centered at about 10° N in the eastern Pacific and shifts equatorward to about 7° N in the western Pacific. This location is coincident with the region between the northern side of the ITCZ and the Northeast Tradewinds. The standard deviation of the quasi-annual wind stress curl variability is largest at lower latitudes in a zonal band centered at about 6° N that spans the full width of the Pacific. This variability is associated with strong seasonal variations of the latitude and intensity of the ITCZ, which migrates from its most southerly latitude in March to its most northerly latitude in September (Mitchell & Wallace, 1992).

As summarized in Section 2, the cross-equatorial asymmetry in the amplitude of annual equatorially trapped Rossby waves has been widely attributed to asymmetry in the annual wind forcing. While there can be no doubt that the observed westward propagating SSH variability in Fig. 3 is somehow generated by the wind, it is not necessarily obvious that the latitudinal asymmetry is attributable to direct forcing by asymmetric winds. The rationale for the oft-hypothesized direct wind forcing is apparently that the spatial distribution of wind stress curl variability (bottom panel of Fig. 6) is very similar to that of the fully filtered SSH (bottom panel of Fig. 2). A broad zonal maximum of wind stress curl variability is centered near
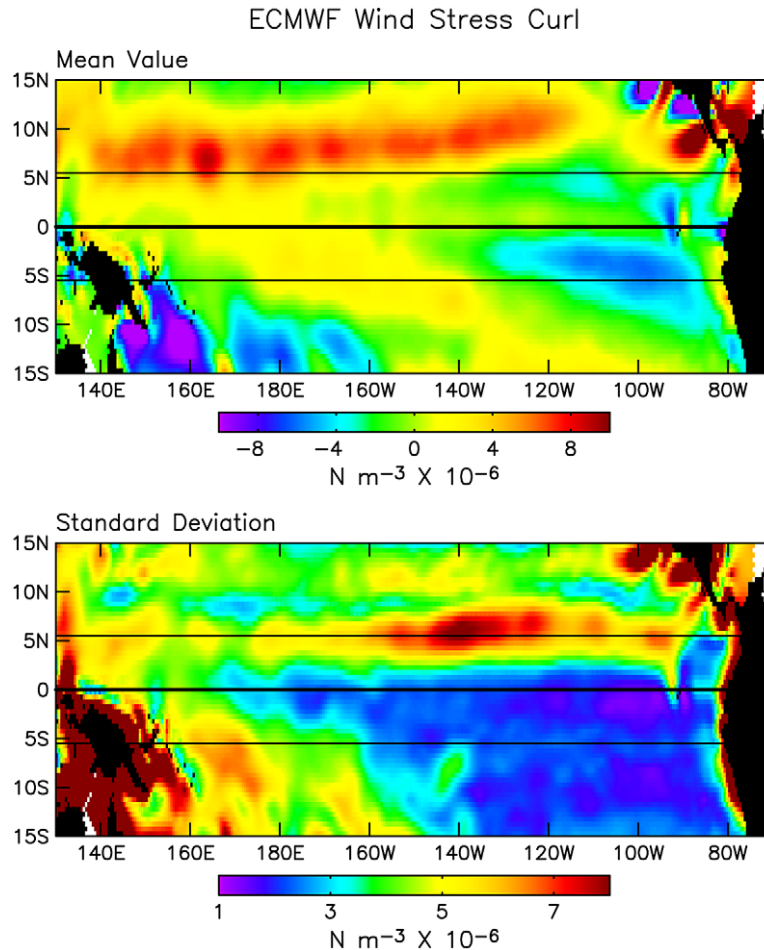
Fig. 6.   Geographical variation of the mean value and the standard deviation of the $3° \times 2° \times 150$ - day filtered ECMWF wind stress curl from 1993–2000.

6° N, 140° W, approximately coincident with the broad zonal maximum variability of fully filtered SSH. Except in the region of the South Pacific Convergence Zone in the western basin, there is virtually no wind stress curl variability south of the equator.

Although the spatial distributions of the standard deviations of wind stress curl and fully filtered SSH are very similar, the space-time evolutions of these two fields are quite different. The wind stress curl field along 5.5° N (right panel of Fig. 7) is positive across the entire Pacific from about February to April of each year. The onset of these positive wind stress curl conditions occurs a month or two earlier west of about 150° E and east of about 110° W and then propagates rapidly toward 170° W from both directions. The westward propagation across the eastern half of the basin is better defined than the eastward propagation across the western basin. The speed of the westward propagation is more than twice that of SSH variability along the same latitude (left panel of Fig. 7).

Over the eastern half of the basin, the durations of large positive wind stress curl are only a few months whereas the durations of large negative wind stress curl are about 6 months. As noted in Section 3.1, this asymmetry of the annual cycle is also evident in SSH (Figs 4 and 5). The fact that the durations of negative
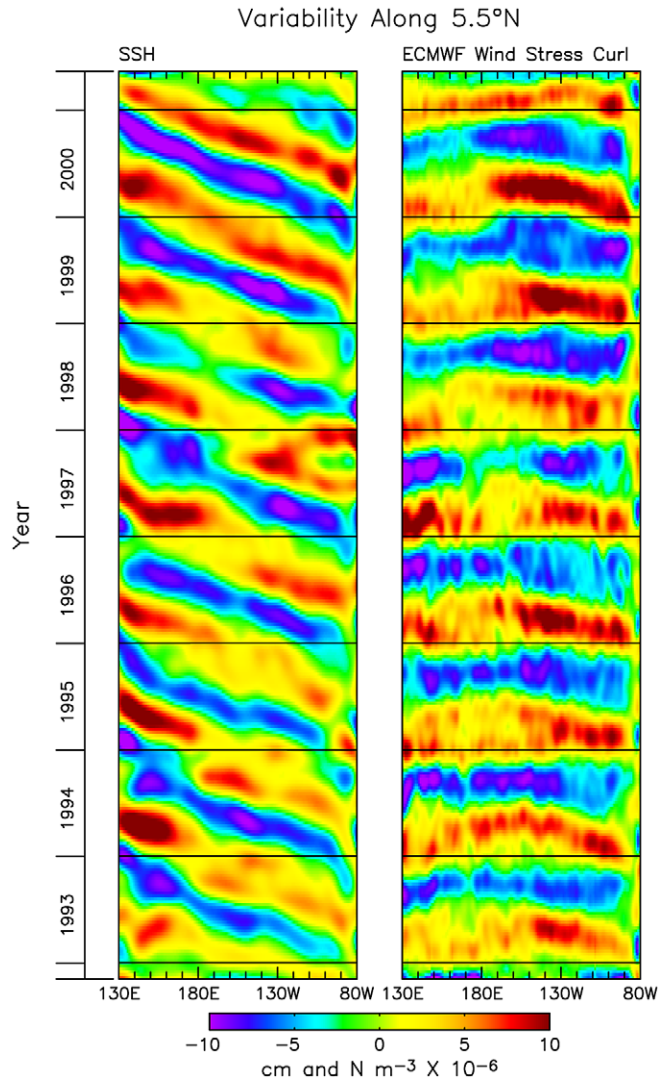
Fig. 7. Time-longitude plots of fully filtered SSH along 5.5° N (left, which is the same as the upper right panel of Fig. 3) and 3° × 2° smoothed and 150–500-day band-pass filtered ECMWF wind stress curl along 5.5° N (right).

SSH and positive wind stress curl are both about 3 months while the reverse phases of positive SSH and negative wind stress curl both have longer durations of about 6 months strongly suggests that the westward propagating SSH signals are somehow generated by the wind stress curl. This close relation between the temporal characteristics of SSH and wind stress curl is apparent at 140° W (Fig. 5). At this particular longitude, SSH at both 5.5° N and 5.5° S lags the negative of the local wind stress curl at 5.5° N by less than a month with correlations of 0.90 and 0.75, respectively.

Because of the monotonic westward propagation of SSH variability across the entire tropical Pacific and the more complex character of the wind stress curl forcing (rapid westward propagation across the eastern Pacific and eastward propagation across the western Pacific), the phase lag between SSH and the negative

of the local wind stress curl increases monotonically westward along 5.5° N (bottom panel of Fig. 8). The lag of maximum correlation between SSH and the negative of the local wind stress curl increases approximately linearly from about -50 days (SSH leading) at 95° W to about +50 days (SSH lagging) at 170° W. The phase lag increases abruptly to about +150 days near the Dateline and then increases approximately linearly to about +250 days (SSH lagging) at 140° E. Across this 125° range of longitudes, the lag between SSH and the local negative of the wind stress curl thus increases by about 300 days. The maximum lagged correlation (top panel of Fig. 8) increases from about 0.6 at 90° W to about 0.9 between 120 and 150° W, decreases to a local minimum of about 0.6 near the Dateline, and then increases to a local maximum of about 0.9 near 160° E. The maximum correlations between SSH at 5.5° S and the negative of the wind stress curl at 5.5° N along the same longitude are somewhat smaller but exhibit similar longitudinal variation. The lags of maximum correlation are very similar along both latitudes.
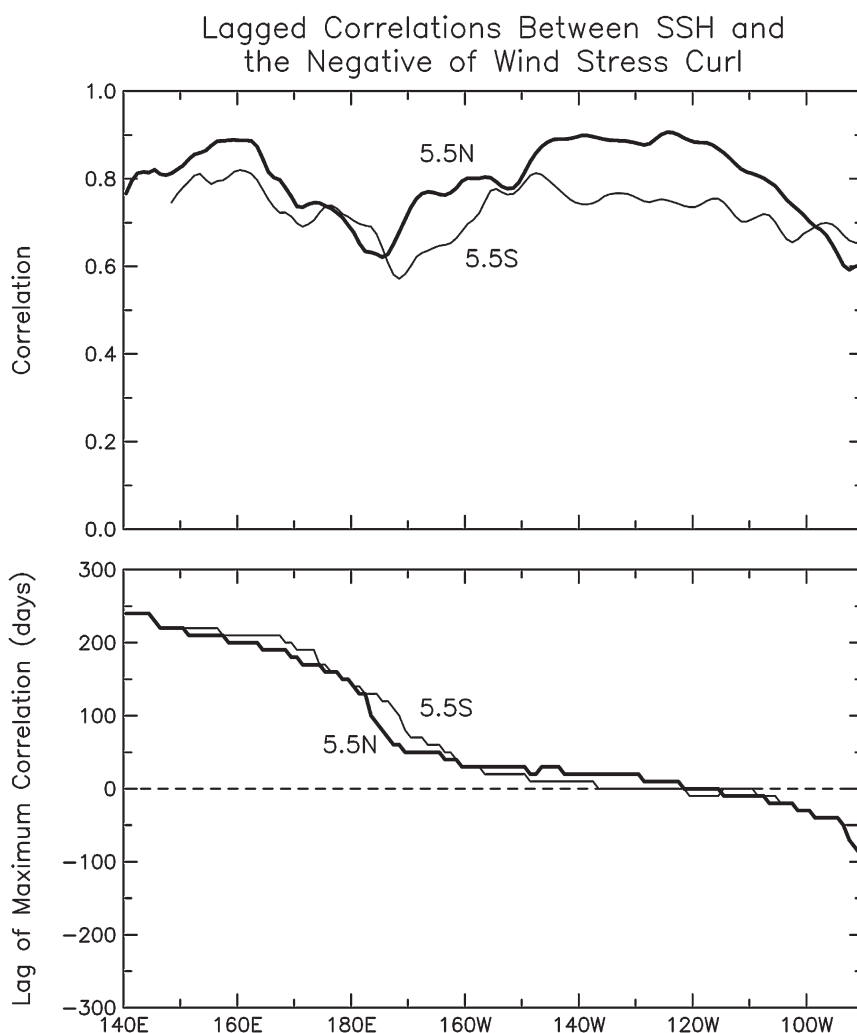

Fig. 8.   Longitudinal variation of the lagged correlations between the negative of the wind stress curl at 5.5° N at time t and SSH at 5.5° N (heavy lines) and 5.5° S (thin lines) at time $t + \tau$. Positive lags τ thus correspond to SSH lagging the negative of the wind stress curl. The maximum correlation and the lag of maximum correlation are shown in the top and bottom panels, respectively.
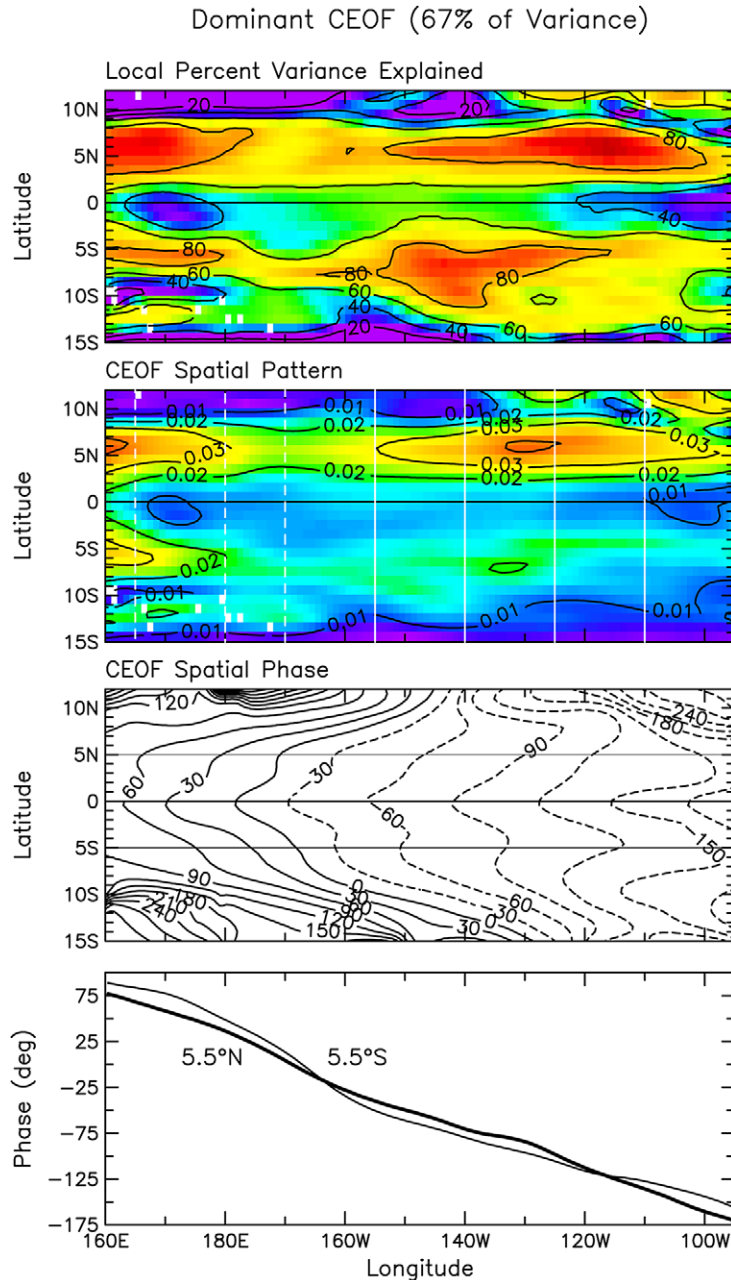
Fig. 9. The dominant Hilbert transform complex empirical orthogonal function (CEOF) of fully filtered SSH over the 6-year time period January 1994 through December 1999. This CEOF accounts for 67% of the variance summed over all grid points. The local percent variance accounted for by this mode at each grid point is shown in the top panel. The spatial amplitude and phase of the CEOF are shown in the second and third panels, respectively, and the longitudinal variations of the phase along 5.5° N and 5.5° S are shown in the bottom panel. The vertical solid and dashed white lines in the second panel indicate the longitudinal sections along which the EOFs were computed in Figs 12, 14 and 15. The theoretical eigenfunctions are determined along the white solid lines in Sections 6.3 and 6.4 and along the white dashed lines in Section 6.5.

The previous studies summarized in Section 2 have noted many of the features of the wind stress curl field described above, i.e., the small variability south of the equator, a band of maximum variability between 3 and 8° N in the eastern half of the Pacific and the near simultaneity of wind stress curl variations across the eastern Pacific within this latitude band. It is probably significant that the longitude of minimum correlation and off-resonance (near 180° phase lag) between SSH and the local wind stress curl coincides with the local minimum of SSH standard deviation near 170° W along 5.5° N (bottom panel of Fig. 2). Likewise, the relatively small phase difference between SSH and the negative of the local wind stress curl between about 100 and 170° W is indicative of near-resonant forcing, as suggested by Wang et al. (2000). This may explain the somewhat elevated SSH variability within this longitudinal band.

Whatever the mechanism is for wind generation of the observed quasi-annual equatorially trapped Rossby waves, the details are likely far more complex than can be addressed by the 1-dimensional forced-wave equation considered by Meyers (1979) and Kessler (1990). In particular, it is not at all clear how the wind forcing results in the observed asymmetry of the equatorially trapped waves. We are not aware of a rigorous demonstration of direct wind generation of asymmetric equatorial Rossby waves. To the contrary, the modeling study by Kessler and McCreary (1993) suggests that the asymmetry of the waves cannot be attributed simply to the equatorial asymmetry of the wind forcing per se. Their particular model was constrained to have zero background mean flow for which the free waves of the system are the Hermite solutions of the classical theory. When forced with asymmetric winds, this model was not able to generate asymmetric equatorial Rossby waves. The unforced model considered in Section 6 suggests that the asymmetric wind stress curl forcing is only indirectly responsible for the observed latitudinal structure of equatorial Rossby waves through its generation of asymmetric mean currents that alter the meridional gradient of potential vorticity that determines the latitudinal structure of the free waves of the system.

4.2. Sea surface height

The coherent westward propagation and cross-equatorial amplitude and phase structures of the fully filtered SSH variability can be concisely summarized by Hilbert transform complex empirical orthogonal function (CEOF) analysis (Barnett, 1983; Horel, 1984; Merrifield & Guza, 1990). In order to avoid potential edge effects in the zonally high-pass filtered SSH analyzed here and to minimize the impact of variability outside of the equatorial waveguide, the analysis is restricted to the geographical domain delineated by the white box in the bottom panel of Fig. 2 and by the vertical white lines in the right panels of Fig. 3. Likewise, to avoid potential problems with edge effects near the beginning and end of the 8.5-year TOPEX/POSEIDON data record in the 500-day high-pass filtered SSH analyzed here, only the central 6-year time period from January 1994 to December 1999 is considered.

The map of the dominant CEOF amplitude (second panel of Fig. 9) and the monotonic westward increase of its phase along all latitudes (third panel) demonstrate that this mode isolates the westward propagating SSH signal of interest. Except for two small patches north of 10° N in the eastern tropical Pacific and a less energetic patch south of 10° S in the western tropical Pacific, the variability associated with this mode is restricted to the equatorial waveguide. This mode accounts for 67% of the variance summed over all of the grid points within the geographical domain. The local percent variance explained is at least 60% throughout two zonal bands centered near 5.5° N and 5.5° S that span the full width of the domain (top panel of Fig. 9) and exceeds 80% in the regions of most energetic filtered SSH variability along both of these latitudes. Note especially that this CEOF accounts for 60–80% of the variance near 5.5° S, despite the small amplitude of the CEOF near this latitude.

The cross-equatorial asymmetry of the amplitude of the quasi-annual equatorially trapped Rossby waves is readily apparent from the dominant CEOF amplitude (second panel of Fig. 9); the amplitude along 5.5° N, for example, is about double that along 5.5° S across most of the domain. Along 5.5° N, the amplitudes of the westward propagating SSH signals are largest between about 100 and 155° W and to

the west of the Dateline and are smallest between about 155° W and the Dateline. The region of minimum CEOF amplitude along this latitude is coincident with the region of minimum standard deviation (bottom panel of Fig. 2). As discussed in Section 4.1, this also coincides with the longitudinal range of off-resonant forcing by the wind stress curl. As noted previously from the right panels of Fig. 3, the amplitude in the south increases to the west of the Dateline and becomes nearly as large as the amplitude in the north at the far western end of the domain considered in Fig. 9.

The CEOF phase (third panel of Fig. 9) is approximately symmetric about the equator with monotonic westward increase at all latitudes. With increasing latitude, the phase varies more rapidly longitudinally, indicative of decreasing westward phase speed. If the westward propagating signals consisted of a single equatorial Rossby wave mode, the phase speed would be latitudinally uniform across the equatorial waveguide. The observed latitudinal variation of phase speed can thus be interpreted as evidence of more than one meridional or vertical mode of variability. Within ±5° of the equator, the phase seldom varies latitudinally by more than about 30°, which suggests that the variability at these low latitudes is dominated by a single mode. At latitudes higher than about 7°, however, the phase along a given longitude increases rapidly with increasing latitude in the central and western regions. This is consistent with the slower phase speeds expected for higher-order meridional equatorial Rossby wave modes.

The greater significance of higher-order meridional modes at higher latitudes within the equatorial waveguide is not surprising. In the classical theory, the first meridional mode has maxima at about 4° N and 4° S and decays rapidly towards zero at higher latitudes (solid line in the top panel of Fig. 1). The SSH variability at higher latitudes must therefore be composed of higher-order meridional modes, which have maxima at increasingly high latitudes with increasing mode number (see, for example, Fig. A1 of Delcroix et al., 1994, for the latitudinal structures of SSH for the first three meridional modes of the classical theory). The westward phase speed of meridional mode m decreases as $(2m + 1)^{-1}$ in the classical theory. SSH variability at higher latitudes within the equatorial waveguide must propagate systematically slower with increasing latitude, just as it does in midlatitude Rossby wave theory.

While the presence of background mean currents quantitatively alters the latitudinal structures of the equatorial Rossby wave modes (see Section 6), the above argument is still valid. Higher-order shear-modified meridional modes with slower phase speeds are necessary to account for the variability at higher latitudes within the equatorial waveguide.

The cross-equatorial covariability of SSH inferred from the CEOF in Fig. 9 is further illustrated in Fig. 10. At all longitudes, the maximum cross correlation along the 5.5° N and 5.5° S latitudes of maximum
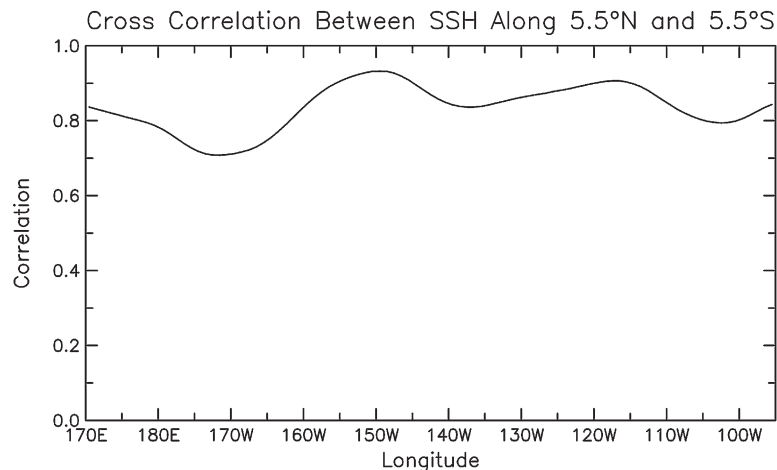

Fig. 10.   Longitudinal variation of the cross-equatorial correlation between fully filtered SSH along 5.5° N and 5.5° S.

SSH variability occurs at zero lag, evidence of the cross-equatorially coherent variability expected for equatorially trapped Rossby waves. Across most of the Pacific, the correlations between SSH variations along these latitudes range between 0.8 and 0.9. There is a local maximum of 0.93 at 150° W and a local minimum of 0.71 near 170° W. The approximately linear westward increases of the spatial phase of the dominant CEOF along 5.5° N and 5.5° S (bottom panel of Fig. 9) are indicative of narrow-banded signals in the wavenumber domain, which implies westward propagation of the covarying variability along these two latitudes. As discussed in detail in Section 5, the deviations from exact linearity can be interpreted as a measure of the zonal variation of the westward phase speed.

The amplitude time series of the dominant CEOF (top panel of Fig. 11) indicates a quasi-annual modulation of the westward propagating signal amplitude that is not necessarily apparent from the time-longitude plots of SSH in the right panels of Fig. 3; the westward propagating SSH signals are largest during the boreal spring and smallest during boreal autumn of each year. The two periods of smallest-amplitude quasi-annual variability occur a few months after the onsets of the 1994–1995 and 1997–1998 El Niño events (bottom panel of Fig. 11). El Niño effects are also apparent in the phase time series (middle panel of Fig. 11). Except for the two El Niño irregularities, the cyclical phase variation is very nearly linear in time with an annual periodicity over the 6-year time period. This annual cycle of the phase emphasizes the dominant quasi-annual nature of the SSH variability isolated by the 150–500-day filtering applied in Section 3.1.

For comparison with the local theoretical eigenfunctions obtained in Section 6, the latitudinal structures of observed SSH variability were determined locally along each of the seven longitudes at which the mean zonal velocity can be accurately estimated from the historical ADCP/CTD data summarized in Section 3.2.
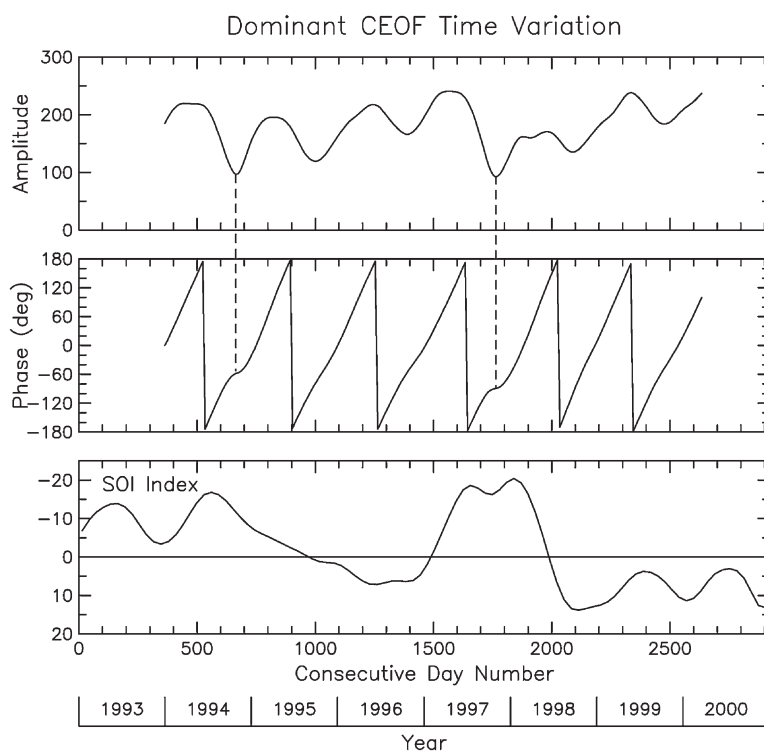

Fig. 11. The amplitude and phase time series (top and middle panels, respectively) of the dominant CEOF of fully filtered SSH shown in Fig. 9. The Southern Oscillation Index is shown in the bottom panel (note the inverted *y* axis).
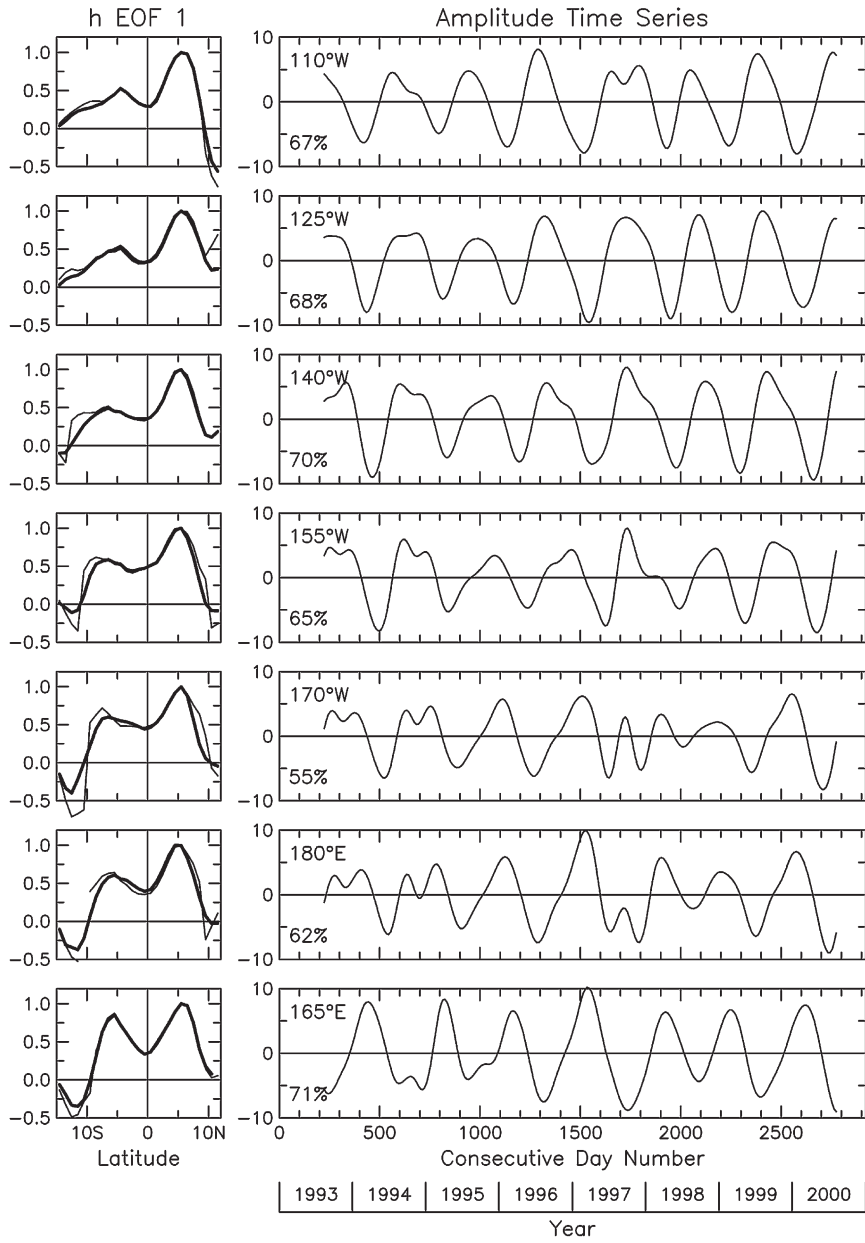
Fig. 12. The dominant empirical orthogonal functions (EOFs) (heavy solid lines in the left panels) and the associated amplitude time series (right panels) of fully filtered SSH computed separately along the longitudes indicated in the upper left corners of the right panels. The percentage of total variance along each longitude accounted for by the EOF is also labeled. The thin lines in the left panels (often indistinguishable from the heavy lines) are cross-sections of the CEOF amplitude adjusted for phase variation along the vertical solid and dashed white lines in the second panel of Fig. 9.

The time-domain empirical orthogonal functions (EOFs) (Preisendorfer, 1988) computed separately for each longitude (heavy lines in the left panels of Fig. 12) are very similar to meridional sections through the CEOF spatial amplitude and phase at these same longitudes (thin lines in Fig. 12). The latitudinal dependencies of the EOFs and CEOFs along each individual longitude are almost identical between 10° N and 10° S. At higher latitudes, the EOFs and CEOFs differ somewhat along some of the longitudes. For comparison with the theoretical eigenfunctions determined locally along each of these seven longitudes in Section 6, the EOFs are preferable to the CEOFs since they are computed locally rather than over the 2-dimensional domain shown in Fig. 9.

Along each of the seven longitudes, the maximum of the dominant EOF is centered at about 5.5° N. A local minimum is centered on the equator at all of the longitudes except 155° W where there is an insignificant shift to about 2° S. At all but the westernmost longitude of 165° E, the amplitude of the secondary maximum south of the equator is about half that of the maximum at 5.5° N. At 165° E, the southern maximum is much larger (about 85% of the amplitude of the northern maximum). At all longitudes, the southern maximum is somewhat less localized than the northern maximum. The precise locations of the broader southern maxima lie between 5° S and 7° S at all seven longitudes.

The latitudinal asymmetry of SSH variability inferred from time-longitude plots (Fig. 3), CEOF analysis (Fig. 9) and EOF analysis (Fig. 12) are inconsistent with both the latitudinal symmetry of first meridional mode equatorial Rossby waves of the classical theory and the latitudinal antisymmetry of the second meridional mode (top panel of Fig. 1). The observed latitudinal structures thus cannot be reconciled with any of the individual meridional modes of the classical theory. As discussed in Section 2, the observed asymmetric latitudinal structure of SSH can be described locally by a superposition of the first two meridional modes of the classical theory. However, the coherent westward propagation of the asymmetric SSH structures deduced from time-longitude analysis (Fig. 3) and CEOF analysis (Figs 9 and 11) is inconsistent with the 40% slower phase speed of meridional mode 2 relative to that of mode 1.

The amplitude time series of the EOFs along each of the seven longitudes (right panels of Fig. 12) are dominated by annual variability with a phase that increases westward. The maximum cross correlations between the seven time series range from higher than 0.9 for the closely spaced sections to about 0.7 for the widely separated sections. The lags of the maximum cross correlations are analyzed in Section 5 to estimate the westward phase speed of the SSH signatures of equatorially trapped Rossby waves.

4.3. Geostrophic velocity estimation

The characteristics of equatorially trapped Rossby waves can be further investigated from the velocity variability associated with the waves. While direct observations are not available to determine the latitudinal structures of velocity variability, the surface geostrophic velocity variability can be estimated from the fully filtered SSH fields derived in Section 3.1. The geostrophic relations for the surface zonal and meridional geostrophic velocity components u and v are

$$u = -\frac{g}{f}\frac{\partial h}{\partial y} \tag{1}$$

$$v = \frac{g}{f}\frac{\partial h}{\partial x} \tag{2}$$

where g is the gravitational acceleration, f is the Coriolis parameter and h is the sea surface height. These relations were shown long ago to be adequate to within 0.5° of the equator (e.g., Knauss, 1960; Arthur, 1960). Near the equator where f approaches zero, the measurement accuracy becomes very demanding. At latitude 0.4°, for example, an error of only 1 mm of SSH change over a distance of 100 km is equivalent to a geostrophic velocity error of 0.1 m s^{-1}.

At the equator $y = 0$, where $f = 0$, the expression (1) for the zonal geostrophic velocity becomes singular unless $\partial h/\partial y|_{y=0} = 0$. Even with this constraint, u cannot be evaluated at the equator from (1). Jerlov (1953) and Tsuchiya (1955) noted that a solution for u at the equator can be derived by differentiating (1) to obtain

$$f \frac{\partial u}{\partial y} = g \frac{\partial^2 h}{\partial y^2} - \beta \frac{g}{f} \frac{\partial h}{\partial y} = g \frac{\partial^2 h}{\partial y^2} + \beta u$$

where $\beta = df/dy$ is the latitudinal variation of the Coriolis parameter. Evaluating this expression at $y = 0$ yields

$$u|_{y=0} = - \frac{g}{\beta} \frac{\partial^2 h}{\partial y^2}. \tag{3}$$

The zonal geostrophic velocity at the equator can thus be estimated from the meridional curvature of the SSH field. Because of the second derivative in (3), this expression for u at the equator is extremely sensitive to measurement errors in SSH.

As suggested by Picaut and Tournier (1991), nonsingularity of (1) can be assured by defining a 'corrected' SSH as

$$\hat{h}(y) = h(y) + h'(y),$$

where

$$h'(y) = A \, y \, e^{-(y^2/L^2)}$$

and the constant A is

$$A = -\partial h/\partial y|_{y=0}.$$

Picaut and Tournier (1991) recommend a value of $L = 2°$ of latitude for the e-folding scale in the expression for h'. In addition to eliminating the singularity in (1), this Gaussian meridional smoothing of the SSH field near the equator mitigates to some extent the effects of measurement noise in the first and second meridional derivatives of h in (1) and (3). With h replaced with $\hat{h}$, the zonal geostrophic velocity for the analysis presented in Section 4.4 was estimated from (1) away from the equator and from (3) on the equator. This technique has previously been applied to Geosat altimeter data by Delcroix et al. (1991, 1994).

Although a method analogous to (3) could be derived to estimate v close to the equator, the meridional velocity perturbations associated with equatorial Rossby waves are about an order of magnitude smaller than the zonal velocity perturbations (see Fig. 13 below). Because of this much lower signal-to-noise ratio, estimates of v are more sensitive to measurement errors in h. Measurement noise was found to be too large to obtain useful estimates of v closer than $2°$ from the equator. While useful outside of this latitude band, it will become apparent in Section 4.5 that estimates of v are somewhat noisier than estimates of u.

4.4. Zonal geostrophic velocity

Latitudinal profiles of the zonal geostrophic velocity are not entirely independent of the latitudinal profiles of SSH obtained in Section 4.2 since $u(y)$ is calculated from $h(y)$ by (1) and (3). Because of the derivative relationships, $u(y)$ is effectively a spatially high-pass filtered version of $h(y)$. Zonal geostrophic velocity
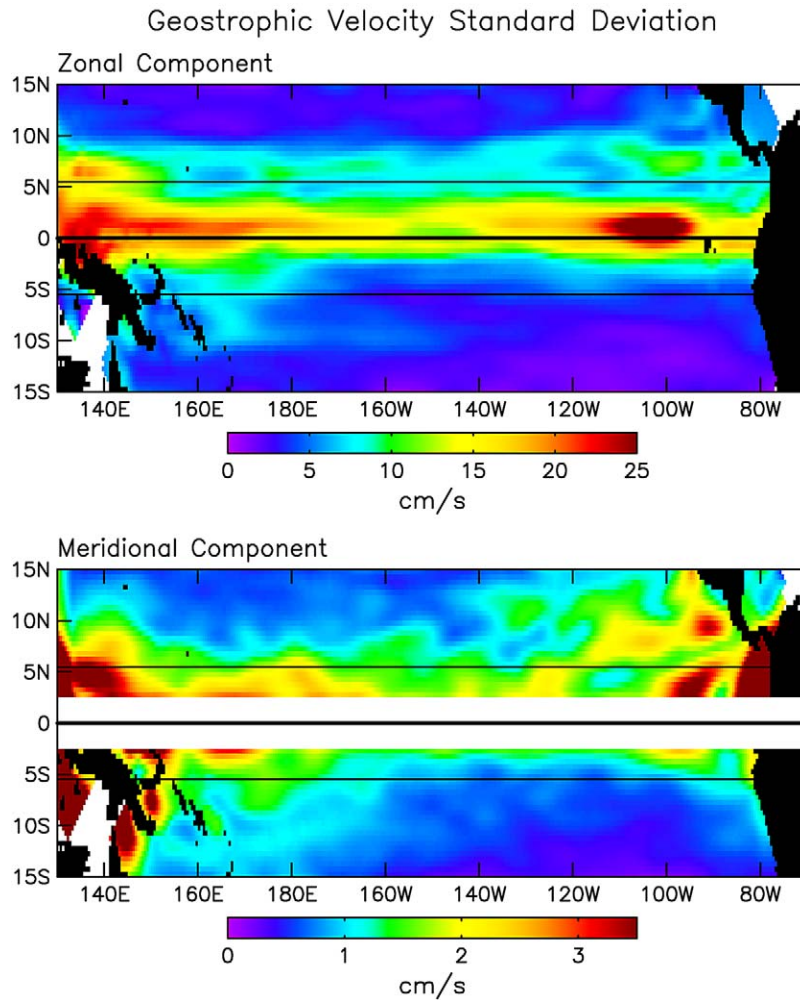
Fig. 13.   Geographical variation of the standard deviations of the zonal and meridional components of geostrophic velocity computed from the fully filtered SSH fields as described in the text.

is a more stringent characterization of the latitudinal structure of equatorially trapped waves in the TOPEX/POSEIDON data since any noise in $h(y)$ will be amplified in the meridional derivatives. Moreover, because the weighting factor f in (1) varies latitudinally, the linear relation between $u(y)$ and $h(y)$ varies significantly across the 10° N to 10° S latitude range of interest here. The EOFs of $u(y)$ therefore provide useful additional insight that augments the information about equatorial Rossby waves inferred from $h(y)$.

The zonal velocity computed as summarized above exhibits strong latitudinal asymmetry with large variability occurring within a band between the equator and about 3° N (upper panel of Fig. 13). This geographical pattern of the standard deviation of u is very similar to that reported by Delcroix et al. (1994) from 3 years of Geosat altimeter data. Within this latitude band, the variability of u is smallest in the central Pacific between about 140 and 170° W. The maximum standard deviation of u exceeds 0.25 m s^{-1} near 1° N between 95 and 110° W. The variability between 4 and 10° N is typically about 0.10 m s^{-1}.
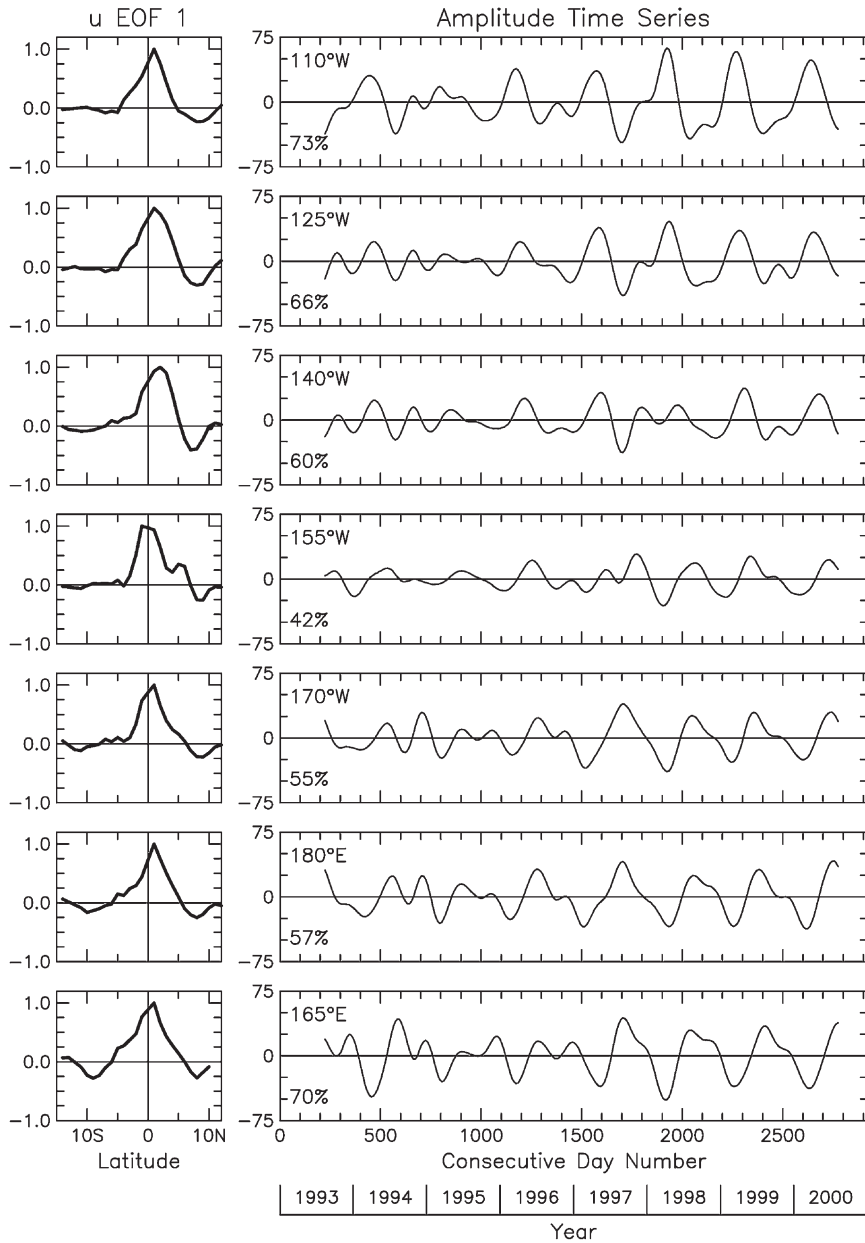
Fig. 14.   As in Fig. 12, except for the dominant EOFs (left panels) and the associated amplitude time series (right panels) of zonal geostrophic velocity computed from SSH as described in the text.

The most striking feature in the standard deviation of *u* is the very weak variability south of the equator everywhere to the east of the Dateline.

The latitudinal structure of *u* was determined as in Section 4.2 from the EOFs along each of the seven longitudes considered in this analysis (Fig. 14). Except at 155° W where the *u* variability is smallest (upper panel of Fig. 13) and, therefore, most susceptible to measurement noise in *h*, the maxima of the EOFs
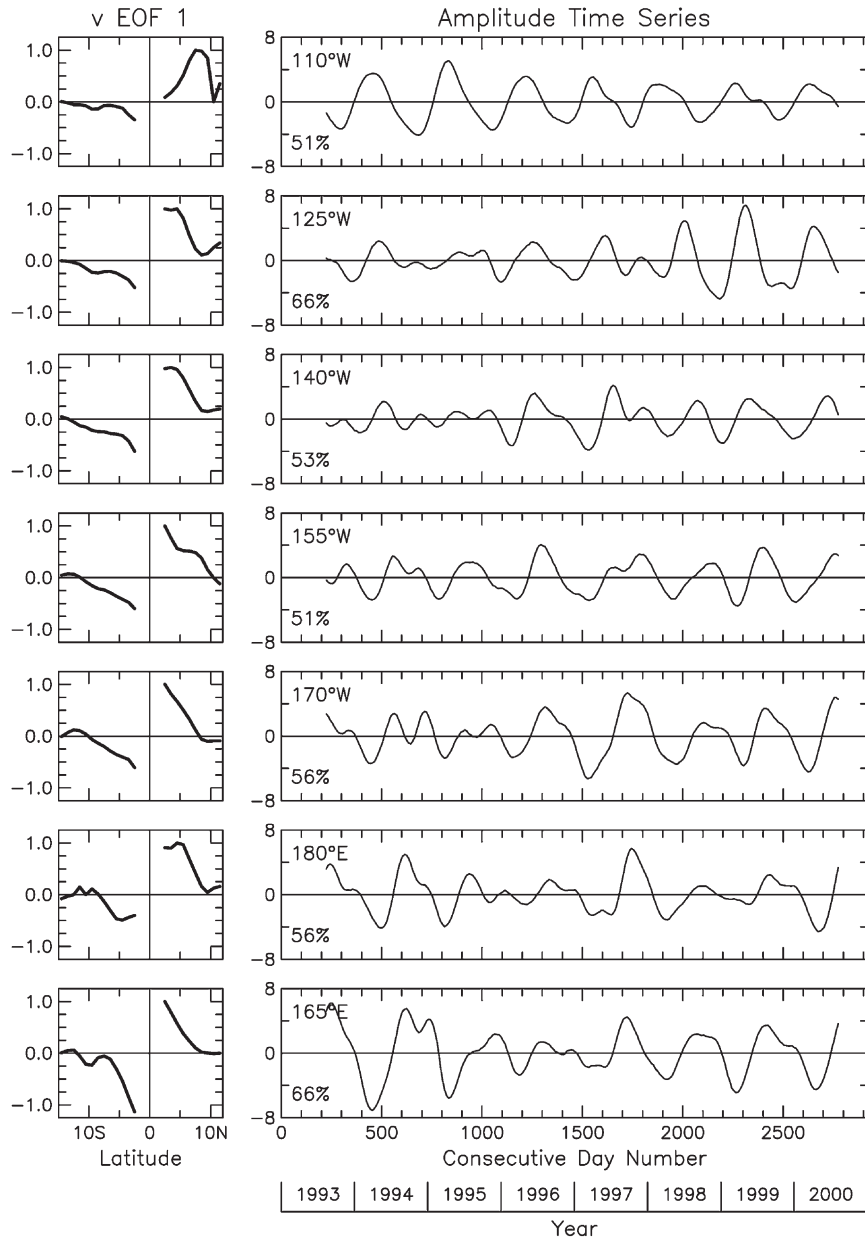
Fig. 15.   As in Fig. 12, except for the dominant EOFs (left panels) and the associated amplitude time series (right panels) of meridional geostrophic velocity computed from SSH as described in the text.

along each longitude are located 1–2° north of the equator. The broad central maxima are flanked by secondary extrema of opposite sign centered near 7.5° N. These latitudinal structures are very similar to the meridional profile of *u* estimated by Delcroix et al. (1991) from Geosat data along 145° W in June 1987. At the westernmost longitude of 165° E and, to a lesser extent, at the Dateline, there is a second negative extremum centered near 8° S. Elsewhere across the Pacific, the EOFs have insignificant amplitude south of about 3° S.

The EOFs of zonal velocity (Fig. 14) are roughly similar to the symmetric structure of *u* in the first meridional mode equatorial Rossby wave of the classical theory (solid line in the bottom panel of Fig. 1). The important distinction from the classical structure is the latitudinal asymmetry with the central maxima shifted somewhat north of the equator, strong negative extrema on the north flank of these central maxima, and much smaller or nonexistent negative extrema south of the equator. The EOFs of *u* bear even less resemblance to the antisymmetric structure of *u* in the second meridional mode (dashed line in the bottom panel of Fig. 1). As in the case of the SSH EOFs, the observed latitudinal structure of *u* therefore cannot be reconciled with any of the individual meridional modes of the classical theory.

4.5. Meridional geostrophic velocity

Since meridional velocity is calculated from zonal derivatives of SSH by (2), the latitudinal profiles $v(y)$ are more nearly independent of $h(y)$ than are the $u(y)$ profiles considered in Section 4.4. The standard deviation of meridional velocity (lower panel of Fig. 13) is apparently largest in the latitude band between 2° S and 2° N within which useful estimates of *v* cannot be obtained from the SSH data. The standard deviations of *v* are almost an order of magnitude smaller than those of *u* throughout the equatorial waveguide, seldom exceeding 0.03 m s^{-1} across most of the Pacific. Exceptions to this occur in the far eastern Pacific near the coast of Colombia, to the north of the Galapagos Islands, to the east of 120° W in the latitude band between 5 and 10° N that is influenced by the Papagayo wind jet (Chelton et al., 2000), and in the far western Pacific. These features in the variability of *v* are likely related to processes other than the equatorially trapped Rossby waves that are of interest here.

The most important conclusion that can be drawn from the lower panel of Fig. 13 is that, except in the regions noted above, the standard deviation of *v* is asymmetric with larger amplitude north of the equator across the eastern and central Pacific. Along 5.5° N, for example, the standard deviation of *v* is about a factor of two larger than along 5.5° S everywhere east of the Dateline.

At the easternmost longitude of 110° W, the first EOF of *v* (Fig. 15) is dominated by variability centered at about 7.5° N that is associated with wind forcing by the Papagayo wind jet noted previously from Fig. 13. The structure of the EOF of *v* along 110° W is therefore not representative of the equatorially trapped Rossby waves of interest here and will not be considered further in this analysis.

Along the other six longitudes, the EOFs of the meridional velocity (Fig. 15) at latitudes where useful estimates can be obtained outside of the immediate equatorial region exhibit discrepancies with the latitudinal antisymmetry of *v* in the first meridional mode equatorial Rossby wave of the classical theory (solid line in the middle panel of Fig. 1) that are analogous to the discrepancies in the observed latitudinal structures of *h* and *u*. Bearing in mind the much greater sensitivity of the estimates of *v* to measurement errors in *h*, the consistency of the EOFs of *v* at these other six longitudes is remarkable. The observed *v* perturbations vary out of phase north and south of the equator, roughly similar to the classical solution for *v* in the first meridional mode, except that the amplitudes of variability south of the equator are smaller than those north of the equator at all but the westernmost longitude of 165° E. The observed variability of *v* thus exhibits equatorial asymmetry that is similar in character to that observed in *h* and *u*. The cross-equatorial phase structure is distinctly different from the latitudinal symmetry of *v* in the second meridional mode (dashed line in the middle panel of Fig. 1). Thus, as in the case of the EOFs of *h* and *u*, no individual mode of the classical theory is able to account for the observed latitudinal structure of *v*.

5. The observed phase speeds

The lags of maximum cross correlation between the *h*, *u* and *v* EOF amplitude time series (Figs 12, 14 and 15) offer three estimates of the westward phase speed (Fig. 16). While the 10-day discretization of
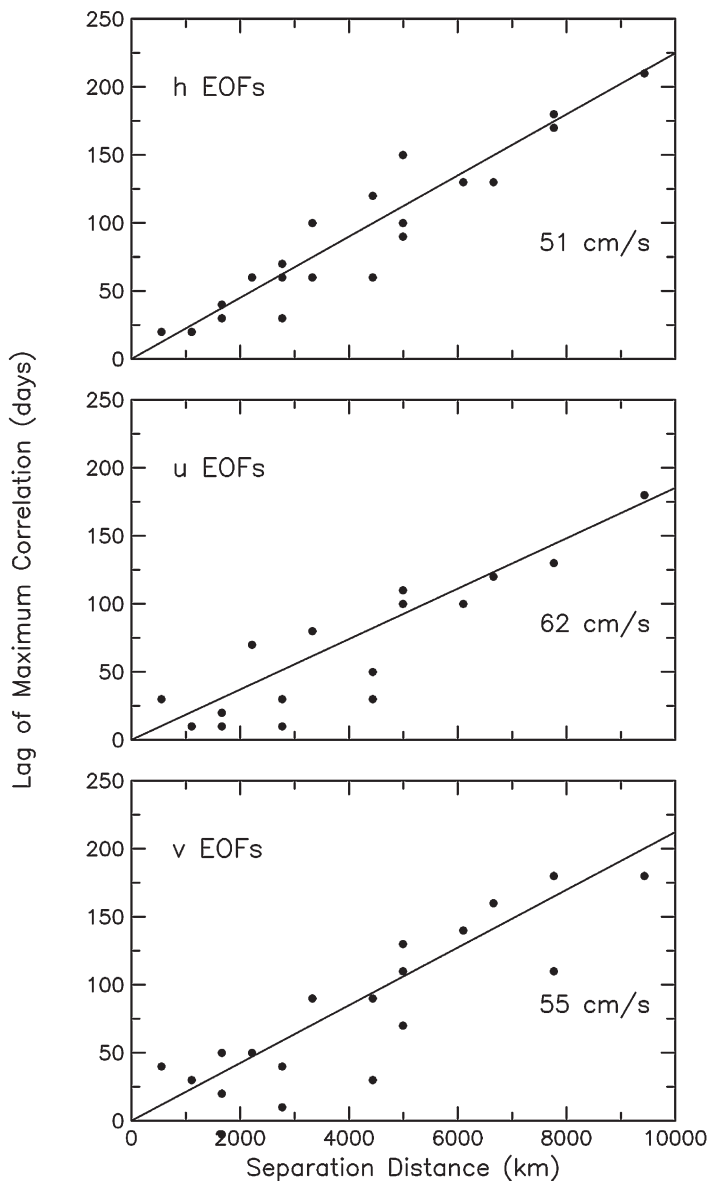
Fig. 16.   The lag of maximum cross correlation between the amplitude time series of the EOFs (right panels of Figs 12, 14 and 15) of SSH (top) zonal geostrophic velocity (middle) and meridional geostrophic velocity (bottom), displayed as a function of the zonal separation of the longitudes along which the EOFs were computed. The straight line constrained to pass through the origin in each panel was fit to the data by least squares. The corresponding westward phase speeds are labeled in each panel.

the smoothed and filtered TOPEX/POSEIDON time series analyzed here limits the precision of the time resolution with which the lagged cross correlations can be determined, it is clear from Fig. 16 that the lags of maximum cross correlation increase with increasing separation of the observation longitudes for all three variables. Least-squares fits of the data points in each panel to lines constrained to pass through the origin indicate westward phase speeds of 0.51, 0.62 and 0.55 m s^{-1} deduced from the *h*, *u* and *v* EOF amplitude time series, respectively.

The classical theory for equatorially trapped Rossby waves predicts a phase speed of $c_1/(2m + 1)$ for low-frequency (nondispersive) first vertical mode waves, where m is the meridional mode number and c_1 is the phase speed of the first baroclinic internal gravity wave. The value of c_1 for the equatorial region is about 2.7 m s^{-1} (Chelton et al., 1998; see also Fig. 17 below). The observed phase speeds deduced from the h, u and v EOF amplitude time series are thus consistent with the approximate 0.55 m s^{-1} phase speed of low-frequency second meridional mode Rossby waves. However, it has been shown in Section 4 that the observed latitudinal structures of the h, u and v EOFs do not exhibit the cross-equatorial phase symmetries of these variables in the second meridional mode Rossby waves of the classical theory. The observed westward propagating h, u and v signals are therefore inconsistent with an interpretation as second meridional mode Rossby waves.

The cross-equatorial phase structures of the observed variability presented in Section 4 more closely match those of the first meridional mode of the classical theory for all three variables. However, the asymmetric amplitude structures (larger in the north than in the south) and the approximate 0.5–0.6 m s^{-1} phase speeds are not consistent with the symmetric amplitude structure and ~0.9 m s^{-1} phase speed of the classical first meridional mode equatorial Rossby wave. The classical theory is evidently lacking both in its description of the latitudinal structure and the phase speed of equatorially trapped Rossby waves.

The phase speed of the observed westward propagating SSH signals can be independently estimated from the time-longitude plots of SSH variability in the right panels of Fig. 3. Close inspection of the westward propagating SSH signals reveals that the phase speeds vary somewhat from year to year and increase somewhat to the west of about 170° E during some years. These variations are especially apparent along 5.5° S.

To avoid biases from the faster phase speeds in the far western Pacific, attention is restricted here to

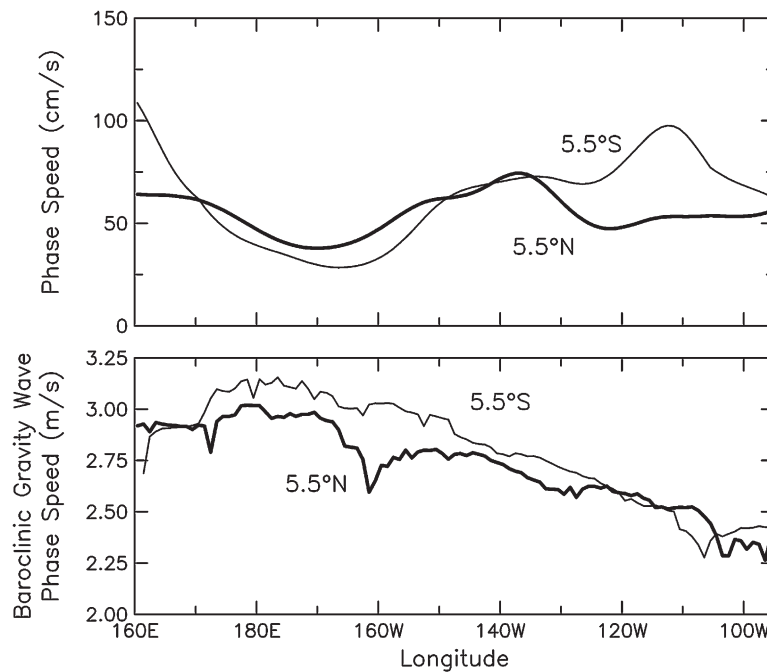Fig. 17. The longitudinal variations of the phase speed of westward propagation along 5.5° N (heavy solid line) and 5.5° S (thin solid line) computed from the CEOF spatial and temporal phase variations as described in the text (upper panel). The lower panel shows the longitudinal variation of the first internal gravity wave phase speed c_1 from Chelton, de Szoeke, Schlax, El Naggar and Siwertz (1998) along the same latitudes.

the interior ocean in the longitude range from 125° W to 170° E. The westward phase speeds along 5.5° N and 5.5° S were estimated from the Radon transform (Deans, 1983). A formalism for the uncertainty of the Radon transform in this setting has not been developed. Lacking a quantitative basis, we have somewhat arbitrarily defined the uncertainty to be the range of phase speeds for which the magnitude of the Radon transform exceeds 95% of its maximum value. With this definition of the uncertainty, the estimated westward phase speeds are 0.60 ± 0.15 m s^{-1} along 5.5° N and 0.48 ± 0.10 m s^{-1} along 5.5° S. The phase speed estimates obtained here are very similar to the estimates of 0.6 and 0.4 m s^{-1} obtained along 5° N and 7° S, respectively, by Susanto et al. (1998) from 32 months of TOPEX/POSEIDON data. The phase speed estimate along 5.5° N is also almost identical to the value of 0.58 m s^{-1} estimated by both Meyers (1979) and Kessler (1990) from XBT data along 6° N.

The phase speeds can also be estimated from the CEOF analysis in Section 4.2. As summarized in detail by Merrifield and Guza (1990), for example, the dominant period and wavelength of the westward propagation can be estimated, respectively, from the reciprocal of the temporal slope of the CEOF phase time series in the middle panel of Fig. 11 and the reciprocal of the spatial slope of the CEOF phase variation in the bottom panel of Fig. 9. From the very nearly exact annual repeatability of the temporal slope variation, the dominant period of the waves is clearly annual. The deviations from exact linearity of the CEOF spatial phase variations in the bottom panel of Fig. 9 are thus indicative of zonally varying wavelength, and therefore of zonally varying phase speed computed as the ratio of the wavelength to the period.

The zonal variations of the westward phase speed were estimated along 5.5° N and 5.5° S based on running least squares fits of straight lines to the spatial CEOF phase variation along each latitude and assuming annual periodicity. The phase speeds along the two latitudes (upper panel of Fig. 17) are very similar between about 130° W and 170° E. Using the standard deviations of the phase speed estimates between 170° E and 130° W as rough measures of uncertainty, the mean values of the phase speeds along 5.5° N and 5.5° S are 0.55 ± 0.12 m s^{-1} and 0.52 ± 0.18 m s^{-1}, respectively. The phase speed estimates from the dominant CEOF are thus consistent with the estimates obtained above from the Radon transform of the time-longitude plots in the right panels of Fig. 3.

The geographical variations of phase speed along both 5.5° N and 5.5° S are likely attributable to variations in ambient conditions. One possible candidate is geographical variations of the stratification, which is embodied in the internal gravity wave phase speed c_1. This quantity increases approximately monotonically westward along both latitudes with a smaller value along 5.5° N than along 5.5° S (lower panel of Fig. 17). One therefore might expect the equatorially trapped Rossby wave phase speed to be somewhat slower along 5.5° N, which is opposite to what is inferred both from the Radon transforms and the CEOF analysis. Likewise, one might expect the phase speeds along both latitudes to be highest between 150° W and 170° E, whereas the CEOF analysis indicates that the phase speeds are slowest in this longitude range. Geographical variations in the background mean density field evidently cannot account for the observed geographical variations of the phase speed of equatorially trapped Rossby waves. We are unable to offer an explanation for the zonal variations and latitudinal differences of the westward phase speeds deduced here from analyses of TOPEX/POSEIDON data. They may be related to geographical variations of the wind forcing or to geographical variations or annual fluctuations of the background mean currents.

6. The theoretical latitudinal structures

The inability of the classical theory to explain the observed meridional structure of westward propagating variability should not be surprising since it is based on an assumed background state of rest. The zonally banded currents in the tropical Pacific have mean zonal velocities with meridional shears that are among the highest in the world ocean. The meridional shears are very strong between the Equatorial Undercurrent (EUC) and the southern branch of the South Equatorial Current (SECS), between the EUC and the northern

branch of the South Equatorial Current (SECN), and between the SECN and the North Equatorial Countercurrent (NECC). Moreover, the latitudinal variation of the relative vorticity of these meridionally sheared mean zonal currents is as strong or stronger than the β contribution to the total potential vorticity gradient that is the restoring mechanism for equatorially trapped Rossby waves (see Figs 18 and 23 below). The effects of the background mean currents on the eigenfunctions and dispersion characteristics of equatorially trapped Rossby waves clearly cannot be ignored.

This section is organized as follows. Previous theoretical studies of the effects of meridionally sheared currents on equatorially trapped Rossby waves are summarized in Section 6.1. The simple 1.5-layer model used here to investigate the effects of the observed equatorial current system on the latitudinal structure and dispersion characteristics of first-meridional mode baroclinic Rossby waves is summarized in Section 6.2. The sensitivity of solutions of the 1.5 layer eigenvalue equations to various estimates of the upper-layer mean zonal velocity profile $U(y)$ along 140° W is discussed in Section 6.3. The salient features of the shear-modified eigenfunctions are shown to be only moderately sensitive to the details of the averaging scheme used to define $U(y)$. Eigensolutions for the other three longitudes considered here in the eastern Pacific (110° W, 125° W and 155° W) are presented in Section 6.4. Eigensolutions for the three western longitudes (170° W, 180° and 165° E) are considered separately in Section 6.5 because they are fundamentally different from those computed for the eastern half of the tropical Pacific.

6.1. Theoretical background

The effects of the meridional profile of mean zonal velocity in the equatorial current system on low-frequency equatorially trapped wave solutions were first investigated by Philander (1979). He considered a narrow, equatorially symmetric eastward jet in a 1.5-layer model. The strong lateral shears on the flanks of this vertically averaged representation of the EUC appreciably alter the dispersion relation and latitudinal structure of equatorially trapped Rossby waves. In particular, the existence of the EUC decreases the westward phase speeds of the waves, broadens the eigenfunctions and shifts their maxima to higher latitudes compared with the Hermite function solutions of the classical theory that assumes that $U(y) = 0$. Boyd (1978) showed the same broadening and shift to higher latitudes for equatorial Rossby waves in the atmosphere in the presence of a symmetric jet centered on the equator. More recently, Proehl (1990) considered the effects of symmetric mean flows on long equatorial Rossby waves in a continuously stratified ocean. As in the simple 1.5-layer model considered by Philander (1979), the latitudinal structure of meridional mode 1 equatorial Rossby waves expanded meridionally in the presence of an EUC.

The equatorially symmetric zonal velocity profiles $U(y)$ considered by Philander (1979), Boyd (1978) and Proehl (1990) cannot account for the observed asymmetry of westward propagating SSH variability presented in Section 4. McPhaden and Knox (1979) investigated the effects of a realistic asymmetric mean zonal flow in a 1.5-layer model, but considered only the Kelvin and first two inertia-gravity wave modes. The mean flow significantly Doppler shifted the phase speed of low-frequency Kelvin waves but had little effect on the latitudinal structure of the waves. The latitudinal structures of h, v and u for the inertia-gravity waves were also only slightly sensitive to the background mean currents. This is because the turning latitude at the high frequencies of inertia-gravity waves is close to the equator. The mean zonal flow is very nearly symmetric within the narrow waveguide of equatorial inertia-gravity waves, thus limiting the ability of the background shears to induce asymmetric latitudinal structures of h, v and u.

Chang and Philander (1989) considered the effects of an equatorially asymmetric meridional profile of mean zonal velocity on equatorial Rossby waves. Their $U(y)$ profile included meridional shear associated with the SEC and the NECC. They showed that the mean vortex stretching effect of the upward slope of the mean thermocline toward the equator in association with the westward geostrophic mean SECN reduces the ambient potential vorticity gradient, and hence the westward phase speeds of equatorially trapped
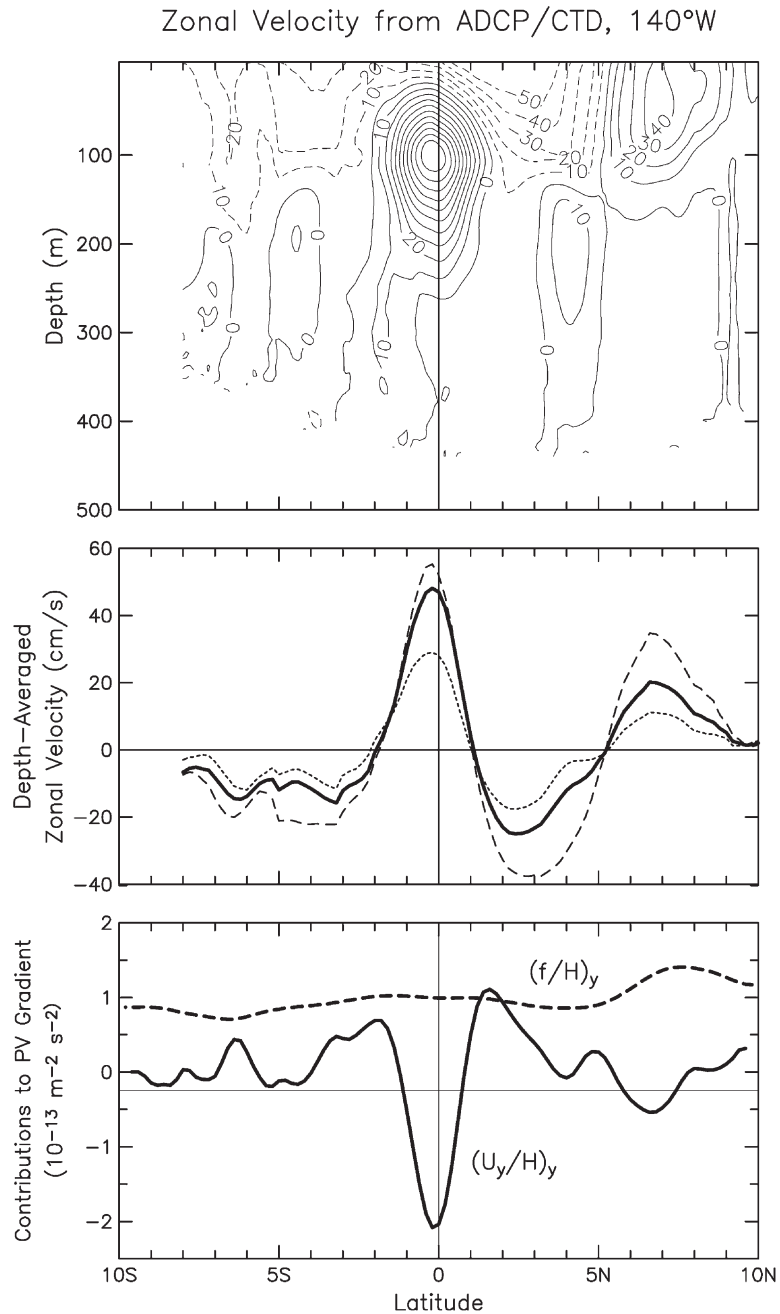
Fig. 18.   Vertical section of the mean zonal velocity estimated from ADCP/CTD data along 140° W (top). The contour interval is 10 cm s^{-1}. The zonal velocity profiles $U(y)$ are shown in the middle panel for vertical averages over the upper 150 m (dashed line), 250 m (heavy solid line) and 400 m (dotted line). The planetary and relative vorticity contributions $(f/H)_y$ and $(U_y/H)_y$ to the meridional gradient of potential vorticity for the 250-m average $U(y)$ are shown in the bottom panel by the dashed and solid lines, respectively.

Rossby waves. The effects of meridional shear on the latitudinal structure of the eigenfunctions were not considered in that study.

Most recently, Zheng et al. (1994) considered the effects of strong latitudinal shear in an idealized representation of an equatorially asymmetric current system. They found that the mean relative vorticity in the shear region between the SEC and NECC also decreases the ambient potential vorticity gradient and thus reduces the westward phase speeds of equatorially trapped Rossby waves. The effects of the meridionally sheared equatorial current system on the latitudinal structure of the eigenfunctions were not considered in that study either.

All previous studies of oceanic low-frequency equatorially trapped Rossby waves have thus concluded that the dispersion characteristics are altered in such a way as to reduce the westward phase speeds of baroclinic equatorially trapped Rossby waves. It is noteworthy that this is the opposite of the effects of the mean flow on extra-tropical Rossby waves. At latitudes higher than about 10° N, baroclinic Rossby wave phase speeds are increased by the vortex stretching contribution of the vertically sheared background mean zonal flow to the meridional gradient of potential vorticity (Killworth et al., 1997; Dewar, 1998; de Szoeke & Chelton, 1999). This distinction between the effects of mean currents on tropical and extra-tropical Rossby waves is consistent with the observed latitudinal variation of Rossby wave phase speeds (Chelton & Schlax, 1996; see also Section 3.4 of Fu & Chelton, 2001).

While the effects of realistic equatorially asymmetric mean currents on the dispersion relation have previously been considered, their effects on the latitudinal structures of low-frequency equatorial Rossby wave eigenfunctions have not yet been studied in the ocean. Boyd (1982) studied an analogous problem in the atmosphere. He considered the effects of meridional shears associated with a midlatitude northern hemisphere wind jet on the barotropic first and second meridional mode planetary-scale barotropic waves on a sphere. The spherical eigenvalue equation for these planetary waves has a form very similar to that for baroclinic oceanic Rossby waves on an equatorial β plane. For zero mean flow, the latitudinal structure of the geopotential for the first meridional mode is symmetric about the equator with maxima at about 40° N and 40° S, similar to the Hermite solution for baroclinic equatorially trapped Rossby waves except displaced to much higher latitudes, as expected for the barotropic mode. In the presence of a Gaussian easterly jet centered at 45° N, the latitudinal structure of the barotropic planetary waves became asymmetric with the amplitude of the southern maximum only about half that of the northern maximum.

For the baroclinic first-meridional mode oceanic equatorial Rossby wave considered in Sections 6.3–6.5, the westward flow of the SECN evidently plays a role similar to that of the northern mid-latitude easterly jet in the barotropic planetary wave problem considered by Boyd (1982). When the SECN is strong, as it is in the eastern and central Pacific, the latitudinal structure of the first meridional mode Rossby wave is asymmetric with larger amplitude north of the equator (see Sections 6.3, 6.4). When the SECN is absent, as in the western Pacific, the latitudinal structure of the first meridional mode Rossby wave is symmetric (see Section 6.5), albeit with maxima shifted to higher latitude and broadened in the presence of the EUC (Philander, 1979; Proehl, 1990).

Although the effects of asymmetric mean zonal flow on the latitudinal structures of oceanic equatorial Rossby waves have not been investigated theoretically for low-frequency waves, such wave-mean flow interaction has received considerable attention in studies of tropical instability waves (TIWs). A detailed summary of the extensive literature on TIWs is beyond the scope of this study. The interested reader is referred to Chelton et al. (2003) for a review. The 20–40-day periodicities of TIWs are very far from the low-frequency portion of the wavenumber–frequency spectrum that is of interest in this study of quasi-annual equatorial Rossby waves. The results of theoretical studies of TIWs are therefore not of direct relevance here. For present purposes, it suffices to note that realistic asymmetric mean zonal currents considerably alter the latitudinal structures of TIWs, resulting in much larger amplitudes north of the equator than south of the equator. It might be anticipated that the asymmetric mean flow of the Pacific equatorial current system significantly alters the structure of low-frequency equatorial Rossby waves as well. This is

investigated here from the very simple model of the baroclinic structure of the tropical Pacific summarized in Section 6.2. The results are compared in Sections 6.3–6.5 with the observed meridional structures and phase speeds estimated in Sections 4 and 5 from the TOPEX/POSEIDON data.

6.2. Reduced-gravity model formulation

The dynamics of the observed h, u and v signatures of westward propagating variability are investigated here from the 1.5 layer reduced-gravity model used by Philander (1979). While this is a rather crude representation of the baroclinic structure of the equatorial Pacific, it provides a simple formulation that yields useful insight into the importance of meridional shear in the background mean currents to the latitudinal structure and phase speed of low-frequency equatorial Rossby waves. Here, the equations are linearized about the observed background mean zonal velocity rather than just the symmetric EUC considered by Philander (1979). By restricting attention to a mean zonal flow that depends only on latitude, the equations remain separable in the y–z plane. The resulting eigenvalue equation for the latitudinal eigenmodes cannot be solved analytically, but solutions can be obtained numerically.

The upper-layer equations, linearized about a mean zonal flow $U(y)$ on an equatorial β plane, are

$$\left(\frac{\partial}{\partial t} + U\frac{\partial}{\partial x}\right)u + \left(\frac{\partial U}{\partial y} - \beta y\right)v + g'\frac{\partial h}{\partial x} = 0 \tag{4}$$

$$\left(\frac{\partial}{\partial t} + U\frac{\partial}{\partial x}\right)v + \beta y u + g'\frac{\partial h}{\partial y} = 0 \tag{5}$$

$$\left(\frac{\partial}{\partial t} + U\frac{\partial}{\partial x}\right)h + \frac{\partial}{\partial y}(vH) + H\frac{\partial u}{\partial x} = 0, \tag{6}$$

where u and v are the zonal and meridional components of the perturbation velocity, h is the perturbation depth of the layer interface (a scaled mirror image of SSH perturbations), β is the meridional gradient of the Coriolis parameter, g' is the reduced gravity, and $H(y)$ is the meridional variation of the mean thickness of the layer, which is specified here to be in geostrophic balance with the mean zonal velocity $U(y)$. The values used here for g' and the latitudinally averaged mean thickness of the upper layer (which will be denoted here as H_1) were specified as described in detail in Section 6.3 and are almost identical to the values considered by Philander (1979).

With boundary conditions of no meridional flow at northern and southern boundaries (taken here to be $y_N = 20°$ N and $y_S = 20°$ S), Eqs. (4)–(6) can be combined to obtain a single second-order differential equation that is a Sturm–Liouville eigenvalue problem for any one of the three state variables h, u or v. Finite-difference solutions of the resulting equation yield extraneous, nonphysical solutions (Proehl, 1991). This problem was circumvented here by simultaneously solving the system of first-order partial differential Eqs. (4)–(6) directly in all three state variables (Proehl, 1996).

Zonally propagating wave solutions with wavenumber k and frequency ω have the form

$$\begin{pmatrix} h \\ u \\ v \end{pmatrix} = \begin{pmatrix} A_h(y) \\ A_u(y) \\ A_v(y) \end{pmatrix} e^{i(kx-\omega t)}$$

where $A_h(y)$, $A_u(y)$ and $A_v(y)$ are the latitudinally varying amplitudes of the wave-induced h, u and v perturbations. Solutions were obtained numerically for the (possibly complex) frequency eigenvalues ω as

a function of specified zonal wavenumber k. The dispersion relation is obtained from solutions at closely spaced intervals of k. The associated eigenfunctions for a specific k represent the latitudinal structures of the wave solutions for h, u and v at that wavenumber. Exponentially growing unstable solutions are represented by negative values of the imaginary part of ω.

In the applications in Sections 6.3–6.5, unstable solutions had periodicities much shorter than the annual period that is of interest here. The existence of these instabilities would tend to stabilize the mean currents through conversion of mean kinetic energy to eddy kinetic energy, potentially altering the background mean currents that affect the latitudinal structure and phase speed of equatorial Rossby wave solutions at all wavenumbers. This alteration of the background mean flow is counteracted by the tendency of the asymmetric wind forcing to re-establish the sheared mean currents. This interaction between the mean flow, the wind forcing and the unstable waves complicates the definition of the mean zonal velocity profile $U(y)$ in the 1.5-layer model Eqs. (4)–(6). A sensitivity analysis found that the salient features of the latitudinal structure of quasi-annual equatorial Rossby waves are not strongly sensitive to variations of $U(y)$ (see Section 6.3). For the purposes of this study, we feel that the 16-year average zonal velocity sections derived from the ADCP data as summarized in Section 3.2 are adequate.

The 1.5 layer Eqs. (4)–(6) were solved locally at each of seven longitudes (the vertical solid and dashed white lines in the second panel of Fig. 9). Local solutions implicitly assume that the background stratification and mean zonal velocity fields do not change as the waves propagate to the west. Along the four eastern longitudes of 110° W, 125° W, 140° W and 155° W, the mean zonal currents averaged over the upper 250 m are similar (see the middle row of Fig. 22 below). The 250-m averaged mean zonal currents along the three western longitudes of 170° W, 180° and 165° E are also similar as a group (see the middle row of Fig. 25 below), but differ substantially from the currents in the eastern tropical Pacific. In particular, the EUC is weaker and the SECN is nonexistent in the western tropical Pacific, resulting in 250-m averaged mean zonal velocity profiles $U(y)$ with weak meridional shear north of the equator. It can therefore be anticipated that the eigensolutions will change as the waves propagate into the western tropical Pacific. The validity of the local solutions of the eigenvalue problem will be assessed by comparing the resulting eigenfunctions with the EOFs of observed h, v and u variability along each longitude (Figs 12, 14 and 15).

6.3. Eigensolutions along 140° W

We first consider in detail the solutions of Eqs. (4)–(6) along 140° W. The Pacific equatorial current system is well represented in the ADCP/CTD mean zonal velocity section, $\hat{u}_0(y,z)$, along 140° W (top panel of Fig. 18). The EUC is centered at 0.2° S and 105 m depth with a maximum velocity of 1.1 m s^{-1}. The SEC is split by the EUC into surface-intensified northern and southern branches centered at about 3° N and 4° S with maximum westward velocities of about 0.6 and 0.3 m s^{-1}, respectively. The eastward flow of the NECC is centered at about 7° N and 60-m depth with a maximum velocity of about 0.45 m s^{-1}.

In the simple 1.5-layer model considered here, it is necessary to average the zonal velocity field vertically to define the upper-layer mean zonal velocity profile $U(y)$ about which Eqs. (4)–(6) are linearized. The inherently subjective nature of the choice for how the vertical average is constructed is addressed later in this section by considering the sensitivity to several different averaging schemes. To include the effects of the EUC that Philander (1979) showed exerts a significant influence on the eigensolutions of Eqs. (4)–(6), we consider first the latitudinal profile of the upper-ocean mean zonal velocity $U(y)$ obtained by averaging the zonal velocity $\hat{u}_0(y,z)$ over the upper 250 m of the ADCP/CTD section (heavy solid line in the middle panel of Fig. 18).

The restoring mechanism for Rossby waves is the meridional gradient of ambient potential vorticity, Q. For the 1.5-layer model considered here, this is

$$\frac{\partial Q}{\partial y} = \frac{\partial}{\partial y} \left(\frac{f - \partial U / \partial y}{H} \right).$$

Denoting the meridional derivative by the subscript y, the contribution $(U_y/H)_y$ is derived from the mean relative vorticity in the 250 m average zonal velocity profile $U(y)$. Owing to the narrow bands of opposing zonal flow in the SECS, EUC and SECN, $(U_y/H)_y$ has an amplitude as large or larger than the combined planetary vorticity and vortex stretching contribution, $(f/H)_y$, within a few degrees of the equator (bottom panel of Fig. 18). In the region between the EUC and the SECN at about $2°$ N, $(U_y/H)_y$ has the same sign as $(f/H)_y$ and is slightly larger in magnitude. The ambient potential vorticity gradient Q_y is thus negative in this region. This change in sign in the latitudinal profile of Q_y is a necessary condition for instability. Unstable solutions were indeed obtained with growth rates on the order of a month at wavelengths shorter than 1000 km, presumably related to the well-known tropical instability waves (Philander, 1978). These are much shorter than the 10 000 km and longer wavelengths of the quasi-annual variability that are of interest here. As summarized in Section 6.2, the tendency toward stabilization of the background mean flow by these instabilities is offset by the tendency toward re-establishment of the shears by the wind forcing. The 16-year average $U(y)$ profile therefore seems appropriate for assessment of the effects of mean flow on quasi-annual equatorial Rossby waves.

The value of the reduced gravity g' in (4) and (5) was specified based on the first-baroclinic gravity wave phase speed of $c_1 = 2.7$ m s^{-1} deduced from historical hydrographic data in this region (Chelton, de Szoeke, Schlax, El Naggar & Siwertz, 1998). The reduced gravity was computed from this value of c_1 and the vertical averaging depth $H_1 = 250$ m by the relation $g' = c_1^2/H_1$. As another practical consideration in the solution of Eqs. (4)–(6), the meridional profile of 250-m averaged zonal velocity along $140°$ W was smoothed somewhat meridionally in order to minimize the amplification of noise in the derivatives of $U(y)$ that are implicit in Eqs. (4)–(6). The $U(y)$ profile was also specified as zero outside of the $8°$ S to $10°$ N latitudinal range of the ADCP/CTD velocity sections.

The eigenfunctions for the state variables h, v and u based on the smoothed 250 m average $U(y)$ profile and the above value of g' (heavy solid lines in Fig. 19) can be compared with those computed numerically from Eqs. (4)–(6) with $U(y) = 0$ (heavy dotted lines). For the case of zero background mean velocity, the eigenfunctions for v are the Hermite functions obtained analytically for the first baroclinic mode with a gravity wave phase speed of $c_1 = 2.7$ m s^{-1}. The eigenfunctions for h and u are linear combinations of Hermite functions (Moore & Philander, 1977; Philander, 1990). The observed background equatorial currents significantly alter the meridional structure of the eigenfunctions. Like the observed variability of h along $140°$ W (Fig. 12), the shear-modified eigenfunction for h is equatorially asymmetric with a maximum amplitude north of the equator that is about twice the amplitude of the secondary maximum south of the equator. This character is distinctly different from the symmetric structure of the classical Hermite function solution for h. The asymmetric structure is very similar to that of the shear-modified atmospheric barotropic planetary wave considered by Boyd (1982), though with an expected very different meridional scale. The maxima of the oceanic baroclinic equatorial Rossby waves considered here are shifted about $1°$ higher in latitude than the maxima of the Hermite function solution. As noted in Section 6.1, Philander (1979) and Proehl (1990) have previously shown that this latitudinal broadening is attributable to the presence of the EUC.

The shear-modified eigenfunction for v (middle panel of Fig. 19) is very nearly antisymmetric in phase, with a zero crossing slightly north of the equator. As with the h eigenfunction, the extrema of the v eigenfunction are asymmetric in amplitude (larger in the north than in the south) and are shifted about $1°$ higher in latitude compared with the Hermite function solution. Although observational knowledge of the latitudinal structure of v is incomplete owing to the equatorial gaps in the EOFs of the estimated geostrophic meridional velocity in Fig. 15, it is clear that they are very similar outside of this gap to the structure of
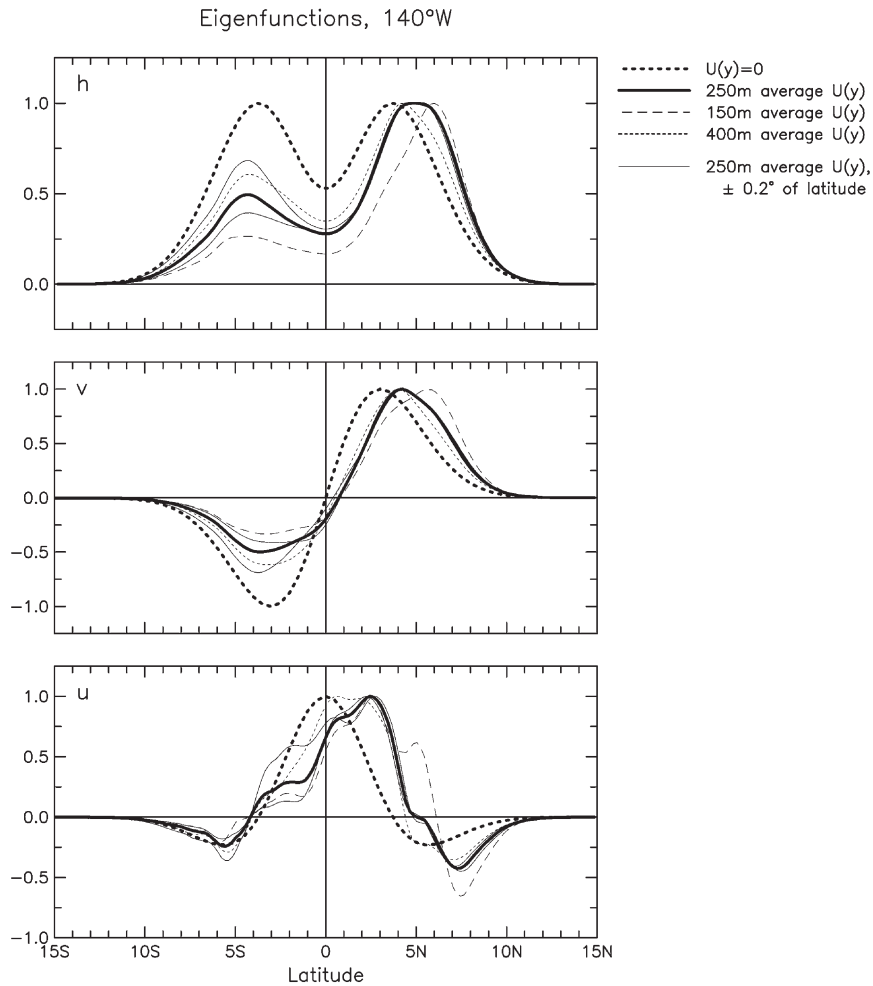
Eigenfunctions, 140°W

Fig. 19.   The eigenfunctions for *h*, *v* and *u* computed from the 1.5 layer β-plane Eqs. (4)–(6) linearized about the vertically averaged mean zonal velocity along 140° W. The heavy dotted lines represent the Hermite function solutions of the classical theory. The thin dashed, heavy solid and thin dotted lines are the shear-modified eigenfunctions computed from mean zonal velocity averaged over the upper 150, 250 and 400 m, respectively. The two thin solid lines are the shear-modified eigenfunctions computed from latitudinal shifts of the 250-m vertically averaged zonal velocity by 0.2° north (the eigenfunction with the larger southern amplitude) and 0.2° south.

the eigenfunction for *v* shown in Fig. 19. In particular, the positive amplitude north of the equator is about a factor-of-two larger in magnitude than the negative amplitude south of the equator.

The shear-modified eigenfunction for *u* (bottom panel of Fig. 19) is distinctly different from the eigenfunction for the case of zero mean background flow. Both eigenfunctions have the same number of zero crossings and a general resemblance between the shear-modified eigenfunction and the Hermite function solution is readily apparent. However, the latitudes of the central maximum and the negative northern extremum of the shear-modified eigenfunction are both shifted by more than 2° to the north of their counterparts in the Hermite function solution. The negative northern extremum is about twice as large in amplitude as that of the Hermite function solution. In contrast, the negative southern extrema for both solutions are located at the same latitude and have the same amplitude. These features of the *u* eigenfunction are all

very similar to the observed latitudinal structure in the EOFs of the estimated geostrophic zonal velocity shown in Fig. 14. The small irregularities in the detailed structure of the shear-modified eigenfunction for u are attributable to residual noise in the smoothed $U(y)$ profile that is amplified in the derivatives that are implicit in the relationship between the u eigenfunction and the mean zonal velocity profile $U(y)$.

Since it includes essentially the full vertical extent of the EUC, vertically averaging over the upper 250 m seems a logical definition for the mean upper-layer velocity $U(y)$ in the 1.5-layer model Eqs. (4)–(6). It is not obvious *a priori*, however, that this is the best choice. We therefore investigated the sensitivity of the solutions of Eqs. (4)–(6) to the depth range over which the mean zonal currents are averaged. Eigenfunctions were computed with $U(y)$ obtained from vertical averages over the upper 150 and 400 m (see, respectively, the dashed and dotted lines in the second panel of Fig. 18). These averaging depths H_1 and the baroclinic gravity wave phase speed of $c_1 = 2.7$ m s^{-1} define the value of $g' = c_1^2 / H_1$ in (4) and (5).

The eigenfunctions computed from the 150 and 400 m vertically averaged currents are qualitatively very similar to those obtained based on the 250-m average (Fig. 19). In particular, all three depth-averaging schemes yield h and v eigenfunctions with extrema that are smaller in amplitude south of the equator than north of the equator. In the 150-m average case (dashed lines in Fig. 19), the stronger representation of the equatorial current system results in a somewhat larger cross-equatorial asymmetry in the amplitudes of the h and v eigenfunctions with northern maxima shifted about 1° higher in latitude. The noisier u eigenfunction is likely attributable to a greater sensitivity to noise in the shallow 150-m averaged $U(y)$ profile. In the 400-m average case (dotted lines in Fig. 19), the weaker representation of the equatorial current system results in somewhat decreased cross-equatorial asymmetry in the amplitudes of the h and v eigenfunctions and a shift of about 1° south in the location of the northern maximum of the h eigenfunction.

To investigate further the sensitivity of the eigenfunctions to the detailed specification of the meridional velocity profile $U(y)$, the 1.5 layer Eqs. (4)–(6) were solved based on ±0.2° latitudinal shifts of the 250-m average $U(y)$ profile. The meridional structures of the eigenfunctions for h, v and u (thin solid lines in Fig. 19) are somewhat less sensitive to these lateral shifts of the zonal current system than they are to the depth range over which the zonal velocity is averaged. North of the equator, the changes of the eigenfunctions relative to those obtained from the non-shifted $U(y)$ profile are imperceptible for all three state variables. South of the equator, however, there are noticeable changes in the structures of the eigenfunctions. The southward shift of $U(y)$ increases the asymmetry of the eigenfunctions by reducing the amplitude of the southern maxima in the h and v eigenfunctions and reducing the amplitude of southern flank of the central peak of the u eigenfunction. The northward shift of $U(y)$ has the opposite effects on the h, v and u eigenfunctions.

Overall, the salient features of the eigenfunctions are the same for all five of the $U(y)$ profiles considered here: The h and v eigenfunctions are consistently asymmetric in amplitude with larger amplitude north of the equator. The primary maximum of the u eigenfunctions is consistently located north of the equator and the negative extremum north of the equator is consistently larger in amplitude than the negative extremum south of the equator.

Of the three averaging depths considered here, the 250 m average zonal velocity profile yields eigenfunctions that most closely agree with the equatorial asymmetries of the observed latitudinal structures of h, v and u variability along 140° W (see the heavy and thin solid lines in the second column of Fig. 24 below). For subsequent discussion and for the solutions of the 1.5 layer Eqs. (4)–(6) along the other longitudes considered in Sections 6.4 and 6.5, we will therefore restrict attention to the eigenfunctions obtained from zonal velocity profiles averaged over the upper 250 m.

It is noteworthy that the value of the reduced gravity $g' = g \Delta\rho / \rho$ that is obtained from the mean upper-layer thickness of $H_1 = 250$ m, an upper layer water density ρ, a density difference $\Delta\rho$ between the two layers, and the baroclinic gravity wave phase speed of $c_1 = 2.7$ m s^{-1} appropriate for this region corresponds to a two-layer density difference of $\Delta\rho = 3$ kg m^{-3}. This is a realistic value for this region. Expressed in terms of the shallow-water equations for a single homogeneous layer with a mean effective depth H_e, the

combination of c_1 and H_1 used here to define g' is equivalent to $H_e = 0.75$ m, which is very nearly the same as the value of 0.70 m considered by Philander (1979).

The theoretical and observed estimates of the latitudinal structure of equatorially trapped Rossby waves at 140° W are in good agreement (see the second column of Fig. 24 below). In particular, the observed asymmetries of the amplitudes of h, v and u variability north and south of the equator are well described by the simple 1.5-layer model linearized about the 250 m averaged zonal velocity profile $U(y)$. The agreement between the theoretical eigenfunctions and the observed variability is especially good between 10° N and 5° S. At higher southern latitudes, however, the model does not account for the detailed structures of the observed variability of h or u. The secondary extrema of the theoretical eigenfunctions for h and u are located at about 5° S and the eigenfunctions decrease to near zero at 10° S. In contrast, the secondary maximum in the observed variability of h is centered near 6° S and is significantly broader, extending to about 13° S. Unlike the eigenfunction for u, there is no secondary negative extremum south of the equator in the observed latitudinal structure of u.

In an effort to understand the reason for the discrepancies between the theory and the observations south of 5° S, we conducted a number of simulations in search of a feature in the equatorial current system that could broaden the secondary maximum of the h eigenfunction to higher southern tropical latitudes and eliminate the southern secondary extremum of the u eigenfunction. Increasing or decreasing the velocity of any of the individual components of the equatorial current system failed to bring the theory into agreement with the observations.

There are numerous possible explanations for the mismatch between the theory and the observations south of 5° S. The discrepancy is probably the result of, at least in part, shortcomings of the model, the most likely candidate being the simplicity of the representation of the baroclinic structure by the 1.5-layer model considered here. The thermocline is much more diffuse south of 5° S than across the rest of the equatorial waveguide (see, for example, Wyrtki & Kilonsky, 1984). The 1.5-layer model is less representative of the weak thermocline at these southern tropical latitudes. Sampling errors in the ADCP/CTD data within the relatively sparsely sampled latitude range 5–8° S and the lack of any velocity observations south of 8° S (see the second panel in the bottom row of Fig. 22 below) cannot be discounted as another candidate explanation. Likewise, unknown artifacts of the filtering applied to the TOPEX/POSEIDON data may be a concern south of the equator where the amplitudes of variability are smaller (Figs 2 and 13), and are therefore more sensitive to measurement and sampling errors.

Despite the inability of the 1.5-layer model to account for the precise latitudinal structures of h, v and u south of 5° S, the observed latitudinal structures are remarkably well described overall for each of these state variables. The simple 1.5-layer model thus captures the essence of observed h, v and u signatures of equatorially trapped Rossby waves in the presence of the meridionally sheared equatorial current system near the longitude of 140° W. The structures of the eigenfunctions at other longitudes are investigated in Sections 6.4 and 6.5.

The dependency of the latitudinal structure of the h eigenfunction on wavelength (and hence on period through the dispersion relation) was determined by successively solving Eqs. (4)–(6) as a function of zonal wavenumber k. The equatorial asymmetry of the amplitude is only weakly sensitive to wavenumber (upper panel of Fig. 20). Over wavelengths of $1–3 \times 10^4$ km (corresponding to the approximate $0.3–1.0 \times 10^{-4}$ cycles km^{-1} wavenumber range of the 150–500-day band-pass filtering applied to the TOPEX/POSEIDON data, see the dispersion relation in Fig. 21 below), there is essentially no change in the meridional structure of the eigenfunction for h. At higher negative zonal wavenumbers, the secondary maximum south of the equator increases somewhat with increasing negative wavenumber, but remains highly asymmetric even at the shortest wavelength of about 1400 km shown in Fig. 20. The deepening of the minimum centered on the equator is not an effect of wave-mean flow interaction since this is also a feature of the classical Hermite function solution for the zero mean flow case (lower panel of Fig. 20). The v and u eigenfunctions
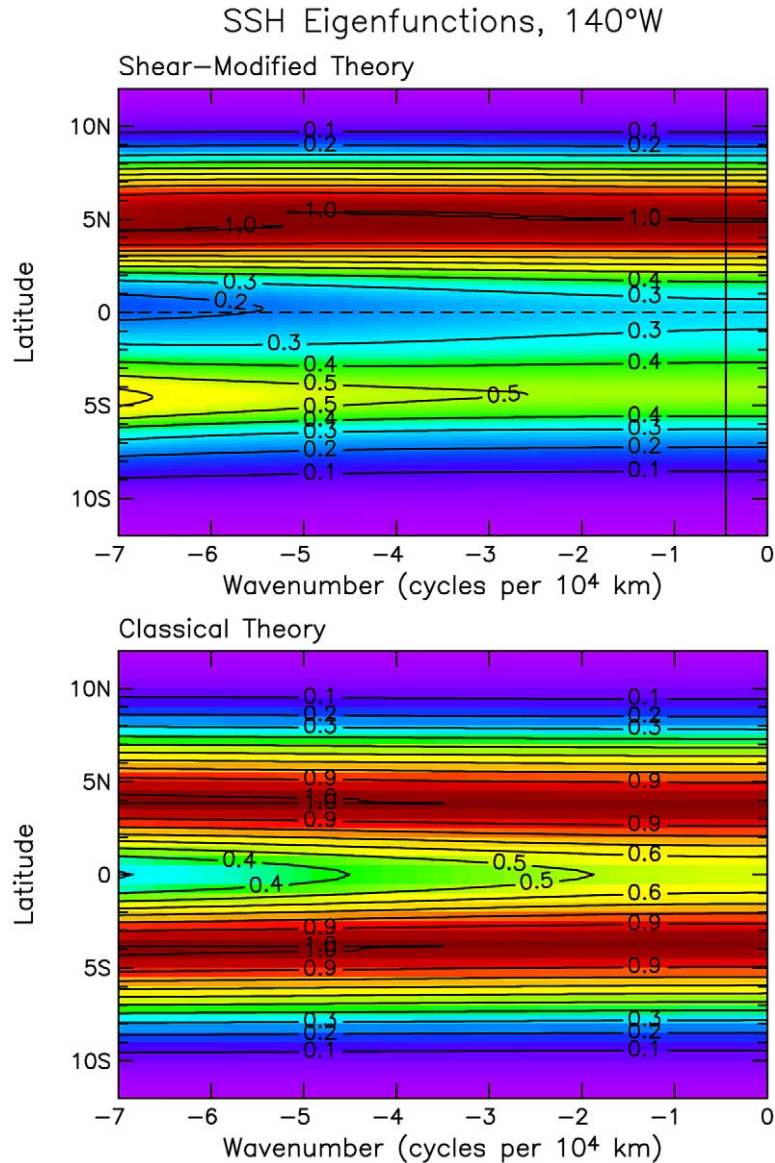
Fig. 20. The wavenumber dependence of the latitudinal structure of the *h* eigenfunction from the 1.5 layer β-plane Eqs. (4)–(6) linearized about the mean zonal velocity averaged over the upper 250 m along 140° W (upper panel) and from the classical theory (lower panel). The vertical line in the upper panel is the wavenumber at which the latitudinal structures of the eigenfunctions are shown by the heavy solid lines in Fig. 19. This wavenumber corresponds to annual variability in the dispersion relation shown in Fig. 21.

(not shown here) are similarly insensitive to wavenumber within the range of wavelengths associated with the quasi-annual variability that is of interest here.

Recall from Sections 2 and 5 that the phase speeds of the observed westward propagating signals are considerably slower than the ~0.9 m s^{-1} phase speed predicted from the classical theory. The dispersion relation from the 1.5-layer model linearized about the 250-m averaged $U(y)$ profile along 140° W was
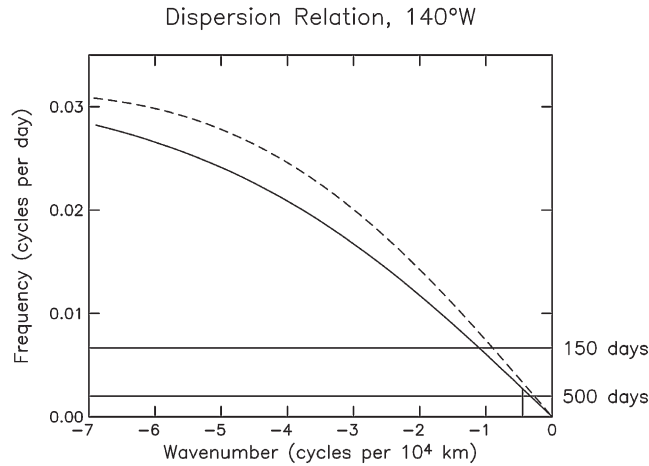
Fig. 21.   The dispersion relations for eigensolutions computed from the 1.5 layer β-plane Eqs. (4)–(6) linearized about the mean zonal velocities averaged over the upper 250 m along 140° W (solid line) and from the classical theory (dashed line). The horizontal lines indicate the half-power points of the 150–500-day band-pass filter applied to the TOPEX/POSEIDON data as described in Section 3.1. The short vertical line in the lower right corner indicates the wavenumber that corresponds to annual variability in the shear-modified dispersion relation.

obtained from the frequency eigenvalues ω for closely spaced values of the zonal wavenumber k and compared with that of the classical theory (Fig. 21). As previously found by Philander (1979), Chang and Philander (1989) and Zheng et al. (1994), the phase speeds of the first meridional eigensolution are reduced by the presence of the background mean equatorial current system. For the annual period, the phase speed of the shear-modified first-meridional mode Rossby waves decreases by about 20% relative to the phase speed obtained from the classical theory (0.71 m s^{-1} compared with 0.87 m s^{-1}).

Although an improvement over the classical theory, the phase speed of 0.71 m s^{-1} in the shear-modified theory is still higher than the phase speeds of the observed variability, which were estimated by a variety of different methods in Section 5 to range from about 0.5-0.6 m s^{-1}.

6.4. Eigensolutions along 110° W, 125° W and 155° W

The methodology summarized in Section 6.3 for obtaining the eigenfunctions along 140° W was applied to solve the 1.5 layer Eqs. (4)–(6) linearized about the 250 m vertically averaged zonal velocity profiles $U(y)$ along 110° W, 125° W and 155° W. All of the components of the equatorial current system are readily identifiable in the mean zonal velocity sections estimated from the ADCP/CTD data along these longitudes (top row of Fig. 22). In each section, the EUC is centered just south of the equator with a subsurface maximum that rises toward the east from a depth of about 120 m at 155° W to about 60 m at 110° W. The two branches of the SEC straddle the EUC. The NECC is strongest in the central Pacific at 140° W. At 110° W, the NECC becomes weak and difficult to distinguish from the northern subsurface countercurrent (the northern Tsuchiya jet, see Rowe, Firing & Johnson, 2000).

The 250-m vertically averaged representations of the EUC, SECS and SECN are very similar along all four eastern longitudes (middle row of Fig. 22). The only significant differences are in the 250-m averaged representations of the NECC, which is somewhat weaker along the two easternmost longitudes. However, these differences in the NECC have very little effect on the shear contributions to the potential vorticity gradient Q_y within the equatorial waveguide that are important to the dynamics of equatorially trapped Rossby waves (upper panel of Fig. 23).
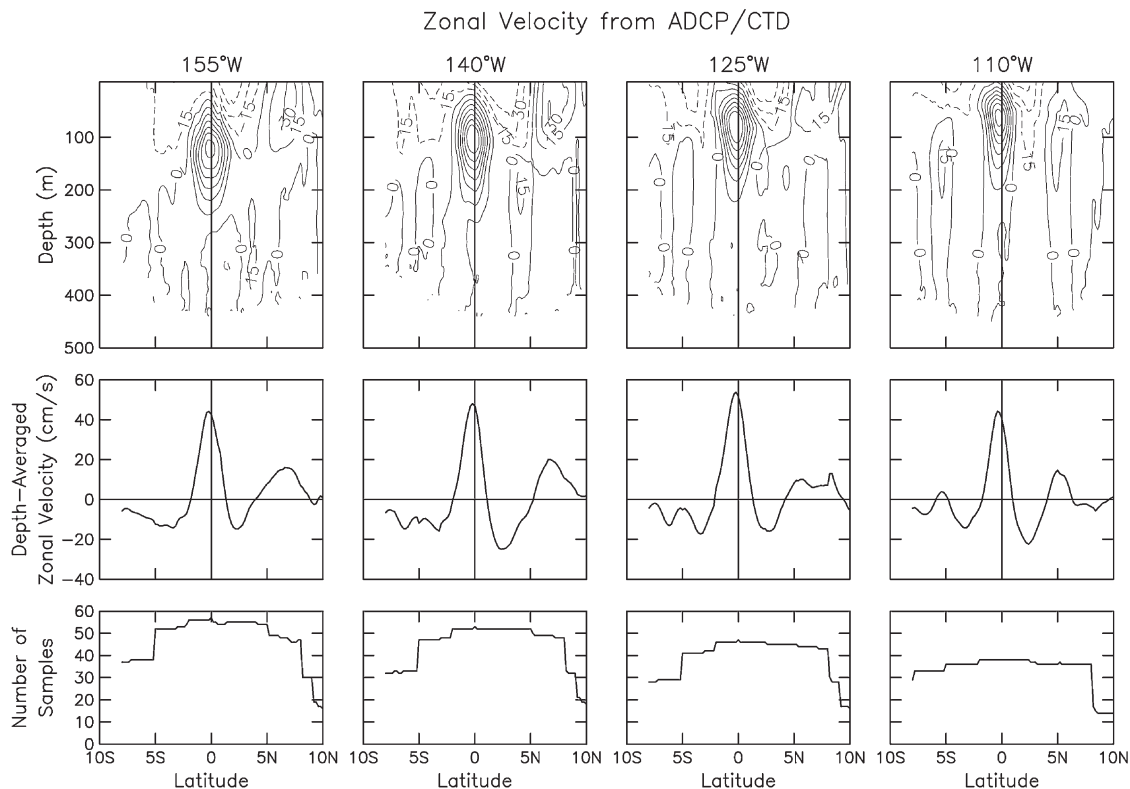
Zonal Velocity from ADCP/CTD

Fig. 22. Vertical sections of the mean zonal velocity estimated from ADCP/CTD data along the four eastern longitudes considered in this study (top row). The contour interval is 15 cm s^{-1}. The zonal velocity profiles along each longitude obtained by averaging vertically over the upper 250 m are shown in the middle row. The number of ADCP/CTD samples at a depth of 150 m summed over the central longitude and the nearest neighboring longitudes to the east and west are shown as functions of latitude in the bottom row.

The eigenfunctions for h, v and u are very similar along each of the four eastern longitudes (Fig. 24). The relatively minor differences in the currents and the associated meridional shears along the four sections thus have little effect on the meridional structures of the eigenfunctions. The h eigenfunction along 140° W has a northern maximum that is slightly broader in latitudinal extent and centered at a slightly higher latitude than the northern maxima along the other longitudes. In addition, the secondary maximum south of the equator is slightly larger in amplitude along 140° W. Likewise, there are minor differences between the detailed structures of the v and u eigenfunctions along each longitude. These differences are not significant in view of the sensitivity of the latitudinal structures of the eigenfunctions to relatively small changes in the definition of the mean zonal velocity profile, $U(y)$ (Fig. 19).

The EOF representations of the observed latitudinal structures of the h, v and u signatures of westward propagating signals along the four eastern longitudes (the upper four panels in Figs 12, 14 and 15) are overlaid as heavy solid lines in Fig. 24. The results for 110° W, 125° W and 155° W are very similar to those obtained in Section 6.3 for 140° W. Along all four of these longitudes, the cross-equatorial asymmetries of the amplitudes of the observed h, v and u variability are well represented by the theoretical eigenfunctions. The observed secondary maxima south of the equator in the h EOFs peak at somewhat lower latitudes along 110° W and 125° W compared with the other two longitudes. As in the case of the 140° W results, the southern maxima of the h EOFs along all four eastern longitudes are broader in the observations than
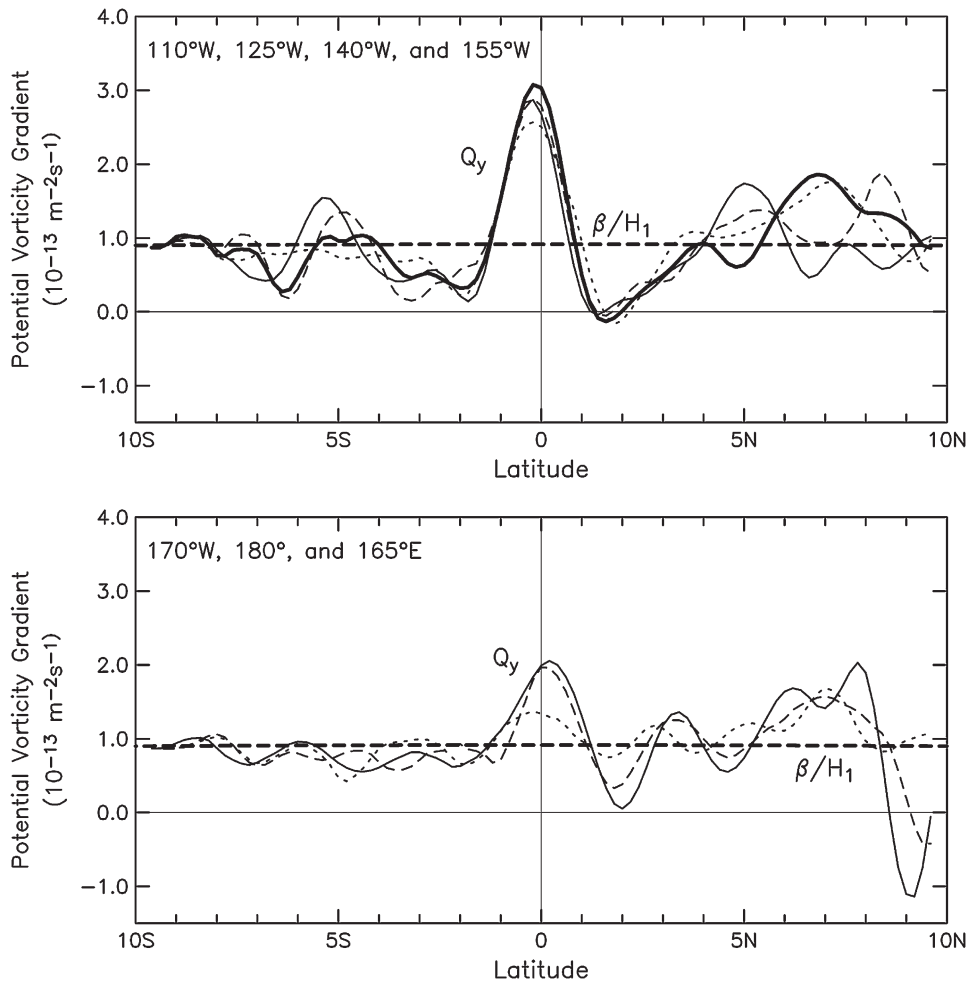
Fig. 23. The meridional gradient of potential vorticity, Q_y, computed from $U(y)$ and $H(y)$ in the 1.5-layer model along the four eastern longitudes (upper panel) and the three western longitudes (lower panel) considered in this study. The heavy solid, thin solid, dashed and dotted lines in the upper panel represent the Q_y profiles along 140° W, 110° W, 125° W and 155° W, respectively. The thin solid, dashed and dotted lines in the lower panel represent the Q_y profiles along 170° W, 180° and 165° E, respectively. The heavy dashed line in both panels is the potential vorticity gradient β/H_1 in the 1.5-layer model with $U(y) = 0$ and a constant upper-layer thickness of $H_1 = 250$ m.

in the model. The northern maximum is also broader in the observations than in the model at the two eastern longitudes and, to a lesser extent, at 155° W. Also noteworthy is the fact that the *u* EOFs are negligibly small south of 5° S at all four eastern longitudes, whereas the theoretical *u* eigenfunctions all exhibit secondary negative extrema at about 6° S.

6.5. Eigensolutions along 170° W, 180° and 165° E

The meridional sections of mean zonal velocity estimated from the ADCP/CTD data along 170° W, 180° and 165° E (top panels of Fig. 25) differ significantly from the eastern sections. The SECS at these three longitudes is similar to the SECS at the four eastern longitudes. The current speeds of the SECN,
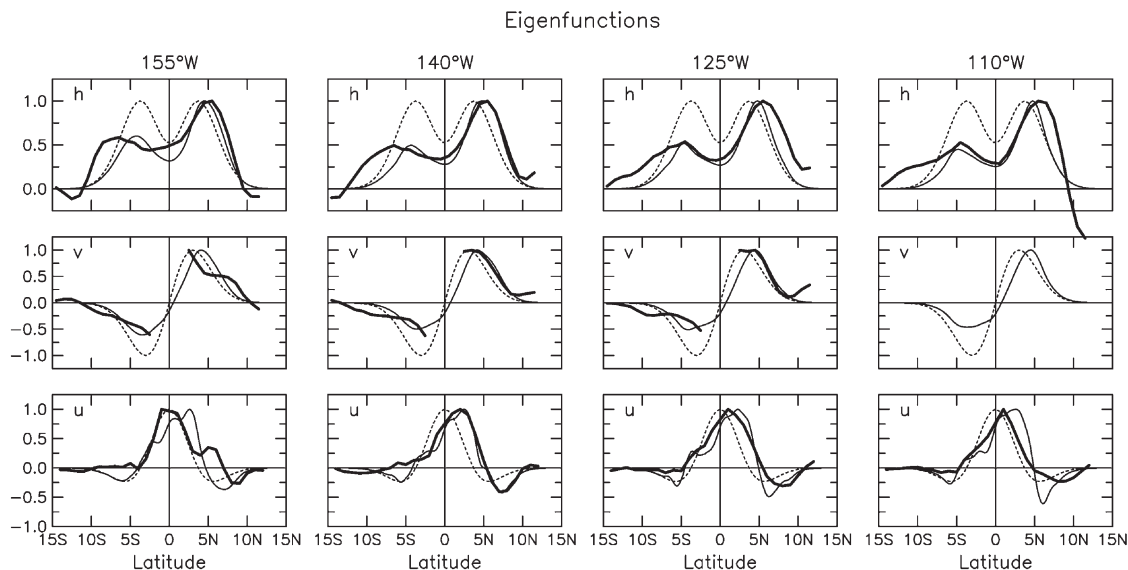
Eigenfunctions

Fig. 24. The eigenfunctions for h, v and u computed from the 1.5 layer β-plane Eqs. (4)–(6) linearized about the mean zonal velocities averaged over the upper 250 m along the four eastern longitudes considered in this study (thin solid lines). The dotted lines are the Hermite function solutions of the classical theory. The heavy solid lines are the observed latitudinal structures of h, v and u from the EOFs shown in the left panels of Figs 12, 14 and 15, respectively. The v EOF along 110° W is omitted because it is not representative of equatorially trapped Rossby waves (see the discussion of Fig. 15).

however, decrease progressively toward the west. Furthermore, the EUC weakens and deepens toward the west with a maximum located slightly north of the equator along all three longitudes. Moreover, at all three western longitudes, the subsurface countercurrents on both sides of the equator (the Tsuchiya jets) are difficult to distinguish from the EUC (see Rowe et al., 2000). This results in a deep broadening of eastward velocity about the equator that is somewhat more pronounced on the north side of the equator.

The different current structures along the three western longitudes have significant effects on the $U(y)$ profiles averaged over the upper 250 m (compare the middle panels of Fig. 25 with the middle panels of Fig. 22). The representation of the effects of the EUC in the 1.5-layer model is centered just north of the equator along all three western longitudes and progressively weakens toward the west. Most significantly, the SECN in the 250-m average $U(y)$ profiles is nonexistent along all three western longitudes. These differences in the $U(y)$ profiles have very large effects on the shear contributions to the potential vorticity gradient Q_y within a few degrees of the equator along each of the three western longitudes (lower panel of Fig. 23).

In view of their distinctly different Q_y profiles, it is not surprising that the eigenfunctions of the 1.5-layer model along the three western longitudes (thin solid lines in Fig. 26) have different latitudinal structures than those for the four eastern longitudes (thin solid lines in Fig. 24). At all three western longitudes, the model eigenfunctions for each of the three state variables differ very little from the Hermite function solutions of the classical theory (dotted lines in Fig. 26). The strongly asymmetric structures of the model eigenfunctions at the four eastern longitudes (Fig. 24) are evidently dependent on the existence of the SECN that is absent at the three western longitudes, and perhaps on the speed and precise latitude of the maximum of the EUC.

There are subtle differences among the eigenfunctions for the three western longitudes that may be noteworthy (Fig. 26). Along 170° W, there are still small asymmetries in the h and v eigenfunctions with slightly larger amplitude in the north than in the south. Along 180° and 165° E, the v eigenfunctions are
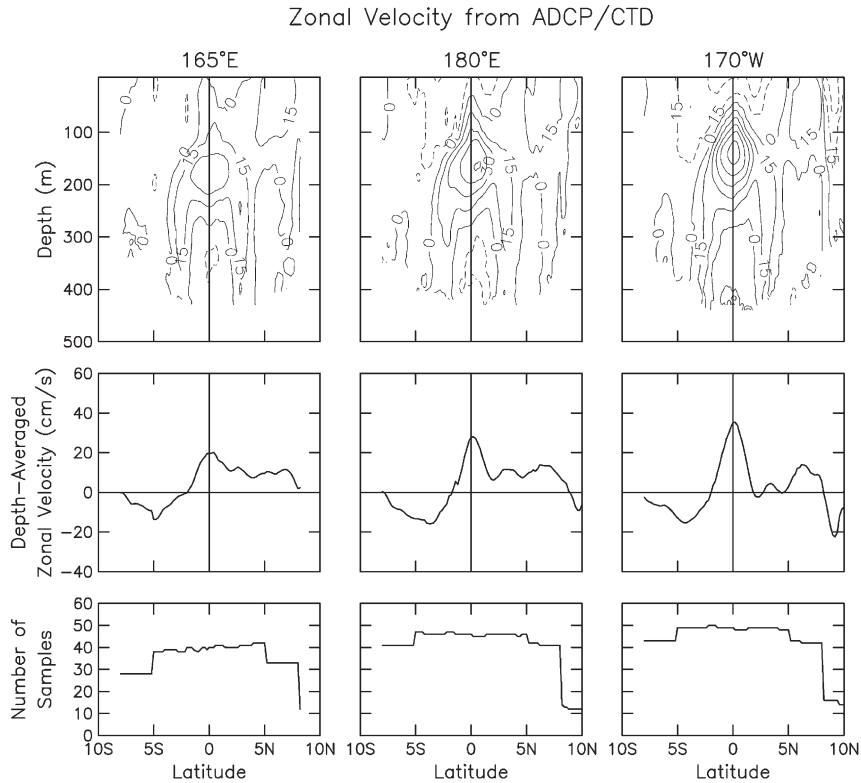
Fig. 25.   The same as Fig. 22, except for the three western longitudes considered in this study.

barely distinguishable from the Hermite function solutions, while the *h* eigenfunctions are slightly asymmetric with smaller amplitude in the north than in the south. From simulations, we have determined that this subtle hemispheric change in the asymmetry is attributable to a combination of the disappearance of the SECN and the shift of the center of the EUC to a latitude slightly north of the equator at the two westernmost longitudes. It is noteworthy that the extrema of the *h* and *v* eigenfunctions along 180° and 165° E shift equatorward to the same latitudes as the extrema of the Hermite function solutions. Philander (1979) showed that the latitudes of the extrema depend on the existence and intensity of the EUC. The equatorward shift of the extrema at the two westernmost longitudes considered here is thus apparently the result of the weakening of the EUC toward the west.

  The EOF representations of the observed latitudinal structures of *h*, *v* and *u* variability along the three western longitudes (the lower three panels of Figs 12, 14 and 15) are overlaid as heavy solid lines in Fig. 26. The observed structures along 170° W and 180° are distinctly different from the model eigenfunctions but are very similar to the latitudinal structures of observed variability along the four eastern longitudes considered in Sections 6.3 and 6.4 (compare with the heavy solid lines in Fig. 24). In particular, the observed variabilities of *h* and *v* exhibit the same asymmetry of the amplitude north and south of the equator and the observed variability of *u* has a central maximum centered at about 1° N with very small amplitude south of 5° S.

  As discussed in Section 4, the latitudinal structure of the observed variability is significantly different at the westernmost longitude of 165° E than at any of the other six longitudes considered here. Specifically, the observed variabilities of *h* and *u* are more symmetric about the equator. The observed structures along
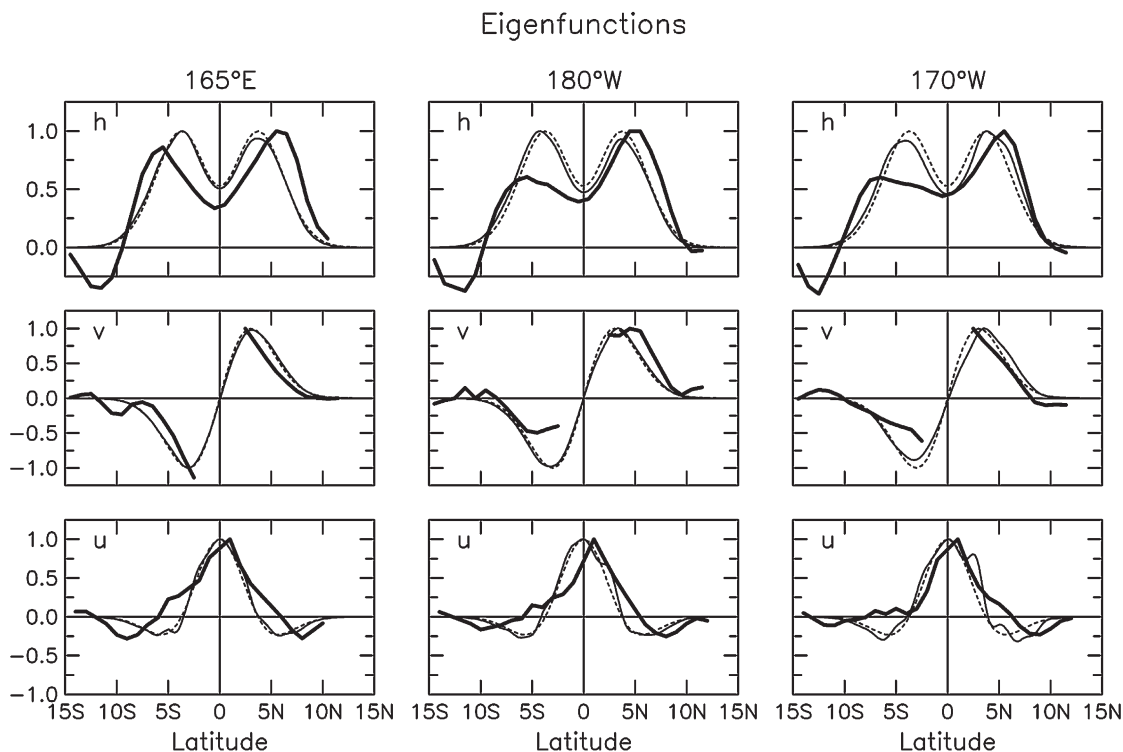
Eigenfunctions

Fig. 26.   The same as Fig. 24, except for the three western longitudes considered in this study.

165° E are thus more consistent with the essentially symmetric structures of the shear-modified theoretical eigenfunctions for *h* and *u* along the three western longitudes. Likewise, although somewhat noisy south of the equator, the observed latitudinal structure of *v* along 165° E is nearly antisymmetric like the eigenfunction for *v*. However, while the latitudes of the extrema of the observed *h* and *u* variability along 165° E are similar to those of the observed *h* and *u* variability across the full width of the tropical Pacific, the off-equatorial extrema are about 2° higher on both sides of the equator in the observations than in the eigenfunctions along 165°E. In addition, the central maximum in the observed *u* variability is broader than that of the *u* eigenfunction.

The local solutions of the eigenvalue problem at each longitude thus do not correspond precisely to the observed variability. Of course, long equatorial Rossby waves propagating westward through a background mean current field that varies longitudinally are not likely to have latitudinal structure that reflects only the effects of the local current field. Geographical variations of the mean zonal velocity field result in locally predicted shear-modified theoretical eigenfunctions that change rather abruptly from highly asymmetric cross-equatorial structures in the eastern and central basin to essentially the structures of the classical solutions for *h*, *v* and *u* to the west of 155° W. The observed transition occurs farther west at the westernmost longitude of 165° E considered here, albeit with greater latitudinal spreading than predicted by the 1.5-layer model.

7. Summary and discussion

Past analyses of the annual variability of isotherm depths, dynamic height and sea surface height (SSH) within the equatorial waveguide between about 8° S and 8° N in the Pacific Ocean have consistently

observed latitudinally asymmetric variability with larger amplitude north of the equator. This is in contradiction to the classical theory for equatorially trapped Rossby waves from which the odd- and even-numbered meridional eigenfunctions for these variables have symmetric and antisymmetric latitudinal structures, respectively (Fig. 1). The observed latitudinal structures thus differ from those of any of the individual meridional modes in the classical theory. In particular, the classical solution for the first meridional mode that is generally considered to dominate the variability is symmetric about the equator in SSH, dynamic height and thermocline depth, with maxima at about 4° N and 4° S.

The latitudinal asymmetry of SSH variability in the tropical Pacific has been confirmed in this study from an analysis of quasi-annual variability in 8.5 years of TOPEX/POSEIDON altimeter data. The TOPEX/POSEIDON data were filtered to remove energetic signals associated with tropical instability waves, equatorial Kelvin waves, the ENSO phenomenon, midlatitude Rossby waves, and steric heating and cooling with large zonal scale. This filtering isolates quasi-annual SSH variability that is highly correlated latitudinally across the equatorial waveguide and longitudinally across most of the Pacific with larger amplitude north of the equator and a westward phase speed estimated here to be in the range 0.5–0.6 m s^{-1}. These phase speeds are 35–45% slower than the ~0.9 m s^{-1} phase speed predicted by the classical theory.

The cross-equatorial structures of the *h*, *v* and *u* signatures of the observed equatorially trapped Rossby waves along the seven longitudes considered in this study were summarized by the EOF analyses in Sections 4.2, 4.4 and 4.5. These EOFs are superimposed separately as the colored lines in Fig. 27 for the four eastern longitudes (right panels) and the three western longitudes (left panels). The variability along each longitude is equatorially asymmetric in all three variables. The observed latitudinal structures are remarkably similar at all but the westernmost longitude of 165° E, which is shown as the green lines in the left panels of Fig. 27. Across an 8000 km span of the tropical Pacific, the amplitudes of *h* and *v* are about a factor of two larger north of the equator than south of the equator. (The equatorial gap in the *v* EOFs is because of the inability to obtain useful estimates of the meridional geostrophic velocity closer than 2° from the equator.) Likewise, the *u* EOFs are asymmetric with maxima centered about 1° north of the equator, significant negative extrema centered near 7.5° N and little or no amplitude south of the equator. The EOFs along 165° E are more nearly symmetric in *h* and *u* and antisymmetric in *v*.

As summarized in Section 2, past studies have variously attributed the asymmetric structure of observed equatorially trapped Rossby waves to sampling errors in the data, a superposition of multiple meridional modes, equatorially asymmetric forcing by the wind stress curl, and forcing by the cross-equatorial southerly winds in the eastern tropical Pacific. We believe that none of these explanations satisfactorily account for the observed latitudinal structure for the following reasons.

Concerns about sampling errors can be dismissed with the extensive spatial coverage and 8.5-year duration of the TOPEX/POSEIDON dataset analyzed here. It also seems unlikely that mode superposition can account for the asymmetric latitudinal structures since the westward phase speeds of low-frequency waves decrease as $(2m + 1)^{-1}$ for increasing meridional mode *m*. A local superposition of the symmetric first mode and the antisymmetric second mode could occur with amplitudes that add constructively north of the equator and destructively south of the equator in such a way as to produce the observed asymmetric structures. Since the westward phase speeds of these two modes differ by about 40%, a latitudinal structure that is initially asymmetric in the eastern Pacific could not be maintained across the 8000-km distance from 110° W to the Dateline over which the asymmetric structure exists in the observations (see the red lines in Fig. 27).

To our knowledge, direct wind generation of asymmetric equatorial Rossby waves also has not been conclusively demonstrated. Wind stress curl is indeed much stronger north of the equator (Fig. 6). Most models of asymmetrically forced Rossby waves also have an asymmetric background mean flow. It is therefore difficult to distinguish the effects of direct forcing by asymmetric winds from shear-induced wave–mean flow interaction. The only study that we are aware of that has isolated the effects of wind forcing is the linear, zero mean flow model considered by Kessler and McCreary (1993). When that model
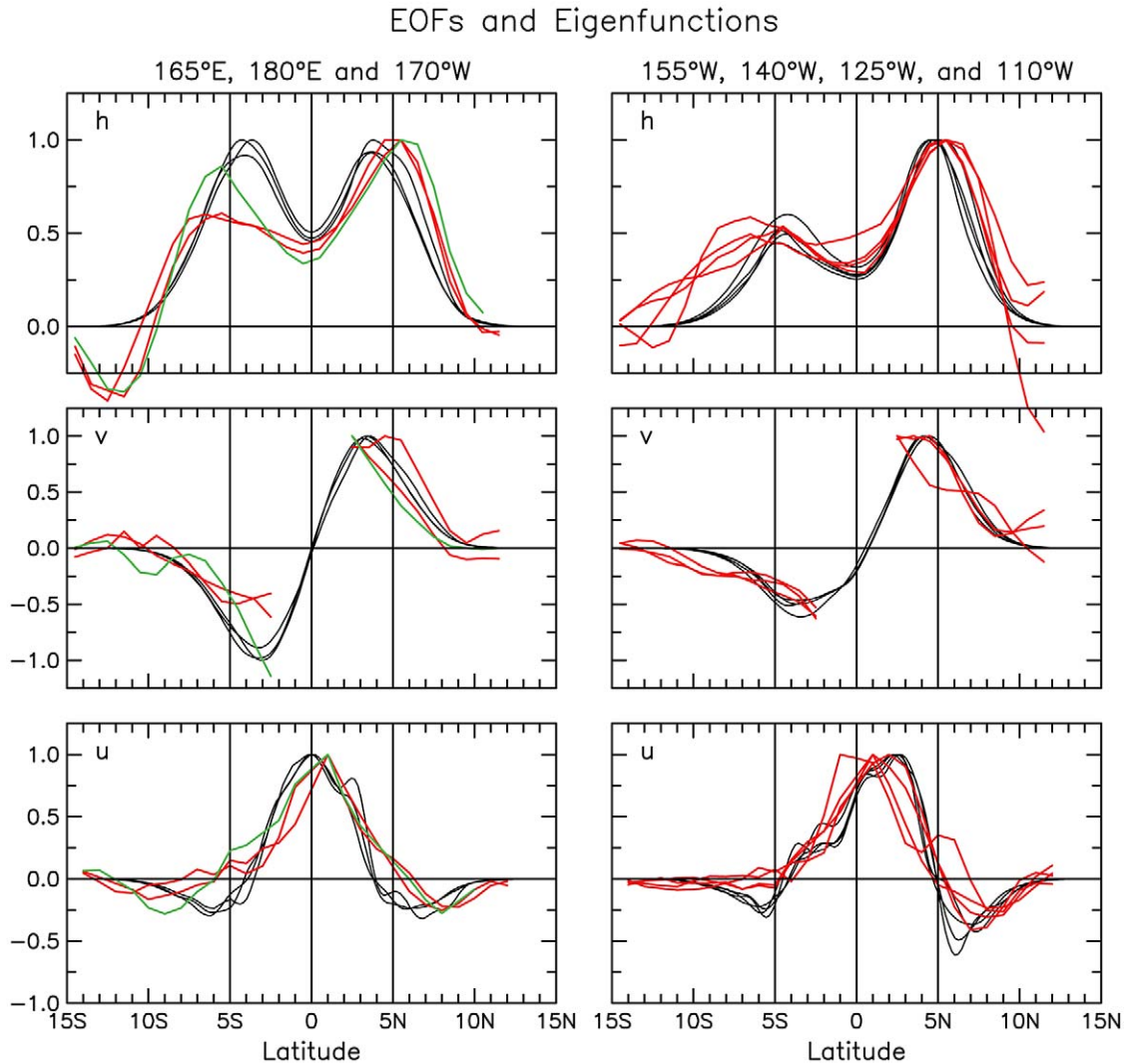
Fig. 27. Superpositions of the observed latitudinal structures characterized by the EOFs (colored lines), and the theoretical eigen-functions (thin solid black lines) for *h*, *v* and *u* along the seven longitudes considered in this study. The results for the four eastern longitudes and the three western longitudes are shown in the right and left panels, respectively. The two red lines in the left panels are the EOFs along 170° W and 180° and the green line is the EOF along the westernmost longitude of 165° E. Note the similarities of the latitudinal structures along 170° W and 180° to those of the EOFs along the four eastern longitudes.

was forced with a realistic asymmetric annual cycle of the wind field, the thermocline signature of the annual Rossby wave response was latitudinally symmetric about the equator. Based on this result, it appears that asymmetry of the wind forcing is not sufficient to generate asymmetric equatorial Rossby waves. In contrast, equatorial Rossby waves are asymmetric in models with asymmetric mean currents (e.g., McPhaden et al., 1988; Wang et al., 2000).

In this study, we believe that we have identified the dominant explanation for the observed equatorially asymmetric latitudinal structure of low-frequency equatorially trapped Rossby waves. The classical theory neglects the effects of background mean currents on the free modes of the system. We used the 1.5-layer

model first considered by Philander (1979), which is the simplest model for baroclinic equatorially trapped waves in the presence of a baroclinic background mean flow. Although clearly an oversimplified representation of the baroclinic structure of the equatorial Pacific, the results obtained from this 1.5-layer model provide useful insight into the importance of the background mean currents to equatorial Rossby waves. The currents exert a non-negligible effect on the potential vorticity gradient in the central and eastern Pacific (Fig. 23). The meridional shears in these currents alter the latitudinal structure and dispersion characteristics of Rossby waves.

For this analysis of the effects of asymmetric background mean currents on equatorial Rossby waves, we have considered only the unforced equations on an equatorial β plane. Though not explicitly considered, wind forcing is obviously essential to the establishment of the asymmetric mean equatorial current system and to the generation of quasi-annual Rossby waves. A more complete analysis should explicitly include the effects of wind forcing through the forced β-plane equations. For the analyses in Section 6, the unforced equations for the upper layer were linearized about the background mean zonal velocities estimated from 16 years of ADCP/CTD data along seven longitudes between 110° W and 165° E. The free-wave eigensolutions obtained locally in Sections 6.3–6.5 at each of the seven longitudes are superimposed as the thin black lines in Fig. 27. When the eigenfunctions are segregated geographically in this manner (the four eastern longitudes vs. the three western longitudes), it is apparent that the characteristics of the eigenfunctions divide conveniently into these two groups.

Across the eastern half of the tropical Pacific, the eigenfunctions are significantly different from the Hermite function solutions of the first meridional mode of the classical theory (compare the black lines in the right panels of Fig. 27 with the first meridional mode solutions in Fig. 1). In particular, the shear-modified eigenfunctions are equatorially asymmetric with latitudinal structures that are very similar to the EOFs of the observed variability of h, v and u. These asymmetries are dependent on the existence of the northern branch of the South Equatorial Current. From the sensitivity studies conducted in Section 6.3, the differences between these model eigenfunctions and the observed latitudinal structures can largely be accounted for by minor inaccuracies in the mean zonal flows estimated from the ADCP/CTD data; relatively small changes in the latitudes and intensities of the Equatorial Undercurrent and the northern branch of the South Equatorial Current can alter the latitudinal structures of the eigenfunctions enough to account for most of the discrepancies between the model and the observations.

The region south of 5° S is an exception to the generally good agreement between the observations and the theory. At these southern tropical latitudes, the observed variabilities of h and v are consistently broader in latitudinal extent than the h and v eigenfunctions and the observed variability of u is negligibly small compared with the u eigenfunction. We have been unable to reproduce these observed characteristics in any model sensitivity studies. This is apparently a shortcoming of the simple model considered here. The most likely limitation of the model is the inadequacy of a 1.5 layer representation of the vertically diffuse thermocline south of 5° S. Incomplete knowledge of the mean currents in the sparsely sampled region south of 5° S cannot be entirely discounted as a partial explanation for the southern hemisphere discrepancy between the model and observations. Residual contamination of the filtered TOPEX/POSEIDON data by processes other than equatorially trapped Rossby waves may also be a factor.

The weakening of the equatorial current system in the western tropical Pacific (specifically, the weakening of the Equatorial Undercurrent and especially the disappearance of the northern branch of the South Equatorial Current) results in eigensolutions with latitudinal structures that differ very little from the Hermite function solutions of the first meridional mode of the classical theory (compare the black lines in the left panels of Fig. 27 with the first meridional mode solutions in Fig. 1). The eigenfunctions for h and u are essentially symmetric and the eigenfunctions for v are essentially antisymmetric. The symmetries of the observed latitudinal structures of h, v and u at the westernmost longitude of 165° E (the green lines in Fig. 27) become nearly the same as those of the eigenfunctions, although with greater latitudinal broadening of h and u. At 180° and 170° W, however, the observed latitudinal structures are very similar to the

observed structures of *h*, *v* and *u* across the eastern half of the basin (compare the red lines in the left and right panels of Fig. 27), albeit with somewhat less latitudinal broadening of the southern maxima. The observations thus suggest that there is a tendency for westward propagating equatorially trapped Rossby waves to evolve towards the solutions of the classical theory in the far western tropical Pacific, but the transition occurs more gradually than in the local eigensolutions.

Given the basin-wide wavelength of quasi-annual equatorial Rossby waves, the level of agreement found here between the local model solutions and the observations is perhaps surprising. Local solutions of the eigenvalue problem ignore the effects of the eastern and western boundaries, wind and buoyancy forcing, and implicitly assume that the background mean currents do not change as the wave propagates to the west. While the background mean currents weaken gradually toward the west, the associated meridional gradient of potential vorticity changes rather abruptly between 155° W and 170° W in the 250-m average $U(y)$ profiles considered here (Fig. 23). The theoretical eigensolutions are thus fundamentally different at the three western longitudes than at the four eastern longitudes. The lack of agreement between the observations and the model at 170° W and 180° is therefore at least partly attributable to the inability of equatorially trapped Rossby waves to adjust instantaneously to geographical variations in the ambient potential vorticity associated with the zonally varying background mean equatorial current system.

Although the effects of zonally varying currents on equatorially trapped Rossby waves have not been investigated, the related question of the effects of zonally varying stratification has been studied by Busalacchi and Cane (1988). They found that zonal variations over distances short compared with the wavelength of the Rossby wave have only a small effect on the character of the waves. The more nearly symmetric latitudinal structure and reduced latitudinal broadening of the southern maximum of the observed SSH variability and the more nearly antisymmetric structure of *v* (though somewhat noisy south of the equator) at the westernmost longitude of 165° E suggest that the westward propagating equatorially trapped Rossby waves evolve toward the latitudinally symmetric structure predicted locally by the model considered here. Likewise, the variability of *u* evolves to more nearly symmetric structure at 165° E.

The cross-equatorial asymmetries of SSH, isotherm depths, dynamic height and geostrophic velocity components across most of the tropical Pacific can thus be largely accounted for by the simple 1.5-layer model considered here. A more sophisticated model of the baroclinic structure will surely result in quantitatively different latitudinal structures of *h*, *v* and *u*, but it is unlikely that the eigenfunctions will lose the equatorially asymmetric structures obtained from the 1.5-layer model.

It is surprising that so much of the observed variability (typically 50–70%, see Figs 12, 14 and 15) can apparently be interpreted as a single free mode (the first vertical, first meridional free mode modified by the meridionally sheared mean currents). The remaining 30–50% of the variance along each longitude is evidently at least partly attributable to other meridional or vertical modes of the system. In addition, the latitudinal variation of phase speed within the equatorial waveguide implied by the latitudinally varying CEOF phase in the third panel of Fig. 9 is an indication that the single-mode description is incomplete at latitudes higher than about 7° within the equatorial waveguide (see the discussion in Section 4.2). Within about 5° of the equator, however, the single shear-modified first vertical, first meridional mode equatorial Rossby wave appears to describe much of the variability.

A somewhat troubling discrepancy between the observations and the model is the slower westward phase speed observed along 5.5° S than along 5.5° N, where the phase speeds are approximately 0.5 m s^{-1} and 0.6 m s^{-1}, respectively. Although the uncertainties of these phase speed estimates overlap, we suspect that the difference is significant. Some of this hemispheric difference in phase speed may be attributable to the difficulty in estimating a single representative phase speed for each latitude when the phase speed varies zonally along the path of propagation (for reasons that cannot be determined from the simple model considered here).

While the 0.71 m s^{-1} phase speed predicted by the 1.5-layer model is slower than that of the classical theory, observed phase speeds along both latitudes are slower still. There are many possible explanations

for the overestimate of the model phase speed. These include lack of consideration of the effects of wind forcing on the westward propagation speeds, the effects of nonlinearities, the simplistic treatment of baroclinic effects, and neglect of the effects of the eastern and western boundaries on the free modes of the system. In the case of the latter, the phase speed of the forced basin modes of the system are likely to be constrained by the periodicity of the wind forcing and the basin width, rather than by the dispersion relation of the local eigenvalue problem. However, the latitudinal structures of the forced basin modes are likely to be similar to the shear-modified local eigenfunctions presented here.

A more complete theoretical analysis should also take into consideration the effects of meridionally sheared mean zonal currents on the group velocity of quasi-annual Rossby waves. Chang and Philander (1989) and Proehl (1990) have shown that background mean currents can significantly alter the meridional group velocity, resulting in complicated ray paths. As a result, it is possible for extra-tropical forcing to influence variability within the equatorial waveguide. In addition to the resonance and off-resonance of wind stress curl forcing suggested in Section 4.1, this energy of extra-tropical origin may account for the geographical variability of the standard deviations of h, u and v within the equatorial waveguide (Figs 2 and 13), e.g., the smaller amplitudes of h and u variability between about 140° W and the Dateline.

Although the details of the mechanism for wind generation and reflected equatorial Kelvin wave generation of equatorial Rossby waves have not been addressed in this analysis, both of these processes are likely to play a role in the generation of the observed equatorial Rossby waves. The strong resemblance between the observed latitudinal structures and the theoretical free-wave solutions considered here suggests that the asymmetric wind stress curl forcing does not directly generate the asymmetric structures of the h, v and u signatures of equatorially trapped Rossby waves. In the mechanism proposed here, the equatorially asymmetric wind stress curl forcing is only indirectly responsible for the observed characteristics of quasi-annual equatorial Rossby waves. The wind stress curl establishes the mean equatorial current system that has the asymmetric meridional shears necessary to modify the latitudinal structure and phase speed of the free modes of the system. Without asymmetric wind stress curl forcing, the equatorial current system would be more nearly symmetric and would have a less dramatic effect on the latitudinal structure of equatorially trapped Rossby waves. It seems probable that the indirect relationship between the asymmetric wind forcing and asymmetric equatorial Rossby waves proposed here has been misinterpreted in past studies as direct wind generation of larger amplitude variability north of the equator.

References

Arthur, R. S. (1960). A review of the calculation of ocean currents at the equator. *Deep Sea Research*, 6, 287–297.
Barnett, T. P. (1983). Interaction of the monsoon and Pacific trade wind system at interannual time scales, Part I: The equatorial zone. *Monthly Weather Review*, 111, 756–773.

Boulanger, J. -P., & Fu, L. -L. (1996). Evidence of boundary reflection of Kelvin and first-mode Rossby waves from TOPEX/POSEIDON sea level data. *Journal of Geophysical Research*, *101*, 16361–16371.

Boulanger, J. -P., & Menkes, C. (1995). Propagation and reflection of long equatorial waves in the Pacific Ocean during the 1992-1993 El Niño. *Journal of Geophysical Research*, *100*, 25041–25059.

Boulanger, J. -P., & Menkes, C. (1999). Long equatorial wave reflection in the Pacific Ocean during the 1992-1998 TOPEX/POSEIDON period. *Climate Dynamics*, *15*, 205–225.

Boyd, J. P. (1978). The effects of latitudinal shear on equatorial waves. Part II: Applications to the atmosphere. *Journal of Atmospheric Sciences*, *35*, 2259–2267.

Boyd, J. P. (1982). The influence of meridional shear on planetary waves. Part 1: Nonsingular wind profiles. *Journal of Atmospheric Sciences*, *39*, 756–769.

Busalacchi, A. J., & Cane, M. A. (1988). The effect of varying stratification on low-frequency equatorial motions. *Journal of Physical Oceanography*, *18*, 801–812.

Chambers, D. P., Tapley, B. D., & Stewart, R. H. (1997). Long-period ocean heat storage rates and basin-scale heat fluxes from TOPEX. *Journal of Geophysical Research*, *102*, 10525–10533.

Chang, P., & Philander, S. G. H. (1989). Rossby wave packets in baroclinic mean currents. *Deep-Sea Research*, *36*, 17–37.

Chelton, D. B., & Schlax, M. G. (1996). Global observations of oceanic Rossby waves. *Science*, *272*, 234–238.

Chelton, D. B. & Schlax, M. G. (2003). The accuracies of smoothed sea surface height fields constructed from tandem altimeter datasets. *Journal of Atmospheric and Oceanic Technology* (in press).

Chelton, D. B., Ries, J. C., Haines, B. J., & Fu, L. -L. (2001). Satellite altimetry. In L. -L. Fu, & A. Cazenave (Eds.), *Satellite altimetry and the earth sciences: a handbook of techniques and applications* (pp. 1–131). Academic Press.

Chelton, D. B., de Szoeke, R. A., Schlax, M. G., El Naggar, K., & Siwertz, N. (1998). Geographical variability of the first baroclinic Rossby radius of deformation. *Journal of Physical Oceanography*, *28*, 433–460.

Chelton, D. B., Freilich, M. H., & Esbensen, S. K. (2000). Satellite observations of the wind jets off the Pacific coast of Central America, Part II: Regional relationships and dynamical considerations. *Monthly Weather Review*, *128*, 2019–2043.

Chelton, D. B., Schlax, M. G., Lyman, J. M. & de Szoeke, R. A. (2003). The latitudinal structure of monthly variability in the tropical Pacific. Manuscript in preparation.

Cleveland, W. S., & Devlin, S. J. (1988). Locally weighted regression: An approach to regression analysis by local fitting. *Journal of the American Statistical Association*, *83*, 596–610.

Deans, S. R. (1983). *The radon transform and some of its applications*. New York: John Wiley pp 289.

Delcroix, T., Picaut, J., & Eldin, G. (1991). Equatorial Kelvin and Rossby waves evidenced in the Pacific Ocean through Geosat sea level and surface current anomalies. *Journal of Geophysical Research*, *96*(Suppl.), 3249–3262.

Delcroix, T., Boulanger, J. -P., Masia, F., & Menkes, C. (1994). Geosat-derived sea level and surface current anomalies in the equatorial Pacific during the 1986-1989 El Niño and La Niña. *Journal of Geophysical Research*, *99*, 25093–25107.

Delcroix, T., Dewitte, B., duPenhoat, Y., Masia, F., & Picaut, J. (2000). Equatorial waves and warm pool displacements during the 1992-1998 El Niño Southern Oscillation events: Observation and modeling. *Journal of Geophysical Research*, *105*, 26045–26062.

de Szoeke, R. A., & Chelton, D. B. (1999). The modification of long planetary waves by homogeneous potential vorticity layers. *Journal of Physical Oceanography*, *29*, 500–511.

Dewar, W. K. (1998). On 'too fast' baroclinic planetary waves in the general circulation. *Journal of Physical Oceanography*, *28*, 1739–1758.

Fu, L. -L., & Cazenave, A. (2001). *Satellite altimetry and earth sciences: a handbook of techniques and applications*. Academic Press 463pp.

Fu, L. -L., & Chelton, D. B. (2001). Large-scale ocean circulation. In L. -L. Fu, & A. Cazenave (Eds.), *Satellite altimetry and the earth sciences: a handbook of techniques and applications* (pp. 133–169). Academic Press.

Fu, L. -L., Vazquez, J., & Perigaud, C. (1991). Fitting dynamic models to the Geosat sea level observations in the tropical Pacific Ocean. Part I: A free wave model. *Journal of Physical Oceanography*, *21*, 798–809.

Greenslade, D. J. M., Chelton, D. B., & Schlax, M. G. (1997). The midlatitude resolution capability of sea level fields constructed from single and multiple satellite altimeter datasets. *Journal of Atmospheric and Oceanic Technology*, *14*, 849–870.

Horel, J. D. (1984). Complex principal component analysis: Theory and examples. *Journal of Climate and Applied Meteorology*, *23*, 1660–1673.

Jerlov, N. G. (1953). Studies of the equatorial currents in the Pacific. *Tellus*, *5*, 308–314.

Johnson, G. C., Sloyan, B. M., Kessler, W. S., & McTaggart, K. E. (2002). Direct measurements of upper ocean currents and water properties across the tropical Pacific Ocean during the 1990s. *Progress in Oceanography*, *52*, 31–61.

Kessler, W. S. (1990). Observations of long Rossby waves in the northern tropical Pacific. *Journal of Geophysical Research*, *95*, 5183–5217.

Kessler, W. S., & McCreary, J. P. (1993). The annual wind-driven Rossby wave in the subthermocline equatorial Pacific. *Journal of Physical Oceanography*, *23*, 1192–1207.

Killworth, P. D., Chelton, D. B., & de Szoeke, R. A. (1997). The speed of observed and theoretical long extra-tropical planetary waves. *Journal of Physical Oceanography*, *27*, 1946–1966.

Knauss, J. A. (1960). Measurement of the Cromwell current. *Deep-Sea Research*, *6*, 265–286.

Lukas, R., & Firing, E. (1985). The annual Rossby wave in the central equatorial Pacific Ocean. *Journal of Physical Oceanography*, *15*, 55–67.

Lukas, R., Hayes, S. P., & Wyrtki, K. (1984). Equatorial sea level response during the 1982–83 El Niño. *Journal of Geophysical Research*, *89*, 10425–10430.

Matsuno, T. (1966). Quasi-geostrophic motions in the equatorial area. *Journal of the Meteorological Society of Japan*, *44*, 25–43.

McPhaden, M. J., & Knox, R. A. (1979). Equatorial Kelvin and inertio-gravity waves in zonal shear flow. *Journal of Physical Oceanography*, *9*, 263–277.

McPhaden, M. J., Busalacchi, A. J., & Picaut, J. (1988). Observations and wind-forced model simulations of the mean seasonal cycle in tropical Pacific sea surface topography. *Journal of Geophysical Research*, *93*, 8131–8146.

McPhaden, M. J., Busalacchi, A. J., Cheney, R., Donguy, J. -R., Gage, K. S., Halpern, D., Ji, M., Julian, P., Meyers, G., Mitchum, G. T., Niiler, P. P., Picaut, J., Reynolds, R. W., Smith, N., & Takeuchi, K. (1998). The Tropical Ocean-Global Atmosphere observing system: A decade of progress. *Journal of Geophysical Research*, *103*, 14169–14240.

Merrifield, M. A., & Guza, R. T. (1990). Detecting propagating signals with complex empirical orthogonal functions: A cautionary note. *Journal of Physical Oceanography*, *20*, 1628–1633.

Meyers, G. (1979). On the annual Rossby wave in the tropical North Pacific. *Journal of Physical Geography*, *9*, 663–674.

Mitchell, T. P., & Wallace, J. M. (1992). The annual cycle in equatorial convection and sea surface temperature. *Journal of Climate*, *5*, 1140–1156.

Mitchum, G. T., & Lukas, R. (1990). Westward propagation of annual sea level and wind signals in the western Pacific Ocean. *Journal of Climate*, *3*, 1102–1110.

Moore, D.W. (1968). Planetary waves in an equatorial ocean. Ph.D. thesis, Harvard University, Cambridge, MA, 207pp.

Moore, D. W., & Philander, S. G. H. (1977). Modeling of the tropical oceanic circulation. In E. D. Goldberg, I. N. McCave, J. J. O'Brien, & J. H. Steele (Eds.), *The sea* (pp. 319–361). New York: Wiley Interscience.

Philander, S. G. H. (1978). Instabilities of zonal equatorial currents, Part 2. *Journal of Geophysical Research*, *83*, 3679–3682.

Philander, S. G. H. (1979). Equatorial waves in the presence of the equatorial undercurrent. *Journal of Physical Oceanography*, *9*, 254–262.

Philander, S. G. H. (1990). *El Niño, La Niña and the Southern Oscillation.* San Diego: Academic Press, Inc 289pp.

Picaut, J., & Busalacchi, A. J. (2001). Tropical ocean variability. In L. -L. Fu, & A. Cazenave (Eds.), *Satellite altimetry and the earth sciences: a handbook of techniques and applications* (pp. 217–236). Academic Press.

Picaut, J., & Tournier, R. (1991). Monitoring the 1979–1985 equatorial Pacific current transports with expendable bathythermograph data. *Journal of Geophysical Research*, *96*, 3263–3277.

Preisendorfer, R. W. (1988). *Principal component analysis in meteorology and oceanography.* New York: Elsevier pp 425.

Proehl, J. A. (1990). Equatorial wave-mean flow interaction: The long Rossby waves. *Journal of Physical Oceanography*, *20*, 274–294.

Proehl, J. A. (1991). On the numerical dispersion relation of equatorial waves. *Journal of Geophysical Research*, *96*, 16929–16934.

Proehl, J. A. (1996). Linear stability of equatorial zonal flows. *Journal of Physical Oceanography*, *26*, 601–621.

Reverdin, G., Frankignoul, C., Kestenare, E., & McPhaden, M. J. (1994). Seasonal variability in the surface currents of the equatorial Pacific. *Journal of Geophysical Research*, *99*, 20323–20344.

Rienecker, M. M., Atlas, R., Schubert, S. D., & Willett, C. S. (1996). A comparison of surface wind products over the North Pacific Ocean. *Journal of Geophysical Research*, *101*, 1011–1023.

Rowe, G. D., Firing, E., & Johnson, G. C. (2000). Pacific equatorial subsurface countercurrent velocity, transport and potential vorticity. *Journal of Physical Oceanography*, *30*, 1172–1187.

Schlax, M. G., & Chelton, D. B. (1992). Frequency domain diagnostics for linear smoothers. *Journal of the American Statistical Association*, *87*, 1070–1081.

Stammer, D. (1997). Steric and wind-induced changes in TOPEX/POSEIDON large-scale sea surface topography observations. *Journal of Geophysical Research*, *102*, 20987–21009.

Susanto, R. D., Zheng, Q., & Yan, X. -H. (1998). Complex singular value decomposition analysis of equatorial waves in the Pacific observed by TOPEX/Poseidon altimeter. *Journal of Atmospheric and Oceanic Technology*, *15*, 764–774.

Tsuchiya, M. (1955). On a simple method for estimating the current velocity at the equator. *Journal of Oceanographic Society of Japan*, *11*, 1–4.

Wang, B., Wu, R., & Lukas, R. (2000). Annual adjustment of the thermocline in the tropical Pacific Ocean. *Journal of Climate*, *13*, 596–616.

Wyrtki, K., & Kilonsky, B. (1984). Mean water and current structure during the Hawaii-to-Tahiti shuttle experiment. *Journal of Physical Oceanography*, *14*, 242–254.

Wyrtki, K., & Meyers, G. (1976). The trade wind field over the Pacific Ocean. *Journal of Applied Meteorology*, *15*, 698–704.

Wyrtki, K., Firing, E., Halpern, D., Knox, R., McNally, G. J., Patzert, W. C., Stroup, E. D., Taft, B. A., & Williams, R. (1981). The Hawaii-to-Tahiti Shuttle Experiment. *Science*, *211*, 22–28.
Yu, X., & McPhaden, M. J. (1999). Seasonal variability in the equatorial Pacific. *Journal of Physical Oceanography*, *29*, 925–947.
Zheng, Q., Yan, X. -H., Ho, C. -R., & Tai, C. -K. (1994). The effects of shear flow on propagation of Rossby waves in the equatorial oceans. *Journal of Physical Oceanography*, *24*, 1680–1687.